

# AN ABSTRACT OF THE THESIS OF

LARRY RUSSELL COOPER for the Ph. D.  
(Name) (Degree)

in PHYSICS presented on July 14, 1969  
(Major)

Title: THE DECAY OF 4.1 HOUR  $Zn^{71}$  AND THE LEVELS  
OF  $Ga^{71}$  BY THE UNIFIED MODEL: LEVELS OF  $Zn^{70}$  BY THE  
 $Zn^{70}(\alpha, \alpha')$  REACTION

Abstract approved: \_\_\_\_\_

Harry T. Easterday

Precision spectroscopy experiments were carried out on the gamma radiations emitted in the decay of 4.1 hour  $Zn^{71}$  and several new transitions were identified. From these results, a decay scheme is proposed for  $Zn^{71}$  in which most of the ambiguities in previously reported schemes have been removed. Using the intermediate-coupling Unified Model of the nucleus, the level energies of  $Ga^{71}$  have been calculated. Vibrational phonon states of the core nucleus of  $Zn^{70}$  are coupled to proton single particle states  $2p_{3/2}$ ,  $1f_{5/2}$ ,  $2p_{1/2}$ , and  $1g_{9/2}$  through a perturbing interaction of the form  $H_{int} = k(r) \sum_{\lambda\mu} a_{\lambda\mu} Y_{\lambda}^{\mu*}$ . The radial dependence of the function  $k(r)$  is taken in one of two forms, Gaussian or derivative Saxon-Woods. For the calculation of radial integrals, radial wave functions are either those generated by a Harmonic Oscillator potential or by a Saxon-Woods potential. Energies and spins of the core excited states were

determined by observing the scattering of 42 Mev alpha particles from  $\text{Zn}^{70}$  and analyzing the inelastic scattering cross sections using the diffraction model. Single particle level spacings are introduced as parameters along with the parameter  $\beta_{\lambda} V_0$  representing the strength of the interaction. Results which agree most closely with experiment arise when  $k(r)$  is taken as the derivative Saxon-Woods shape and Saxon-Woods wave functions are used for the bound states. The first three negative parity levels predicted by the model agree closely in energy and spin with the experimental level scheme. By coupling a  $1g_{9/2}$  particle state to a  $0^+$  phonon state and coupling a  $3^-$  phonon state to  $2p_{3/2}$  and  $1f_{5/2}$  single particle states, energies for positive parity  $9/2$  levels are determined. Two of these levels are fitted to the experimental decay scheme. Eigenvectors for the calculated levels are used to calculate static nuclear moments and gamma ray transition probabilities. Several results from these calculations are in good agreement with the experimental values. It is concluded that the unified model can be applied to describe low lying excited states of  $\text{Ga}^{71}$ .

The Decay of 4.1 Hour  $\text{Zn}^{71}$  and the Levels of  
 $\text{Ga}^{71}$  by the Unified Model: Levels of  $\text{Zn}^{70}$   
by the  $\text{Zn}^{70} (\alpha, \alpha')$  Reaction

by

Larry Russell Cooper

A THESIS

submitted to

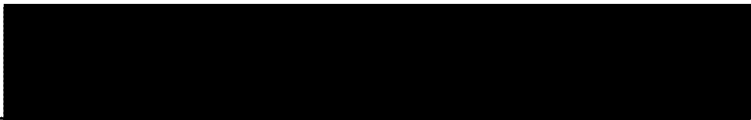
Oregon State University

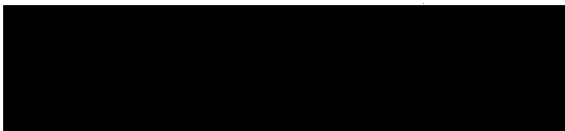
in partial fulfillment of  
the requirements for the  
degree of


Doctor of Philosophy

June 1968

APPROVED:

  
\_\_\_\_\_  
Professor of Physics  
in charge of major

  
\_\_\_\_\_  
Chairman of Department of Physics

  
\_\_\_\_\_  
Dean of Graduate School

Date thesis is presented July 14, 1968

Typed by Marion F. Palmateer for Larry Russell Cooper

## ACKNOWLEDGEMENTS

It is with gratitude and appreciation that these acknowledgements are made. Particularly, gratitude is expressed to Dr. Harry T. Easterday, the major professor, for his advice, guidance, patience, and continued encouragement. Thanks are expressed to several individuals for their help, time, and encouragement: To Dr. Victor A. Madsen with regard to the theoretical development, who asked the necessary questions; To Dr. Chris Zafiratos for his advice and assistance on the scattering experiment; To Dr. Larry Schechter for his interest and support. There are many others who could be mentioned for their assistance. To name a few, Mr. Frank Schmittroth for his computer program BSWF, Mr. Michael Stomp for assistance with the computer problem, and Mr. Donald Walker for use of his efficiency curve. Without the aid and advice of these individuals, the successful conclusion of this study would not have been possible.

# TABLE OF CONTENTS

	<u>Page</u>
INTRODUCTION	1
EXPERIMENTAL APPARATUS AND PROCEDURE	7
Source Preparation	7
Apparatus and Procedure	9
Data Analysis and Results	20
DECAY SCHEME OF $\text{Zn}^{71}$	43
UNIFIED MODEL FOR $\text{Ga}^{71}$	53
Introduction	53
Intermediate Coupling Model	57
INELASTIC SCATTERING OF ALPHA PARTICLES FROM $\text{Zn}^{70}$	76
Apparatus and Procedure	76
Data Analysis and Results	82
DISCUSSION OF SCATTERING EXPERIMENT	101
CONCLUSIONS	110
BIBLIOGRAPHY	121
APPENDICES	125
Appendix A     Derivations of Formulas for Unified Model Calculations	125
Appendix B1    Computer Program Matrial Calculation of Matrix Elements	135
Appendix B2    Computer Program BSWF, Bound State Wave Functions for the Saxon-Woods Potential	137

## LIST OF FIGURES

<u>Figure</u>		<u>Page</u>
1	Typical gamma ray spectrum from Ge(Li) detector.	11
2	Block diagram of electronics for coincidence experiment (energy analysis in Ge(Li) channel).	13
3	Block diagram of electronics for coincidence experiment (energy analysis in Na I channel).	14
4	Block diagram of electronics for delayed coincidence experiment.	16
5	Typical delayed coincidence spectrum.	18
6	$Zn^{71}$ gamma ray spectrum. 0-650 kev.	21
7	$Zn^{71}$ gamma ray spectrum. 650-1200 kev.	22
8	$Zn^{71}$ gamma ray spectrum. 1200-2000 kev.	23
9	$Zn^{71}$ gamma ray spectrum. 2000-2800 kev.	24
10	$Zn^{71}$ gamma ray spectrum from Na I detector.	25
11	Relative efficiency curve.	32
12	Gamma-gamma coincidence. Ge(Li) gate - 387.	36
13	Gamma-gamma coincidence. Ge(Li) gate - 488.	37
14	Gamma-gamma coincidence. Ge(Li) gate - 512.	38
15	Gamma-gamma coincidence. Ge(Li) gate - 596.	39
16	Gamma-gamma coincidence. Ge(Li) gate - 620.	39
17	Gamma-gamma coincidence. Na I gate - 940 to 1020 kev.	40
18	Gamma-gamma coincidence. Na I gate - 1040 to 1090 kev.	40
19	Delayed coincidence. 610-500 kev.	42
20	Decay scheme of 4.1 hour $Zn^{71}$ .	44

<u>Figure</u>		<u>Page</u>
21	Total absorption gamma ray spectrum of $\text{Zn}^{71}$ .	46
22	Decay scheme for 2.2 minute activity of $\text{Zn}^{71}$ .	49
23	Alternative level schemes for $\text{Ga}^{71}$ .	51
24	Type I calculation. $E_1 = 0.70 \text{ Mev}$ , $E_2 = 2.00 \text{ Mev}$ .	67
25	Type II calculation. $E_1 = 0.75 \text{ Mev}$ , $E_2 = 2.00 \text{ Mev}$ .	68
26	Type III calculation. $E_1 = 0.70 \text{ Mev}$ , $E_2 = 1.80 \text{ Mev}$ .	69
27	Comparison of experimental and theoretical level schemes for $\text{Ga}^{71}$ .	71
28	Positive parity levels - Type III calculation.	74
29	Positive parity levels including quadrupole excitation.	75
30	Block diagram of electronics for inelastic scattering experiment.	78
31	Typical scattered alpha particle spectrum - $\theta = 34^\circ$ .	84
32	Geometry for computing energy losses in the target.	86
33	Ratio of differential elastic scattering cross section to Rutherford cross section - $B(\theta_c)$ .	89
34	Differential elastic scattering cross section. $Q = 0$ .	93
35	Differential scattering cross section. $Q = -875 \text{ kev}$ .	94
36	Differential scattering cross section. $Q = -1750 \text{ kev}$ .	95
37	Differential scattering cross section. $Q = -1960 \text{ kev}$ .	96
38	Differential scattering cross section. $Q = -2360 \text{ kev}$ .	97
39	Differential scattering cross section. $Q = -2810 \text{ kev}$ .	98
40	Differential scattering cross section. $Q = -2990 \text{ kev}$ .	99
41	Differential scattering cross section. $Q = -3295 \text{ kev}$ .	100
42	Level schemes of even mass zinc isotopes.	105



# LIST OF TABLES

<u>Table</u>		<u>Page</u>
1	Calibration sources.	27
2	Energies and relative intensities of gamma rays of $\text{Zn}^{71}$ decay.	30
3	Eigenvector coefficients $a(j, NR, I)$ for low lying states in $\text{Ga}^{71}$ .	70
4	Levels energies in $\text{Zn}^{70}$ .	83
5	Static nuclear moments.	114
6	Transition probabilities.	117

THE DECAY OF 4.1 HOUR  $\text{Zn}^{71}$  AND THE LEVELS OF  
 $\text{Ga}^{71}$  BY THE UNIFIED MODEL: LEVELS OF  $\text{Zn}^{70}$   
BY THE  $\text{Zn}^{70} (\alpha, \alpha')$  REACTION

INTRODUCTION

One of the more useful approaches used to describe the nucleus is to construct a Nuclear Model. For example, there is the Shell Model which predicts the ground state spin for nearly all nuclei. Or, there is the Vibrational Model which describes the systematic ordering of excited levels in even-even nuclei as collective vibrations of the nuclear surface.

An attempt is made here to use a model to explain the level structure in  $\text{Ga}^{71}$ . The model chosen is a unification of the Shell Model and the Vibrational Model, and it is an extended version of the weak coupling model suggested by Bohr and Mottelson (7). Experimental observations of the decay of  $\text{Zn}^{71}$  populating levels in  $\text{Ga}^{71}$  are used to construct a level scheme for  $\text{Ga}^{71}$ . The validity of the model is tested by requiring the predictions of the model calculations to agree with the experimental decay scheme.

Prior to the advent of solid state lithium drifted germanium detectors,  $\text{Ge(Li)}$ , most gamma ray spectroscopic studies were performed with scintillation crystal detectors. Such detection systems have, at best, an energy resolution of about 7 to 8% for gamma

rays in the energy region of one Mev. The germanium detectors provide an improvement in resolution of a factor of ten, or more, with, however, a great sacrifice in detection efficiency. The use of the germanium detectors, by virtue of their higher resolution, has revealed much new evidence in gamma ray spectroscopy which was previously concealed. New gamma ray transitions have been found which had been missed when studied with scintillation systems. By using sources of gamma rays with well known and precise energies, germanium detectors are capable of measurements of gamma ray energies to high precision. This feature will be of major importance to this study.

Spectroscopy experiments were performed on the radioactive nucleus  $\text{Zn}^{71}$  which has a half life of 4.1 hours. This nucleus decays by beta emission to excited states in  $\text{Ga}^{71}$  followed by gamma ray transitions leading to the ground state. Previous studies (26, 44) of  $\text{Zn}^{71}$  indicated the presence of a ground state with a half life of 2.2 minutes and a 4.1 hour isomeric state,  $\text{Zn}^{71m}$ . From the beta decay energies, the excited state is estimated to lie 350 kev above the ground state. The modes of decay of the two states are different and populate, in general, different levels in  $\text{Ga}^{71}$ . Only the 4.1 hour activity is discussed here.

The decay schemes for  $\text{Zn}^{71}$  reported by Le Blanc, Cork, and Burson (26) and by Thwaites and Pratt (44) are very simple and show

the presence of only three gamma rays in cascade, the order being uncertain. Both groups used scintillation detectors. A single beta ray group is seen to be in coincidence with all of the gamma rays, whose energies are 390, 495 and 610 kev. Later studies by Sonnino, Eichler, and Amiel (40) and by Tandon and Devare (42) show evidence of a multitude of higher energy gamma rays. Most of these that were found required use of a spectrum unfolding technique applied to the complex gamma ray spectrum since both of these groups used NaI scintillation detector systems. The results of the two groups do not agree and different decay schemes were suggested.

The present study attempts to resolve these difficulties. The germanium detector made very clear that a completely new picture had to be formed. The only transition which survives unchanged by this study is the 390 kev gamma ray, with an improved energy value of  $386.8 \pm 0.1$  kev. Others previously reported are either resolved into two or more separate gamma rays or have not been found to exist. Coincidence relationships are found between several of the radiations, but for most transitions, low intensities of the radiations and low efficiency of the detector combine to prevent such measurements. Energies of the transitions are measured to a very high precision. These experimental results are then used to construct a decay scheme. Beta ray branching is deduced from the intensity measurements, as direct beta ray measurements are precluded by the

presence of strong impurity radiations in the sources.

After the completion of the experiments, another study of  $\text{Zn}^{71}$  was reported by Li and Monaro (27) who also used germanium detectors. Their results are in good agreement with those reported here but differ in a few aspects. The energy measurements reported here have greater precision which is one important difference. Also, their study was restricted to gamma rays of energies less than 1200 kev and several transitions of higher energies are reported here. Many of the ambiguities in the decay scheme of Li and Monaro are eliminated in the decay scheme deduced from this study, and the higher energy transitions are fit into the scheme.

The weak coupling model, suggested by Bohr and Mottelson (7), involves the coupling of a single particle proton state to a vibrational core state. The coupling is treated as a perturbation in the product space of the core and particle. The model is extended here in a similar manner with other studies (8, 9, 17, 43) to include several possible single particle states which introduce admixtures of these states into the calculated energy levels. The model is referred to as an intermediate coupling model or as a Unified Model.

The model calculations require a knowledge of the energies of the vibrational core states along with their spins. The core in this case is  $\text{Zn}^{70}$ . This information was found through a study of the inelastic scattering of 42.5 Mev alpha particles from  $\text{Zn}^{70}$ . Analysis

of the differential cross sections verifies the assumption that low lying excited states of this nucleus can be described by the vibrational model. The results for the energies and spins of the various core levels are then used for the model calculation.

The single particle level spacings are not well known. Results of calculations for  $\text{Cu}^{63}$  and  $\text{Cu}^{65}$  (8) using the Unified Model, suggest values of about 1.2 to 1.4 Mev for the  $2p_{3/2}^- - 1f_{5/2}^-$  splitting and of 1.4 to 1.8 Mev for the  $2p_{3/2}^- - 2p_{1/2}^-$  splitting. These three single particle states are the only ones considered for determining negative parity states. Kisslinger and Sorensen (24) from their calculations on spherical nuclei, suggest values of 0.95 and 2.25 Mev respectively, for  $Z = 30$  and  $N = 34$  nuclei. Thus, various energies in these ranges were used until the theoretical level scheme agreed with the experimentally deduced scheme for  $\text{Ga}^{71}$ . The results are very sensitive to the choice of splitting. Positive parity states were also considered by coupling a  $1g_{9/2}^+$  particle state to the positive parity vibrational levels. The coupling of a  $2p_{3/2}^-$  and a  $1f_{5/2}^-$  particle to the  $3^-$  octupole vibration were included.

Radial integrals which occur in the calculation of the matrix elements of the perturbing interaction require some decisions as to the form of radial wave functions to be used for the single particle orbital. Two different choices were made; first, Harmonic Oscillator functions and second, the wave functions derived for a

Saxon-Woods potential. The form of the interaction was chosen as either of Gaussian shape or of a derivative of the Saxon-Woods potential. The energy level configuration was adjusted in terms of a coupling parameter proportional to  $\beta_{\lambda} V_o$ , where  $\beta_{\lambda}$  is the collective deformation of the core and  $V_o$  is the strength of the interaction.

The success of the method suggests the possibility of describing  $\text{Ga}^{71}$  in terms of this Unified Model. The low lying energy levels can be fit very well using the radial wave functions for a Saxon-Woods potential and an interaction of the form of the derivative of this potential. The final decay scheme retains some ambiguities, particularly, for the high lying levels, but the lower levels are well described by the model.

## EXPERIMENTAL APPARATUS AND PROCEDURE

### Source Preparation

Zinc foils were exposed to the internal deuteron beam of the Oregon State University 37 inch cyclotron. Bombardments were made at a beam energy of six Mev for periods of about two hours. Targets were made from commercial grade zinc foil rolled to a thickness of 0.010 inches. Natural abundances of the stable zinc isotopes are as follows:  $\text{Zn}^{64}$  (48.9%),  $\text{Zn}^{66}$  (27.8%),  $\text{Zn}^{67}$  (4.1%),  $\text{Zn}^{68}$  (18.5%), and  $\text{Zn}^{70}$  (0.6%). Since (d,p) and (d,n) reactions predominate at this energy, the following radioactive isotopes were expected to be formed:  $\text{Zn}^{65}$ ,  $\text{Ga}^{65}$ ,  $\text{Ga}^{67}$ ,  $\text{Ga}^{68}$ ,  $\text{Zn}^{69}$ , and  $\text{Zn}^{71}$ . All activities decay into stable isotopes with the exception of  $\text{Ga}^{65}$  which decays by positron emission with a half life of 15 minutes into  $\text{Zn}^{65}$ .  $\text{Zn}^{65}$  has a long half life of 245 days.

The removal of gallium from the zinc was easily carried out using solvent extraction (18). Gallium is highly soluble in ethyl ether as compared to its solubility in hydrochloric acid; however, the situation is the reverse for zinc. It is necessary to keep the pH of the solutions at the proper levels. The bombarded foils were dissolved in 6.0 N HCl. Ethyl ether was added and the mixture shaken vigorously for one minute in a separation funnel. The solution was



allowed to stand for three minutes while the two immiscible liquids separated into ether and acid phases. The acid portion containing the zinc isotopes was then drawn off, and the gallium in the ether was discarded. This process was repeated three more times to assure essentially 100% separation. This estimate was based on the intensities of characteristic gamma rays of  $\text{Ga}^{65}$  which emanate from the source at the end of the separation. The estimate agrees with the conclusions of Grahame and Seaborg (18) for this extraction process. The acid portion was evaporated to dryness until only the zinc chloride residue remained. The residue was packed into a small lucite cylinder which was then sealed to prevent spilling. The cylinder walls were 1.5 cm thick which was thick enough to stop positrons emitted by impurity isotopes and thus to prevent their annihilation exterior to the source. In coincidence experiments this arrangement eliminates the possibility of detecting annihilation gamma rays from positrons stopped in the surroundings.

After chemical separation, several isotopes still remained as impurities in the source. Although radiations from the  $\text{Zn}^{71}$  were moderately intense, the radiations from the isotopes  $\text{Zn}^{69}$  and  $\text{Zn}^{65}$  were much more intense. Transitions from an isotope identified as  $\text{Na}^{24}$  also appeared prominently. The presence of the  $\text{Na}^{24}$  is unexplained. Since commercial grade zinc was used for the targets, it was thought that the impurity could be eliminated by using highly

purified zinc foils. However, the  $\text{Na}^{24}$  contamination was still present when such target material was used.

### Apparatus and Procedure

The primary detector was a  $1.2 \text{ cm}^3$  lithium drifted germanium crystal with a six millimeter depletion layer and was biased at 510 volts. A cryostat and liquid nitrogen reservoir system was used to keep the detector cooled to a temperature of  $77^\circ \text{ K}$ , which is imperative for germanium detectors, in order to reduce the leakage current. Large leakage currents result in poor detector resolution. The detector was coupled to a low noise charge sensitive preamplifier, Technical Measurements Corp. Model 327A, through a low capacitance lead to make the signal to noise ratio as large as possible. For the majority of the experiments, the input stage of the preamplifier consisted of an EC 1000 low noise thermionic tube, but near the end of the experimental period, the tube was replaced by a field effect transistor. (This step improved the energy resolution of the system from 3.7 to 2.7 keV (FWHM) for the 122 and 136 keV gamma rays of  $\text{Co}^{57}$ .) For cooled detectors, the noise introduced by the preamplifier provides the main limitation on the resolution of the system. Preamplifier signals were fed into a TMC Amplifier-Bias Amplifier System, Model 320. This unit is the TMC version of the very low noise system designed by J. S. Goulding at the Lawrence Radiation

Laboratory. The integration time of the signal at the input of the amplifier was 100 nanoseconds, a value determined empirically to give the best signal to noise ratio. The pulse was further shaped by single delay line differentiation in a terminated 800 nanosecond delay line. This combination provided the best overall resolution for low counting rates. An output pulse stretcher formed flat-topped pulses of 0-8 volts amplitude. This pulse shape gives rise to the best gain stability in the multichannel analyzer and thus the best overall resolution. For pulse analysis and the storage of data, a TMC Multichannel Analyzer, Model 404A, was used.

The Bias Amplifier portion of the system was useful for expanding small sections of the gamma ray spectrum for detailed investigation. This feature was used in making the relative intensity measurements by spreading the peaks out over 15 or 20 channels of the analyzer for better peak and background definition.

A typical spectrum for a single gamma ray is shown in Figure 1. The gamma ray has an energy of 662 kev and the figure shows the low photoelectric cross section inherent in germanium detectors; that is, the Compton distribution is pronounced relative to the photopeak. The small peak at about 200 kev arises from the backscattered gammas in the source and the surroundings. This peak is broader than the photopeak and its energy can be predicted exactly from the photopeak energy.

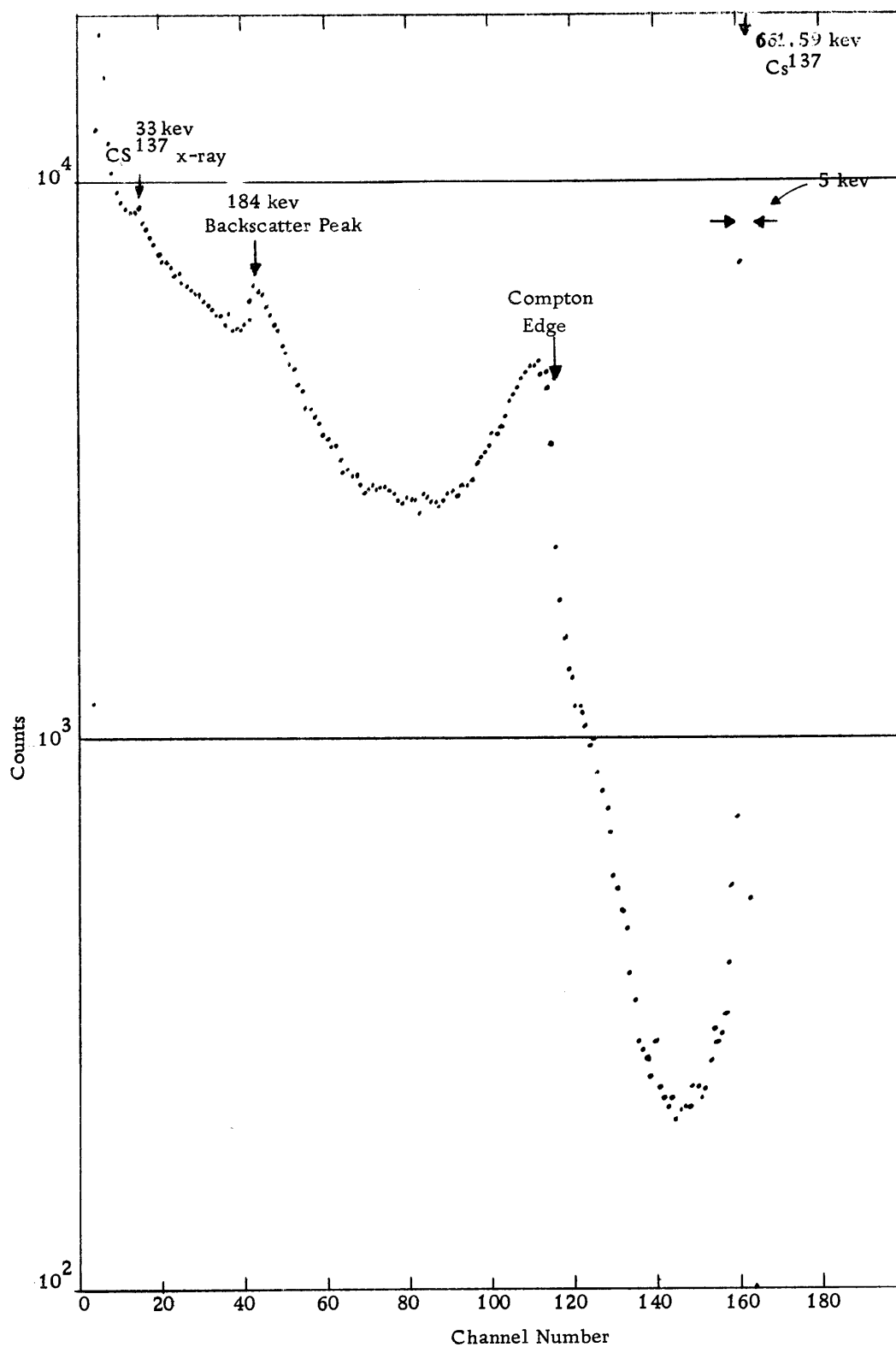


Figure 1. Typical gamma ray spectrum from Ge(Li) detector.

Figures 2 and 3 show block diagrams of the apparatus for the coincidence measurements in the fast-slow coincidence configuration. The second detector was a 3" x 3" NaI crystal mounted on a Dumont 6363 photomultiplier tube. Experiments were carried out in two configurations. First, energy analysis was performed in the Ge(Li) "channel", Figure 2. In this system each gamma ray is resolved well enough that a given transition can be analyzed separately by the single channel analyzer. Second, the energy analysis was made in the NaI "channel", Figure 3. In this case, close lying doublet peaks could not be resolved and so two or more gamma rays are analyzed simultaneously. This configuration, of course, does not provide conclusive coincidence information but proved useful in the investigations of several of the weak gamma rays.

Timing was adjusted by feeding signals from a precision pulse generator into both channels and inserting delay lines at appropriate places so that the pulses arrived simultaneously at the coincidence circuit input. A variable delay within the Amplifier System provided a fine tuning adjustment for the fast coincidence requirements. Fast pulses were generated by the crossover pickoff gates. In the NaI side, the Hamner Linear Amplifier, Model N308, incorporates a pickoff gate to generate a large negative pulse. This pulse was fed into a pulse inverter-pulse shaper circuit which produced a small, fast rising, positive, flat-topped pulse, ideal for use with the fast

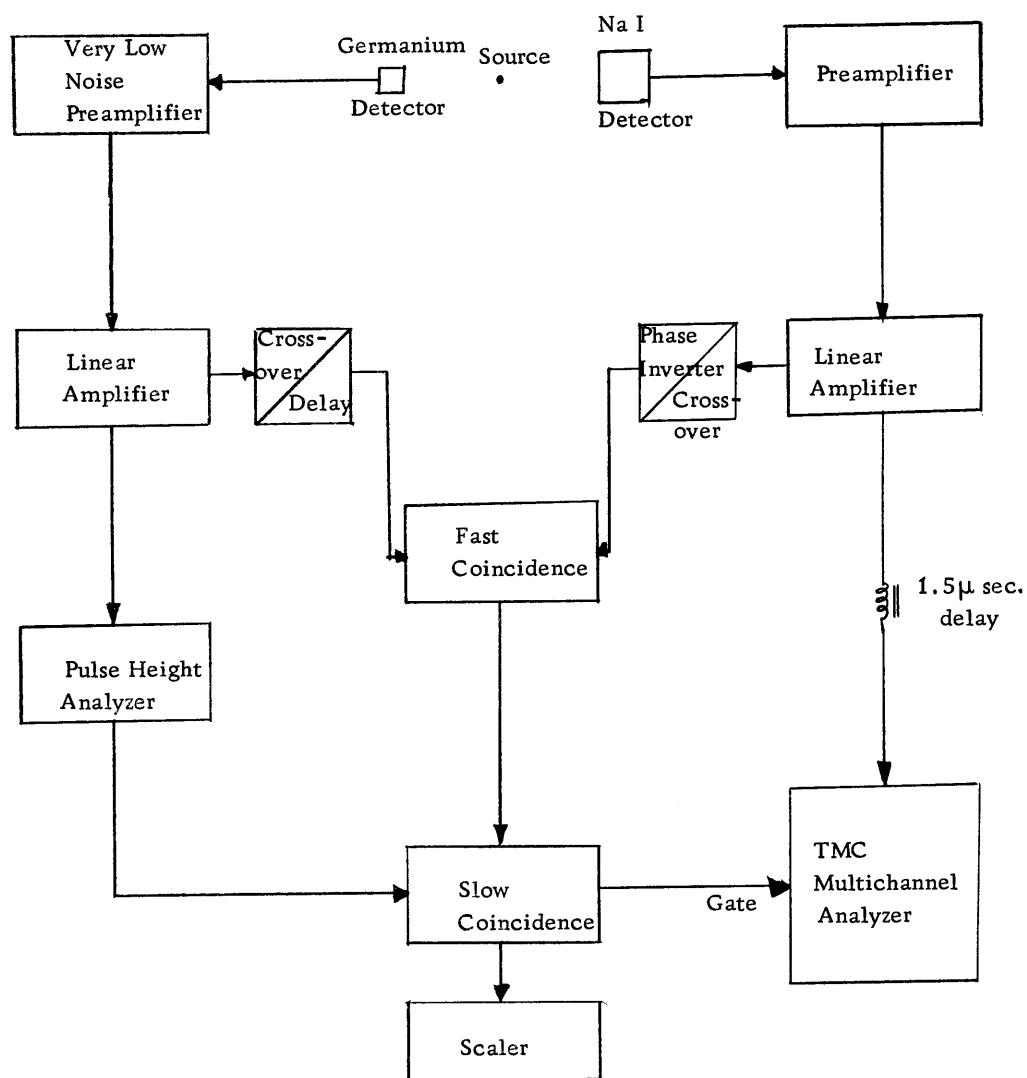


Figure 2. Block diagram of electronics for coincidence experiment (energy analysis in Ge(Li) channel).

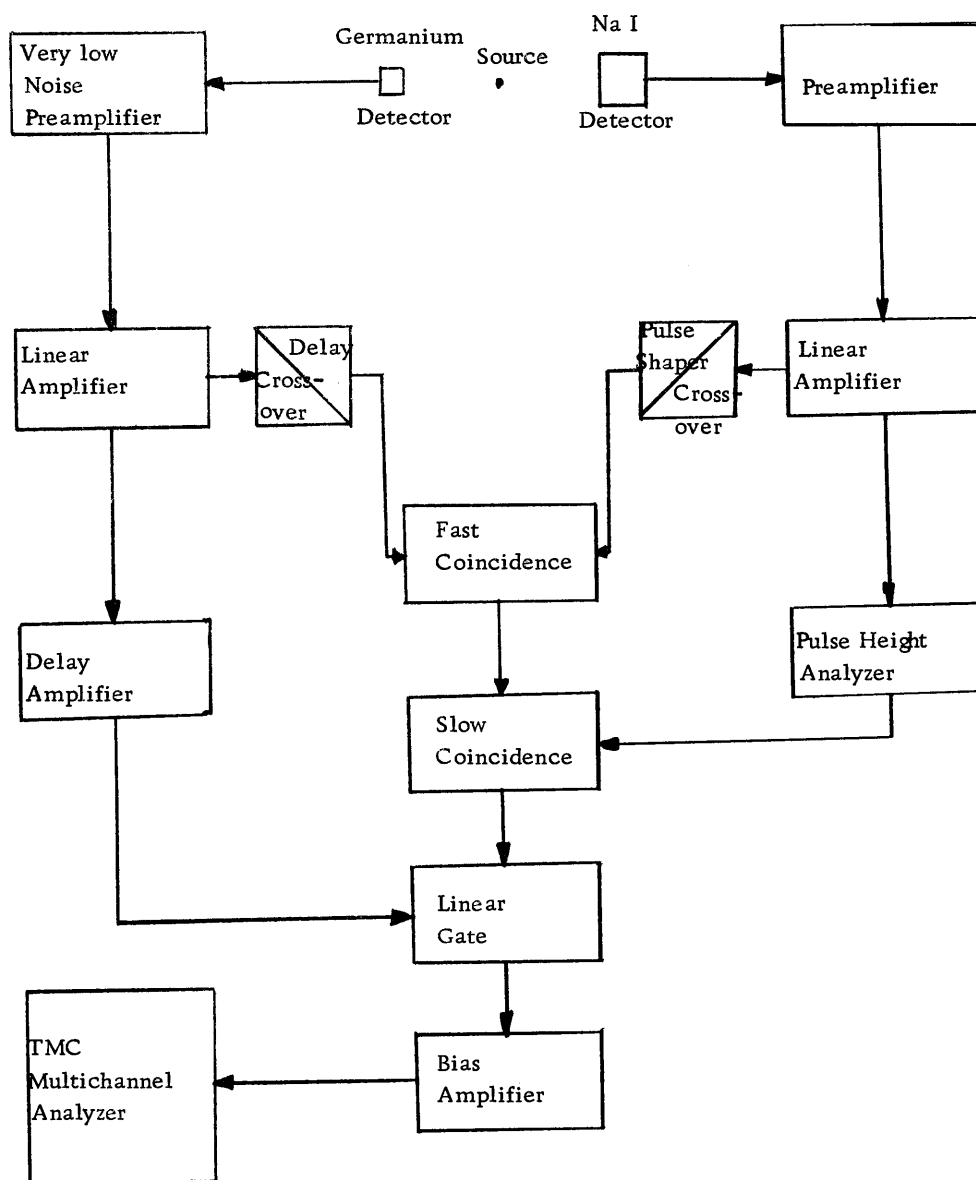


Figure 3. Block diagram of electronics for coincidence experiment (energy analysis in Na I channel).

coincidence circuit. The TMC system has an equivalent crossover gating circuit within the main amplifier. The fast coincidence resolving time was variable continuously from 10 to 110 nanoseconds. The slow coincidence circuit provides the condition on energy. A square pulse, two microseconds long, is produced which gates the multichannel analyzer.

The second experimental configuration, Figure 3, required energy selection in the NaI "channel". The linear gate was used which avoided the need of gating the analyzer.

The detectors and source defined a horizontal plane with the detector axes oriented at right angles in order to eliminate the detection of gamma rays from positron annihilation. Lead shielding was placed between the detectors to inhibit detection of scattered radiations.

Figure 4 is a block diagram of the electronic system used for the delayed coincidence experiments. The detectors consisted of 1 1/2" x 2" NaI crystals optically coupled to 14 stage, high gain, RCA-6810 photomultiplier tubes operated at 2200 volts. Pulses from the tenth dynodes were fed into 404A limiter amplifiers with the outputs feeding into 100 nanosecond clipping stubs. Fast rising pulses (i. e. less than five nanoseconds) were thus changed into square, flat-topped pulses of 200 nanoseconds duration. These pulses were then fed into the Time to Pulse Height Converter which uses the



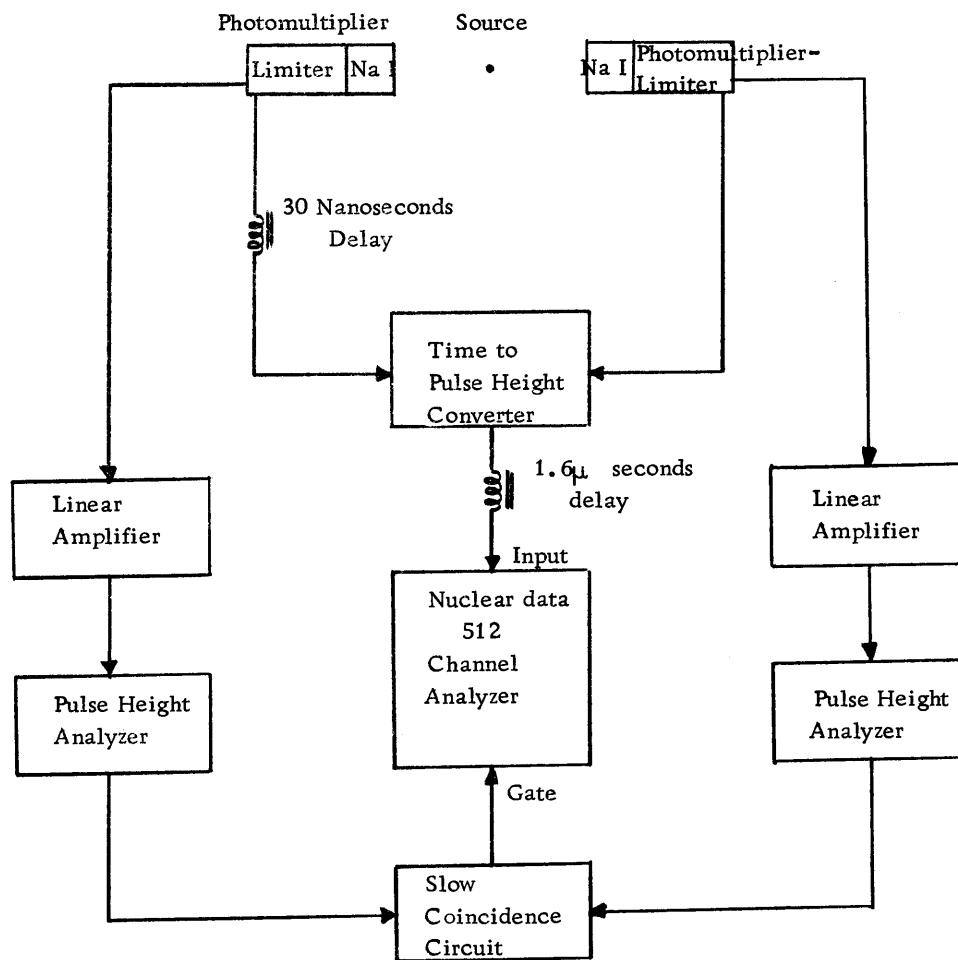


Figure 4. Block diagram of electronics for delayed coincidence experiment.

design of Green and Bell (20) as modified by Sommerfeldt (39). When the two limited pulses have maximum overlap in time, the converter produces a maximum amplitude output pulse. After a small delay, the converter pulses were fed into the gated analyzer for analysis of the coincidence spectrum.

Anode pulses of each detector were amplified and analyzed in single channel pulse height analyzers to provide energy selection requirements on the coincident gamma rays. The analyzer pulses were fed into a slow coincidence circuit with the output used to gate the multichannel analyzer.

Figure 5 shows a typical "prompt" spectrum arising from coincidences between the annihilation gamma rays in the decay of  $\text{Na}^{22}$ . The coincidence counting rate is plotted as a function of amplitude, or time of delay between pulses. The prompt peak is the symmetrical distribution due to the maximum overlap of the limiter pulses in the converter (i. e. exact time coincidence). The width of the peak at half of the maximum height is defined as the resolving time of the system,  $2\tau$ . The peak appearing in the low amplitude part of the spectrum is due to single pulses arriving at the converter which can generate small output pulses; this is referred to as single channel feed-through. The plateau region between peaks is a result of coincident pulses from the detectors which are of insufficient amplitude to properly drive the limiters to saturation, and so the

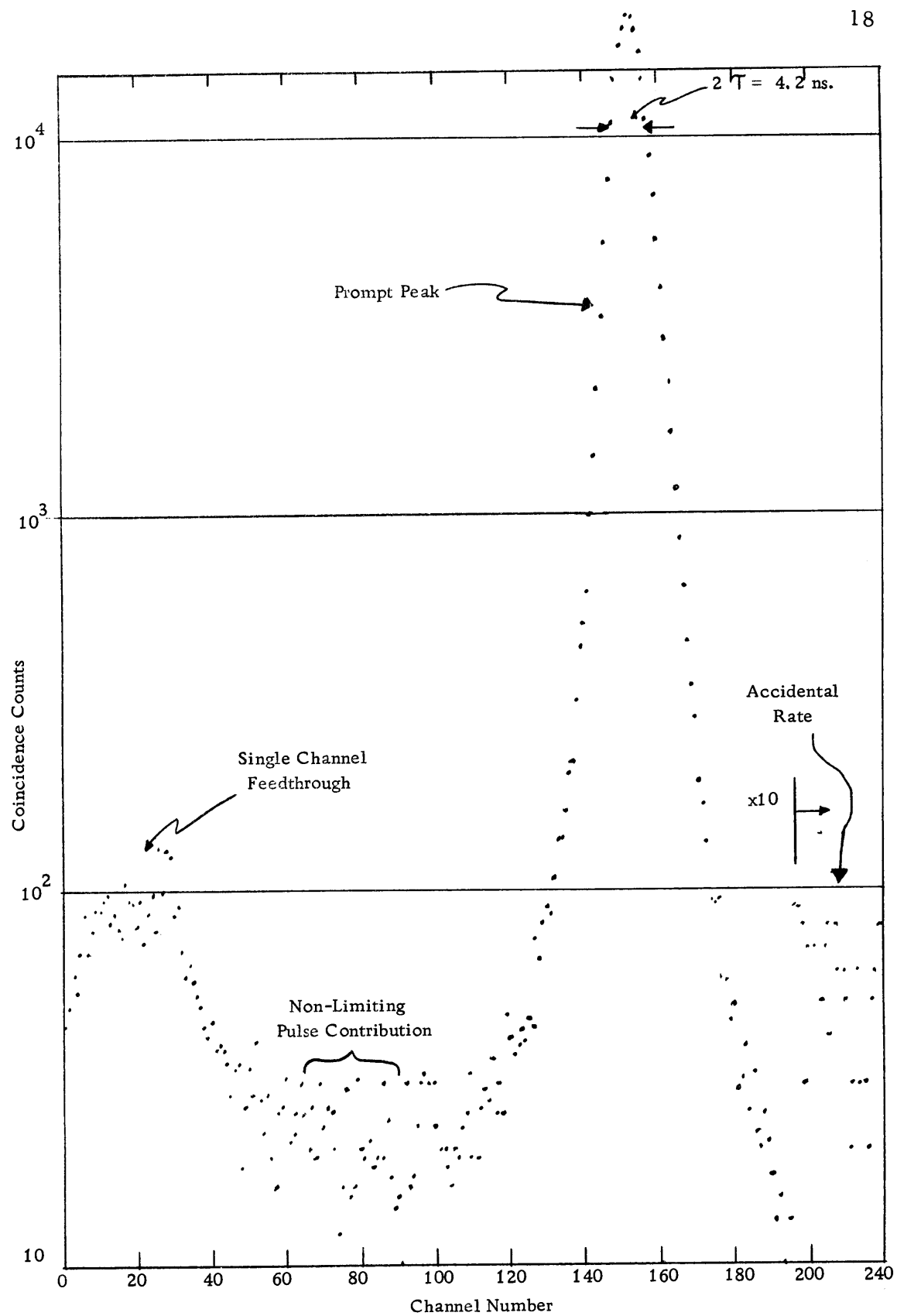


Figure 5. Typical delayed coincidence spectrum.

pulses are not properly shaped for the converter. This situation arises mostly from Compton scattered events in the detectors.

By inserting a 100 ns delay line in one side of the fast pulse channels of the system, the prompt peak is shifted downward in amplitude. Now coincidence pulses which are separated slightly in time will give rise to events which fall to the right of the prompt peak. The spectrum of such coincidence rates can be analyzed on a semilog plot against time to give the decay constant for the nuclear level involved. For very small shifts away from the prompt spectrum, the centroid shift method may be used (33).

Various delays having values ranging from 15 to 90 ns were put in the place of the 100 ns line. By plotting the peak position channel number as a function of the amount of delay added, the system was calibrated giving the amount of delay per channel. The calibration constant was 0.424 ns per channel. The linearity was very good, so that the points could be fitted by eye. One further check of the system required that the calibration line have the same slope regardless of to which channel the delay was added.

Care was taken to see that the peak position was not subject to drift effects in the electronics; it was found that no corrections were necessary for counting periods of 12 hours or less.

The NaI detectors could not resolve the 488-512 and 596-620 kev doublets in the  $\text{Zn}^{71}$  spectrum, so the pulse height analyzer

analyzed both gamma rays simultaneously. Thus, the experiments could not be expected to give unambiguous results. However, if the two levels involved had rather different lifetimes, then a composite spectrum would result.

It was estimated that the shortest lifetime that could be measured was about  $5 \times 10^{-10}$  seconds. For any lifetime shorter than this, it may be concluded that the transitions are either of E1, M1, E2 character, based on the Weisskopf single particle estimates (5).

### Data Analysis and Results

Figures 6 through 9 show the  $\text{Zn}^{71}$  gamma ray spectrum from 0 to 3000 kev, using the Ge(Li) detector. For comparison, Figure 10 shows the spectrum from a 3" x 3" NaI crystal. Spectra were obtained for several successive, equal time intervals providing a sequence of spectra taken over a total duration of as long as 36 hours. From these spectra, the area under each gamma ray photopeak was determined and the number plotted as a function of time on semilog graph paper. The usual counting rate versus time decay curves were obtained. In this procedure, each gamma ray can be investigated separately, and the background is accounted for accurately. For all of the gamma rays finally attributed to  $\text{Zn}^{71}$ , the values of  $T_{1/2}$  fall within the range of  $4.1 \pm 1.0$  hours, in good agreement with previous measurements (26, 44). Intensities of a few gamma rays were so

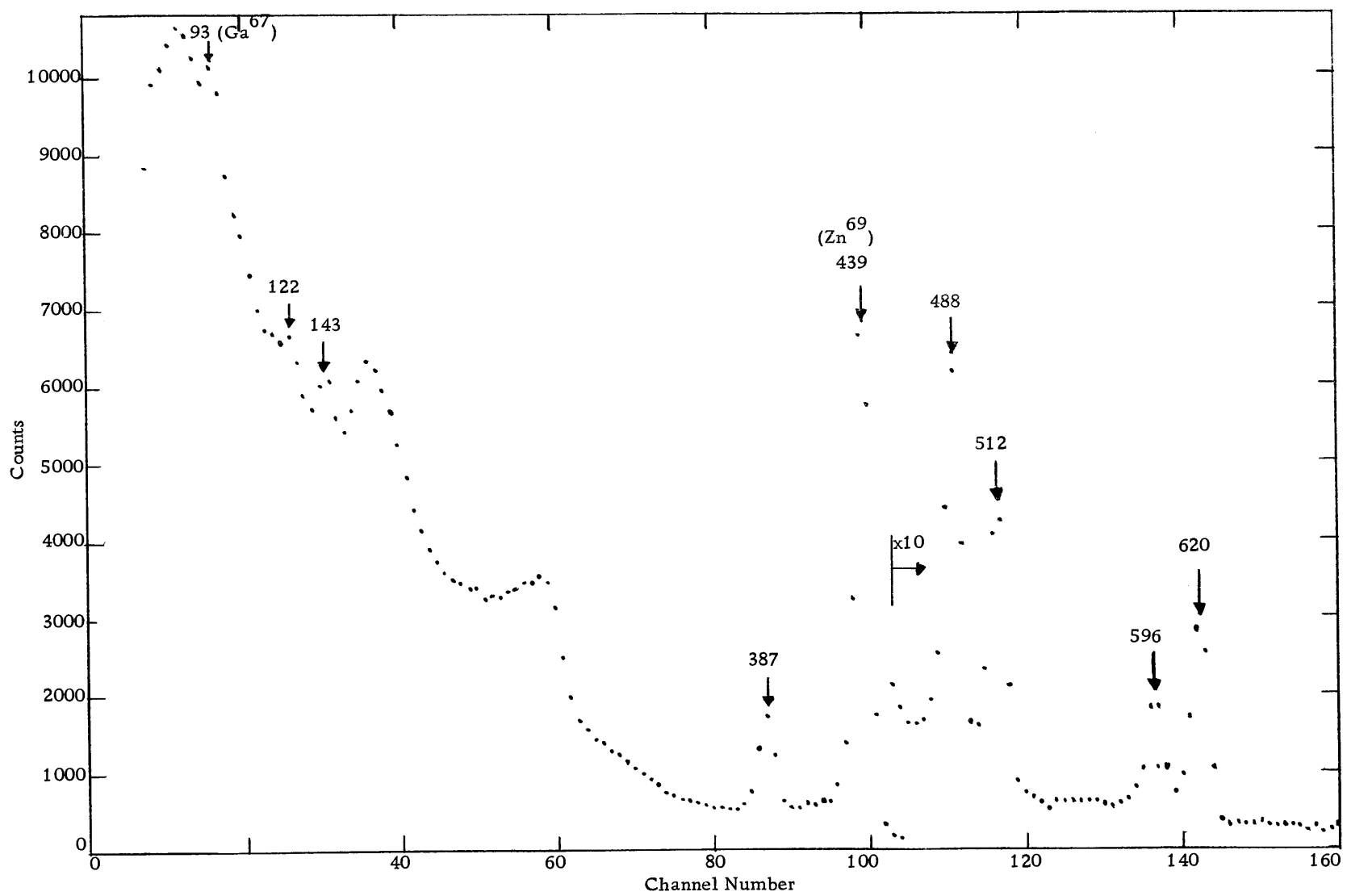


Figure 6.  $Zn^{71}$  gamma ray spectrum. 0-650 kev.

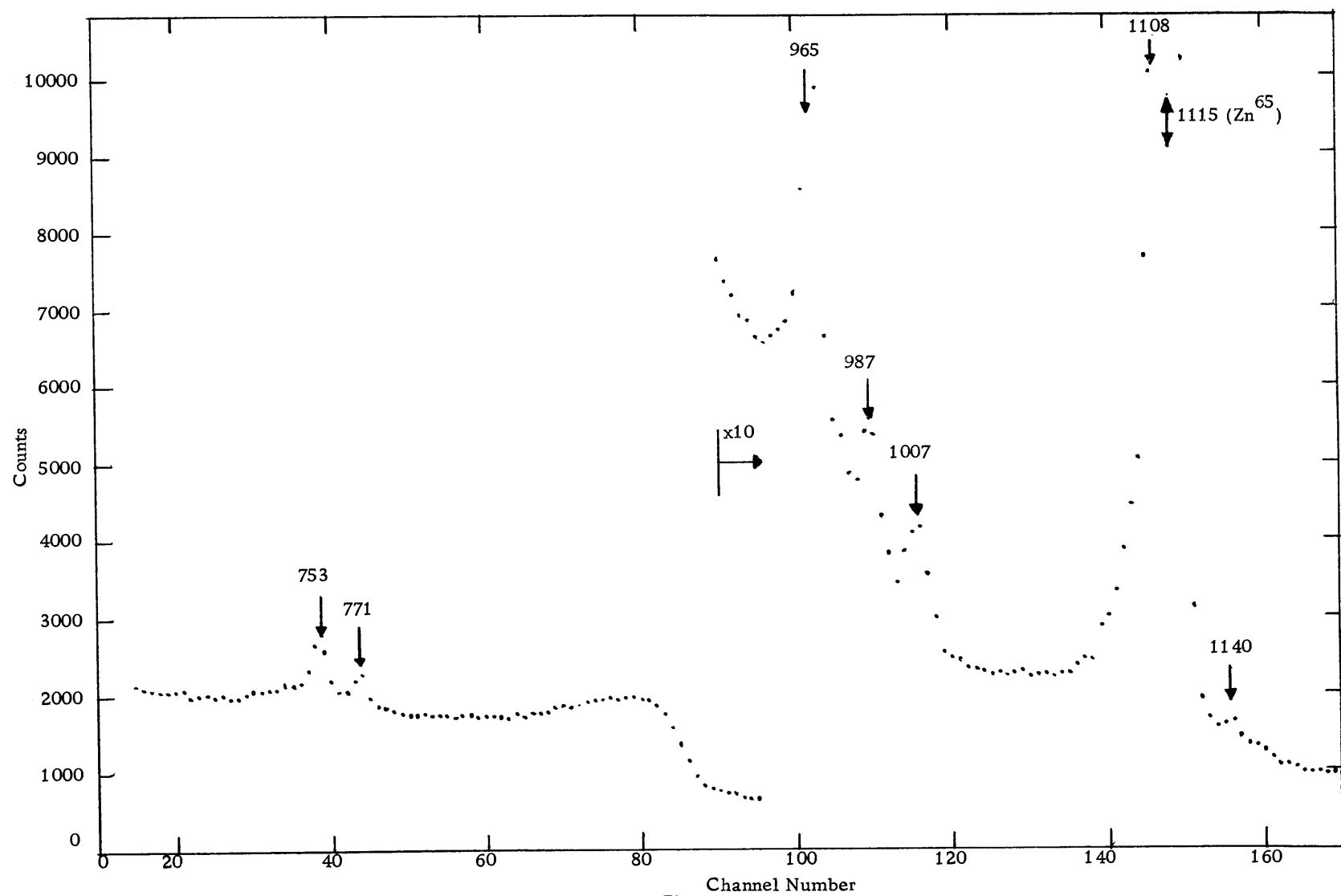


Figure 7.  $Zn^{71}$  gamma ray spectrum. 650-1200 kev.

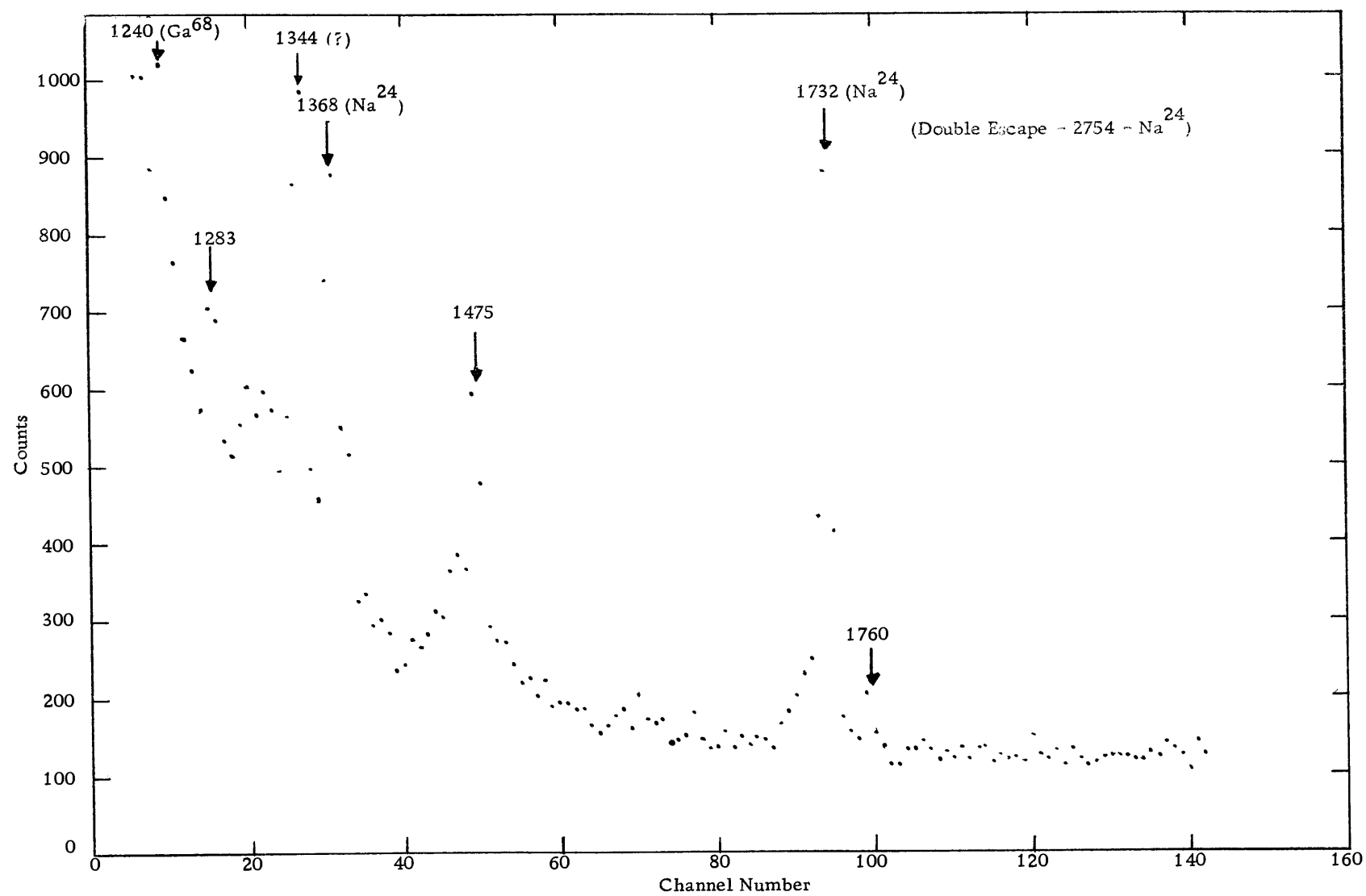


Figure 8.  $\text{Zn}^{71}$  gamma ray spectrum. 1200-2000 kev.



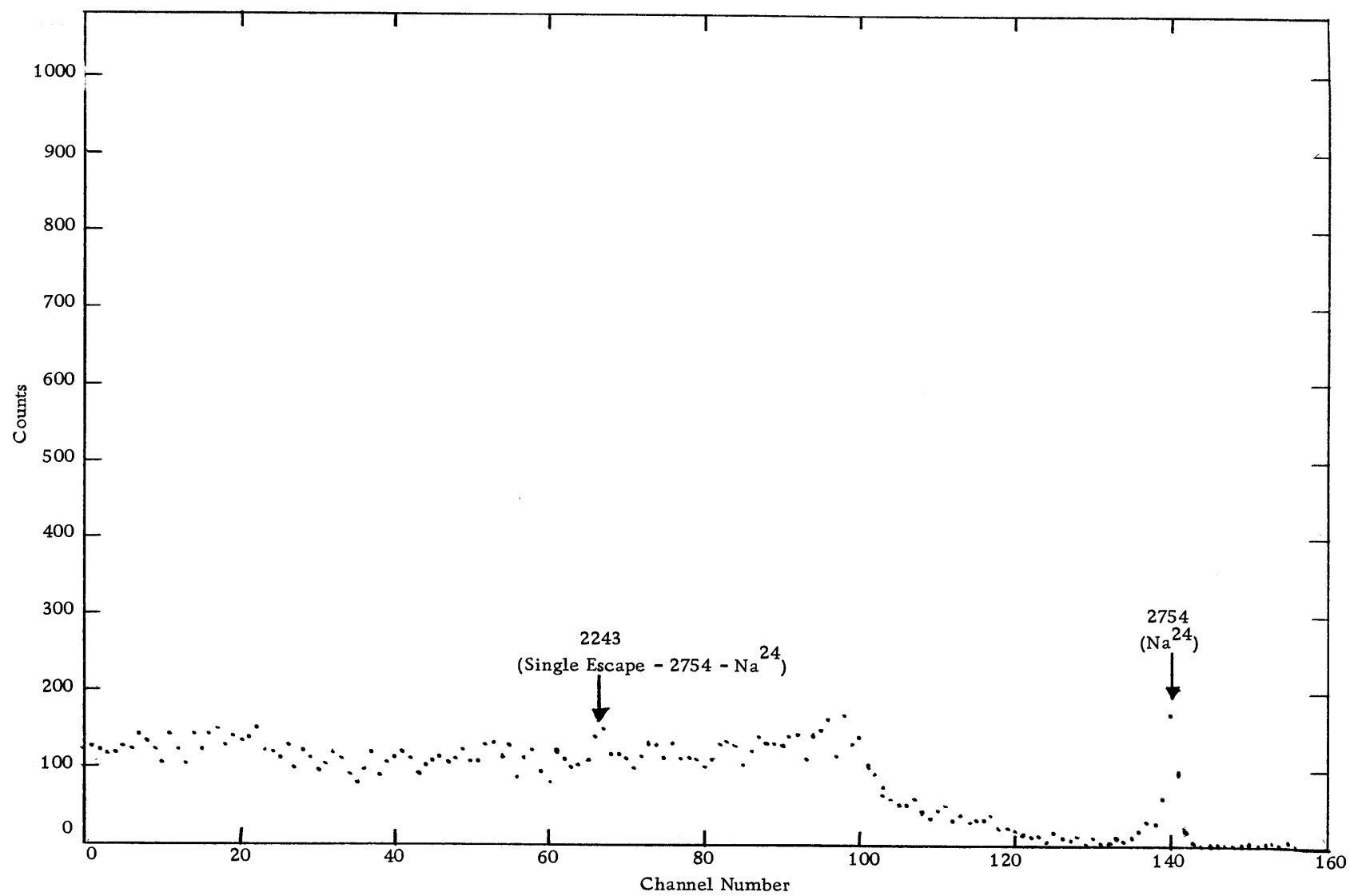


Figure 9. Zn<sup>71</sup> gamma ray spectrum. 2000-2800 kev.

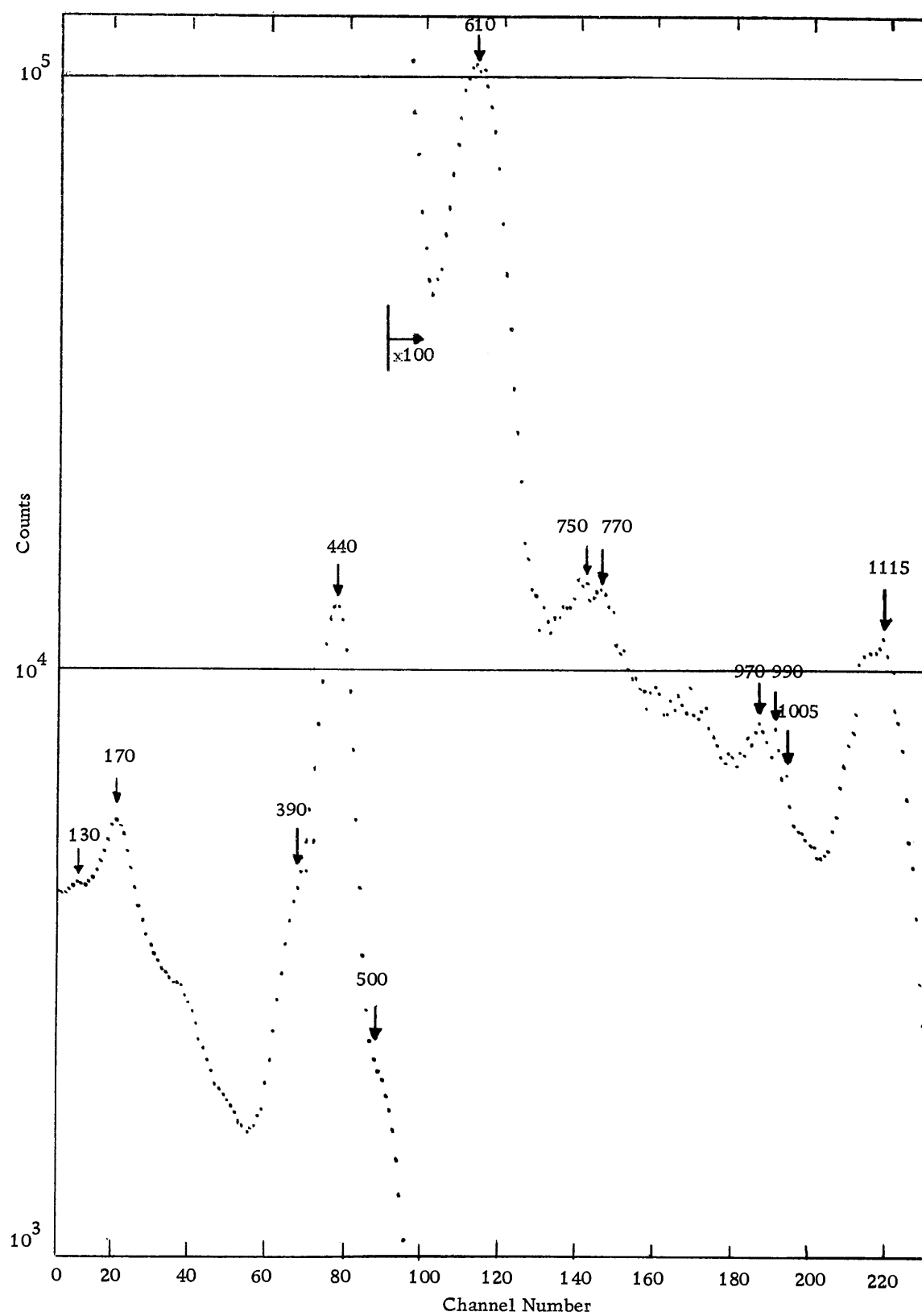


Figure 10.  $\text{Zn}^{71}$  gamma ray spectrum from Na I detector.

small that this method could not be used. By calculating the ratio of their peak amplitude relative to that of a "known" gamma ray, the peak in question was identified as belonging to the  $\text{Zn}^{71}$  decay if the ratio remained constant for spectra taken at later times. For several of the gamma rays, neither method was applicable due to the presence of the strong impurity radiations. Thus, the 512, 1108, and 1140 kev gamma rays could not be directly identified by half life.

The 439 kev gamma ray had a half life of about 15 hours and was attributed to  $\text{Zn}^{69}$ . The peaks at 1368, 1732, and 2754 kev had half lives of the order of 15 to 17 hours. This data, combined with some other information discussed later, identified these lines as originating with  $\text{Na}^{24}$ . The 1115 kev peak had a very long half life, and it is attributed to 245 day  $\text{Zn}^{65}$ .

Until recently, there were few isotopes whose gamma ray energies had been measured to a precision of 0.1 kev particularly, for energies above several hundred kev. However, the Ge(Li) detector is well suited for such measurements and was used here for this purpose. The precision of the measurements play an important role in deducing the decay scheme, as will be discussed in a later chapter.

Calibration sources used are listed in Table 1. These sources were placed in front of the detector both before and after each run to check for possible shifts in the calibration. The source itself

Table 1. Calibration sources.

Isotope	Energy (kev)	Reference <sup>*</sup>
Se <sup>75</sup>	121. 12 $\pm$ 0. 01	a
	135. 99 $\pm$ 0. 02	
	264. 62 $\pm$ 0. 07	
	279. 57 $\pm$ 0. 08	
	400. 7 $\pm$ 0. 2	
Sb <sup>124</sup>	602. 8 $\pm$ 0. 1	b
	1691. 3 $\pm$ 0. 3	
	2090. 7 $\pm$ 0. 5	
Sc <sup>46</sup>	888. 3 $\pm$ 0. 4	b
	1119. 2 $\pm$ 0. 6	
Co <sup>57</sup>	121. 97 $\pm$ 0. 03	c
	136. 33 $\pm$ 0. 03	
Hg <sup>203</sup>	279. 15 $\pm$ 0. 02	c
Na <sup>22</sup>	511. 006 $\pm$ 0. 002	c
	1274. 7 $\pm$ 0. 2	
Bi <sup>207</sup>	569. 62 $\pm$ 0. 06	c
	1063. 51 $\pm$ 0. 08	
Cs <sup>137</sup>	661. 595 $\pm$ 0. 076	c
Zn <sup>65</sup>	1115. 6 $\pm$ 0. 18	c
Co <sup>60</sup>	1173. 226 $\pm$ 0. 040	c
	1332. 483 $\pm$ 0. 046	
Na <sup>24</sup>	1368. 526 $\pm$ 0. 044	c
	2753. 92 $\pm$ 0. 12	

<sup>\*</sup> a = Reference 15, b = Reference 30, and c = Reference 29.

contained calibration lines due to the  $\text{Zn}^{65}$  and  $\text{Na}^{24}$ . For each run, enough counts were accumulated in each peak until the peak was well defined, usually, several thousand counts at the maximum. For the very weak, high energy gamma rays this required several hours of accumulation time. Fortunately, the peaks due to the impurities provided the calibration points in this region so that drifts in the electronics were not important.

An important problem which arose was a shift in pulse height with counting rate. The shift is a result of baseline distortion in the amplifier. This effect could have been reduced by using double delay line pulse shaping in the amplifier to give short bipolar pulses, but this choice results in decreased resolution. Another solution is to mix the calibration sources with the  $\text{Zn}^{71}$  source. However, this procedure is awkward and the multitude of weak gamma rays made identification and measurements difficult as it was. Instead, a source holder and a proportional counter were arranged in a standard geometry so the source-detector distance could be varied until the total chamber current was the same for both the calibration sources and the  $\text{Zn}^{71}$  source. Using this procedure, shifts could be reduced below detectable levels.

Another serious problem encountered was the non-linearity of the TMC multichannel analyzer in the first one hundred channels. The last three hundred channels were used, therefore, for most of

the energy measurements. When a Nuclear Data 512 Channel Analyzer became available, which was very linear over all channels, the energy values were checked for reliability.

The exact position of a gamma ray photopeak in the spectrum was determined with a precision of less than 0.1 channels. Photo-peaks of a germanium detector are very slightly asymmetric, the low energy side having a smaller slope. This is due to processes in the crystal which lead to small amounts of energy loss and partly to count rate effects in the amplifier. The peak was plotted on a linear scale and fitted with a triangular shape; the slope of the sides being chosen as equal to that of the high energy side where no distortion occurs. One point was chosen on the low energy side with a line of proper slope drawn through it. The intersection of the two sloping lines thus determines the peak position. For several weak gamma rays located near strong peaks, this procedure was not possible; an estimated position was determined, hence the errors are larger.

The calibration data for each run were used to calculate least squares parameters to a linear function  $E = a(CN) + b$ , from which the gamma ray energies were determined. Results are shown in Table 2. Errors represent the standard errors involving at least ten measurements. No account is made for any possible systematic errors. Uncertainties associated with the least squares parameters,  $a$  and  $b$ , were determined by propagating the uncertainties in  $E$  and

CN for the calibration sources. Errors so calculated were four or five times smaller than the standard errors and are not significant.

Table 2. Energies and relative intensities of gamma rays of  $\text{Zn}^{71}$  decay.

Gamma Ray Energy (kev)	Relative Intensity
$122.2 \pm 0.1$	$2.3 \pm 0.5$
$143.4 \pm 0.2$	$5.1 \pm 1.1$
$386.8 \pm 0.1$	100
$488.0 \pm 0.1$	$63 \pm 13$
$511.7 \pm 0.1$	* $28 \pm 6$
$596.2 \pm 0.1$	$28 \pm 6$
$620.4 \pm 0.1$	$64 \pm 13$
$753.2 \pm 0.2$	$2.6 \pm 0.6$
$771.3 \pm 0.3$	$1.2 \pm 0.3$
$964.5 \pm 0.1$	$3.9 \pm 1.2$
$987.8 \pm 0.1$	$0.9 \pm 0.2$
$1007.0 \pm 0.2$	$1.2 \pm 0.3$
$1108.2 \pm 0.2$	---
$1140.4 \pm 0.2$	---
$1283.4 \pm 0.6$	$0.2 \pm 0.1$
$1475.6 \pm 0.2$	$0.5 \pm 0.2$
$1758.4 \pm 0.7$	---

\*Deduced from the decay scheme, and from coincidence experiments.

It is of interest to note that the best measurement of the energy of the gamma ray in  $\text{Zn}^{69}$  previous to the present experiment was  $438.9 \pm 0.7$  kev (31). The result of these measurements,

$438.8 \pm 0.1$  kev, is an improvement which demonstrates the value of the Ge(Li) detector in energy measurements.

By biasing out the lower energy part of the gamma ray spectrum, using the Bias Amplifier, any portion of the spectrum could be isolated and expanded. Thus, a peak would be spread over 15 or 20 channels. Long counting periods were used so total numbers of events accumulated ran as high as  $10^7$  counts. The spectrum shapes were smooth which made accurate background subtraction possible. Ratios of peak areas relative to that of the 387 kev gamma ray (the most intense and chosen as the reference intensity) were calculated. These ratios do not represent the relative intensities because of the dependence of the detection efficiency on energy. For this reason the relative efficiency curve, Figure 11, was determined using calibration sources with gamma rays having known relative intensities.<sup>1</sup> Note that the errors associated with the calibration data are of the order of 15 to 20%. These uncertainties are the main source of error listed in Table 2. The photoelectric and pair production cross sections for germanium are shown in Figure 11 (22). Note that the photoelectric cross section is a straight line over the energy region 100 to 1000 kev. A straight line was drawn through the calibration points of the relative efficiency curve since it is expected this is the

---

<sup>1</sup>The data was obtained and analyzed by Mr. Donald A. Walker.



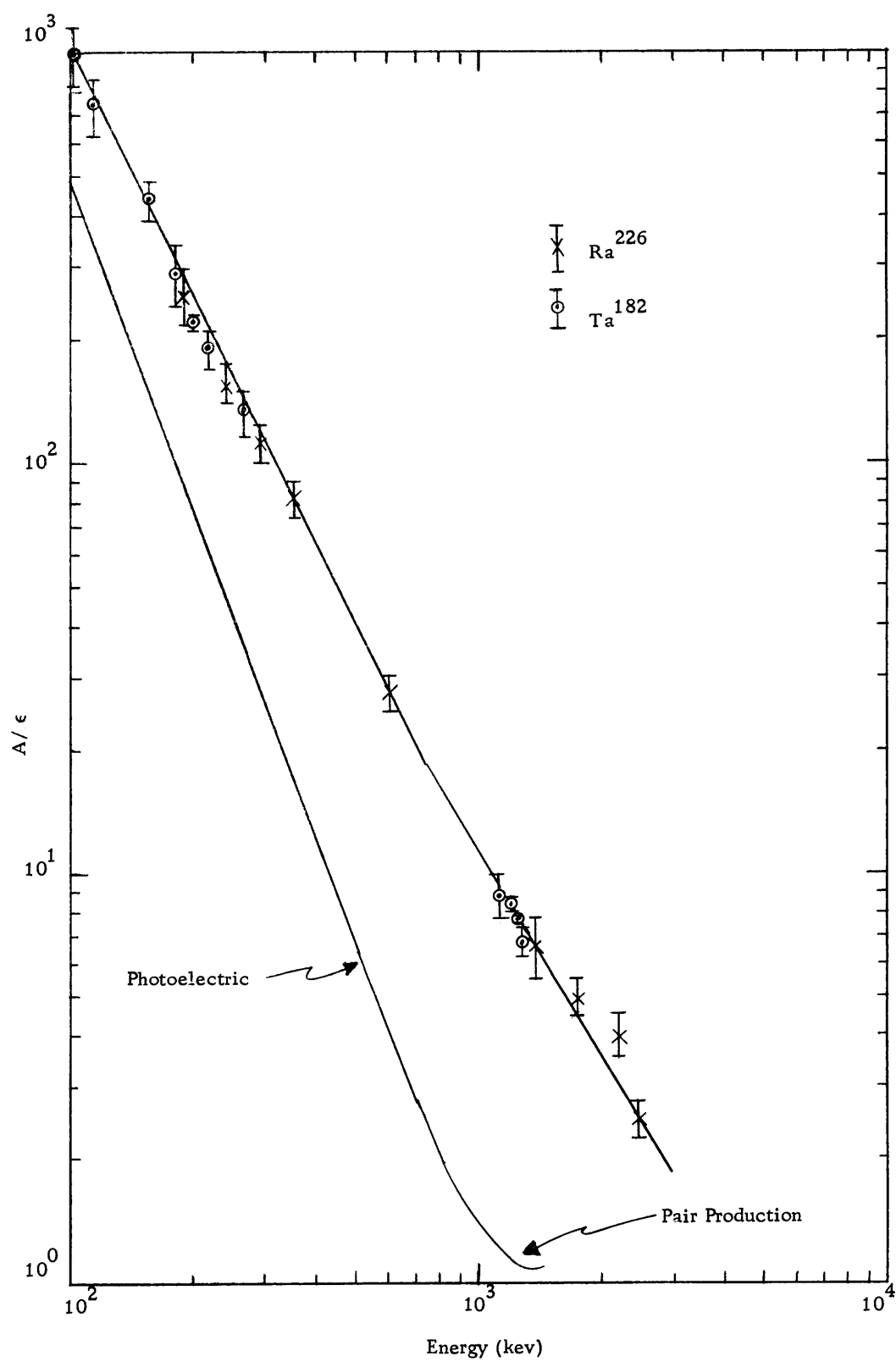


Figure 11. Relative efficiency curve.

major contributing process to the cross section. The Compton process also occurs but will not contribute to the photopeak. The probability is small for multiple process events which lead to total energy absorption since the crystal is small. Thus, the total energy peak efficiency should not differ from that of the photoelectric cross section, the reason for fitting the data with a straight line. The absolute magnitude of the efficiency is not easily obtained, being dependent on crystal shape, size, counting geometry, and the physical properties of each crystal.

The calibration data is actually plotted with  $\epsilon = A/I$ , where  $A$  is the peak area and  $I$  is its relative intensity. Calculations will involve the ratios  $r_{12} = A_2/A_1$ , and the relative intensities become:

$$\frac{I_1}{I_2} = r_{12} \frac{\epsilon_2}{\epsilon_1}$$

Below 1000 kev the data was fitted by a least squares analysis to a linear function,  $\log \epsilon = a \log E + b$ , from which the efficiencies were calculated as a function of energy. Above 1000 kev the calibration points were fitted by a least squares line also. Actually, the pair production cross section, which becomes important at these energies, gives rise to a non-linear total energy peak cross section. However, the curvature is small and large uncertainties in the calibration data suggest a linear fit is an appropriate approximation.

Table 2 shows results of the measurements; errors include an average of 15% from the calibration data compounded with the standard errors resulting from at least six measurements. The relative intensity of the 512 kev gamma ray could not be measured due to the positron emitting impurities present. The value quoted in the table is deduced from the decay scheme and coincidence data. The 1140 and 1758 kev transitions were too weak to be measured, and the 1108 kev peak was too close to the 1115 kev line.

Intensity measurements in the region above 1000 kev were difficult to make. Low detector efficiency and low intensities created a problem of identification which was further hindered by the presence of impurities. Frequently, very small peaks would appear in the spectra but were too small to be identified; it is possible that some of these weak peaks might be related to  $\text{Zn}^{71}$ . Several gamma rays could not be identified, but these could be rejected on the basis that they decayed either faster or slower than  $\text{Zn}^{71}$ . Many were radiations from minute quantities of gallium isotopes which remained after the extraction process. As mentioned earlier, the  $\text{Na}^{24}$  could not be explained, but it has a simple spectrum and a relatively long half life of 15 hours. Identification was based on the half life of the 1368, 1732 and 2754 kev peaks, their energies, and similarity with the spectrum reported by Hollander (22). Of particular interest is the large peak at 1732 kev in Figure 8. For a gamma ray of this

energy and intensity there should be a very prominent Compton distribution with an edge at 1510 kev. Absence of such a distribution requires that the 1732 kev peak be the result of an energy loss process. The only process to consider is that of the escape of the annihilation gamma rays following pair production. The probability for this process increases very rapidly above energies of 1022 kev (22).

As a further check on the origin of the impurities, pure zinc foils<sup>2</sup> were bombarded. No essential differences in the gamma ray spectrum was observed. The only other way the Na<sup>24</sup> could arise was from some contamination deposited during the handling of the target foils.

Coincidence results are shown in Figures 12 through 16. These results assure the following relationships: 387-488-620 and 387-512-596. However, the order of the cascades is not determined. The only other information is not conclusive. Figures 17 and 18 are the coincidence results when the analyzer windows are set for the 940-1020 and the 1035-1085 kev regions, respectively. It is apparent that the 143 kev gamma ray is in coincidence with either the 965, the 987, or the 1007 kev gamma rays, or with all of them. Low intensities and low detector efficiencies prevented use of the alternate method in which analysis occurs in the Ge(Li) channel. The fact

---

<sup>2</sup>High purity zinc foil, less than 0.001% of any impurity, was obtained from A. D. Mackay, Inc. New York, N. Y.

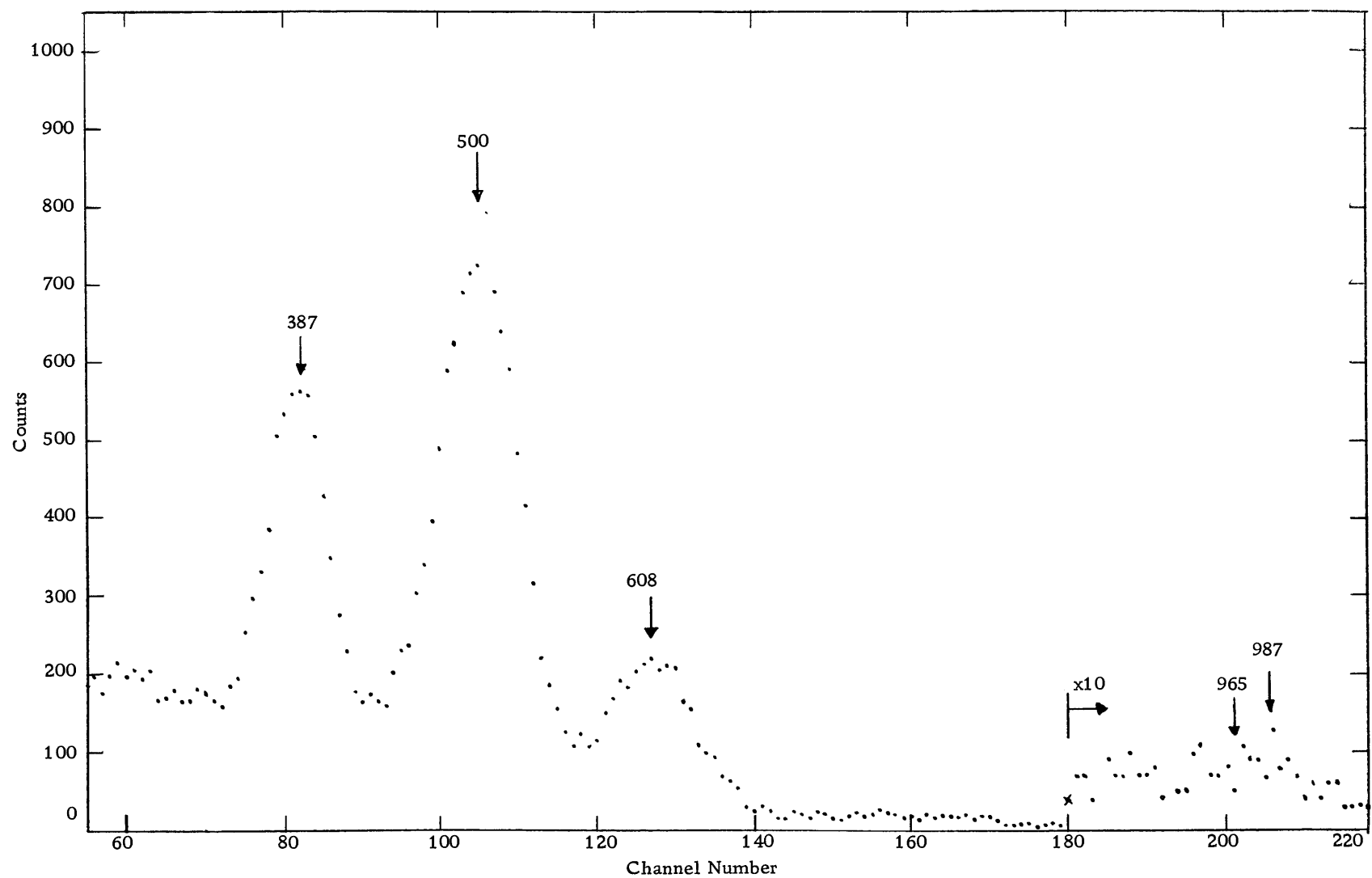


Figure 12. Gamma-gamma coincidence. Ge(Li) gate - 387.

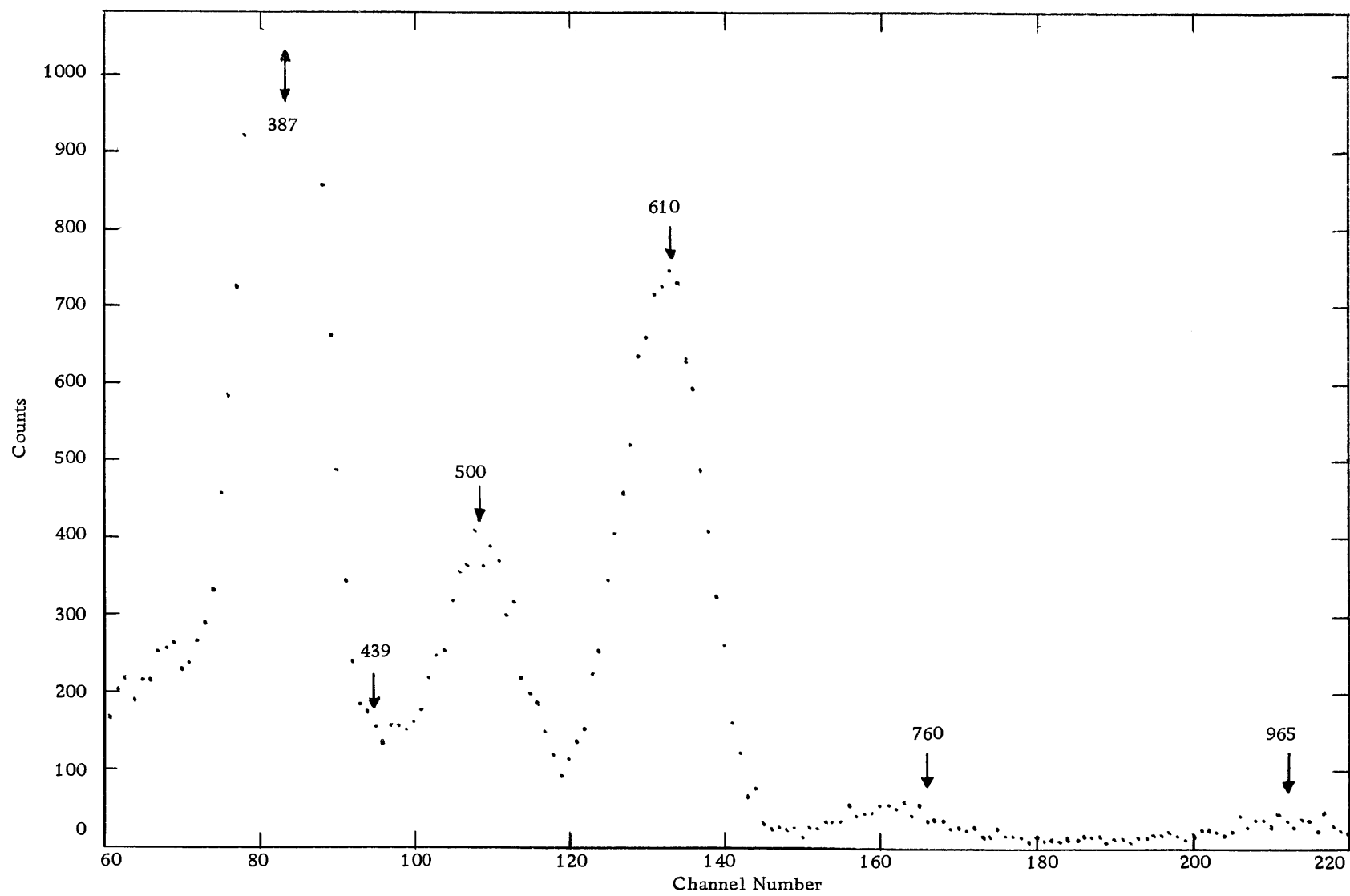


Figure 13. Gamma-gamma coincidence. Ge(Li) gate - 488.

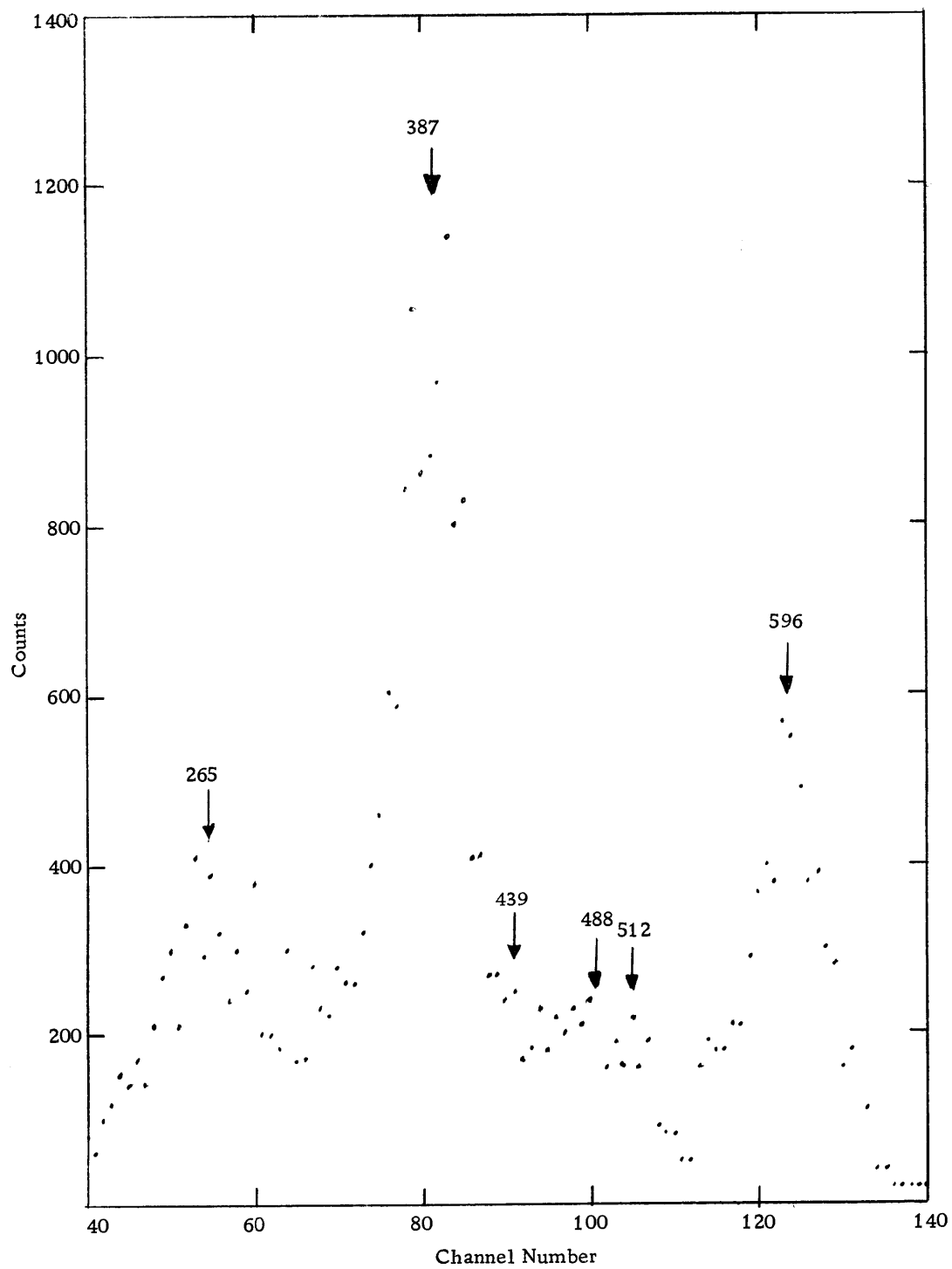


Figure 14. Gamma-gamma coincidence. Ge(Li) gate - 512.

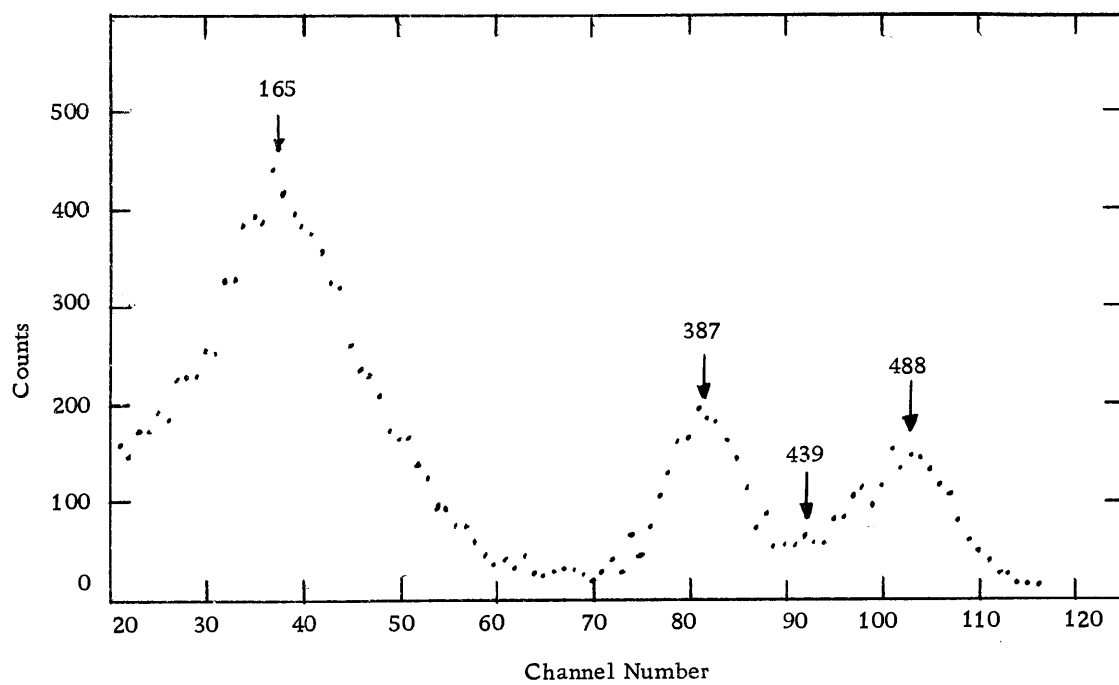


Figure 16. Gamma-gamma coincidence. Ge(Li) gate - 620.

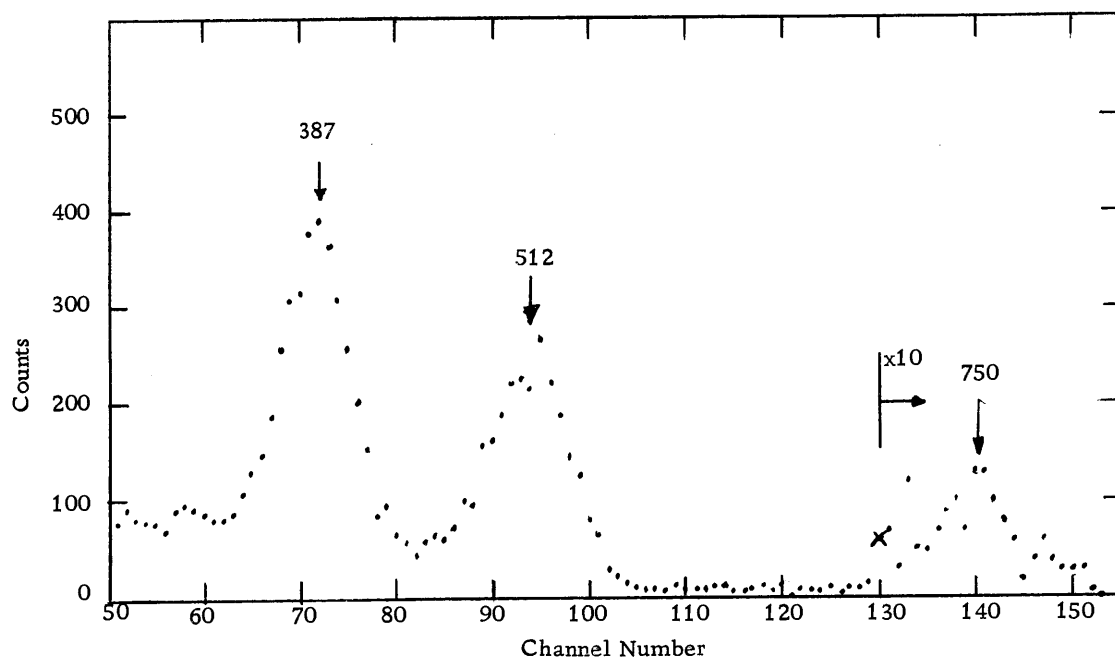


Figure 15. Gamma-gamma coincidence. Ge(Li) gate - 596.



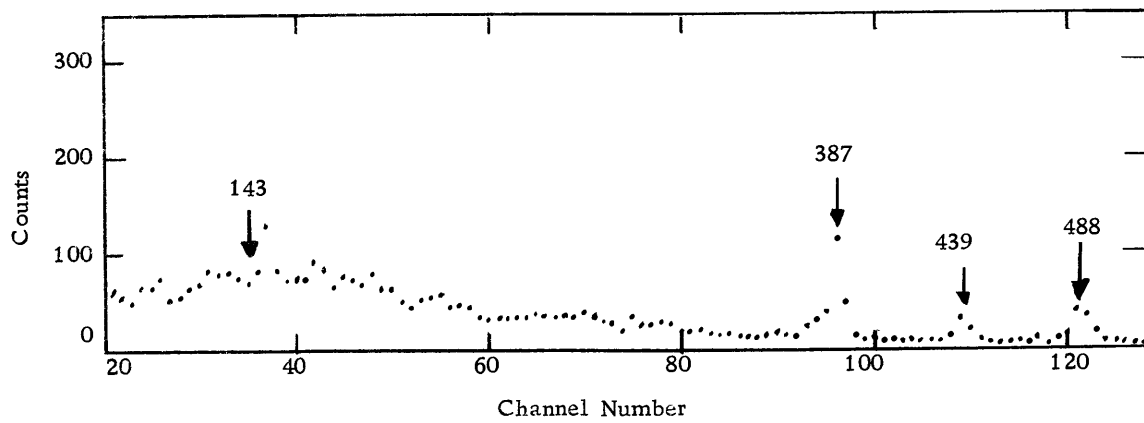


Figure 18. Gamma-gamma coincidence. Na I gate - 1040 to 1090 keV.

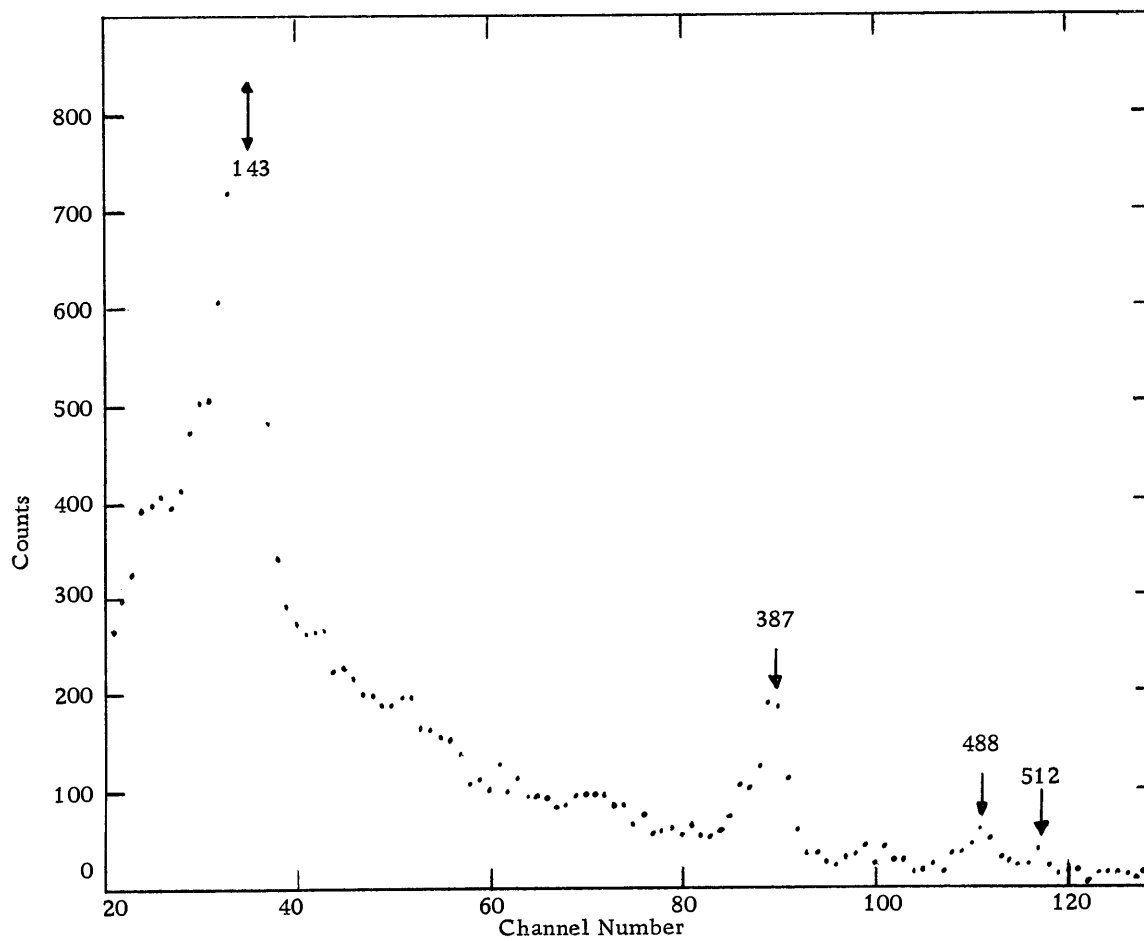


Figure 17. Gamma-gamma coincidence. Na I gate - 940 to 1020 keV.

that the 387, 488, and 512 keV peaks appear in both Figures 17 and 18, implies that they are in coincidence with a high energy gamma ray whose Compton distribution falls within the analyzer window.

Typical delayed coincidence experimental results are shown in Figure 19 for the 610-500 keV transitions. There appears to be no difference between the data for the  $\text{Zn}^{71}$  source and that of the prompt peak using annihilation gamma rays. Similar results are found for the 610-390 and 500-390 keV coincidences.

The presence of impurities prevented any beta ray measurements. The very strong 900 keV beta rays from  $\text{Zn}^{69}$  and the 1390 keV beta rays from  $\text{Zn}^{65}$ , completely dominated the much less intense electron spectrum from  $\text{Zn}^{71}$ . The use of beta-gamma coincidence methods was rejected as unfeasible. The large Compton backgrounds in the energy regions of interest would have contributed large coincidence backgrounds also. In the next chapter, some information on the energies and branching ratios of the beta decay will be deduced on the basis of the decay scheme and the gamma ray relative intensities.

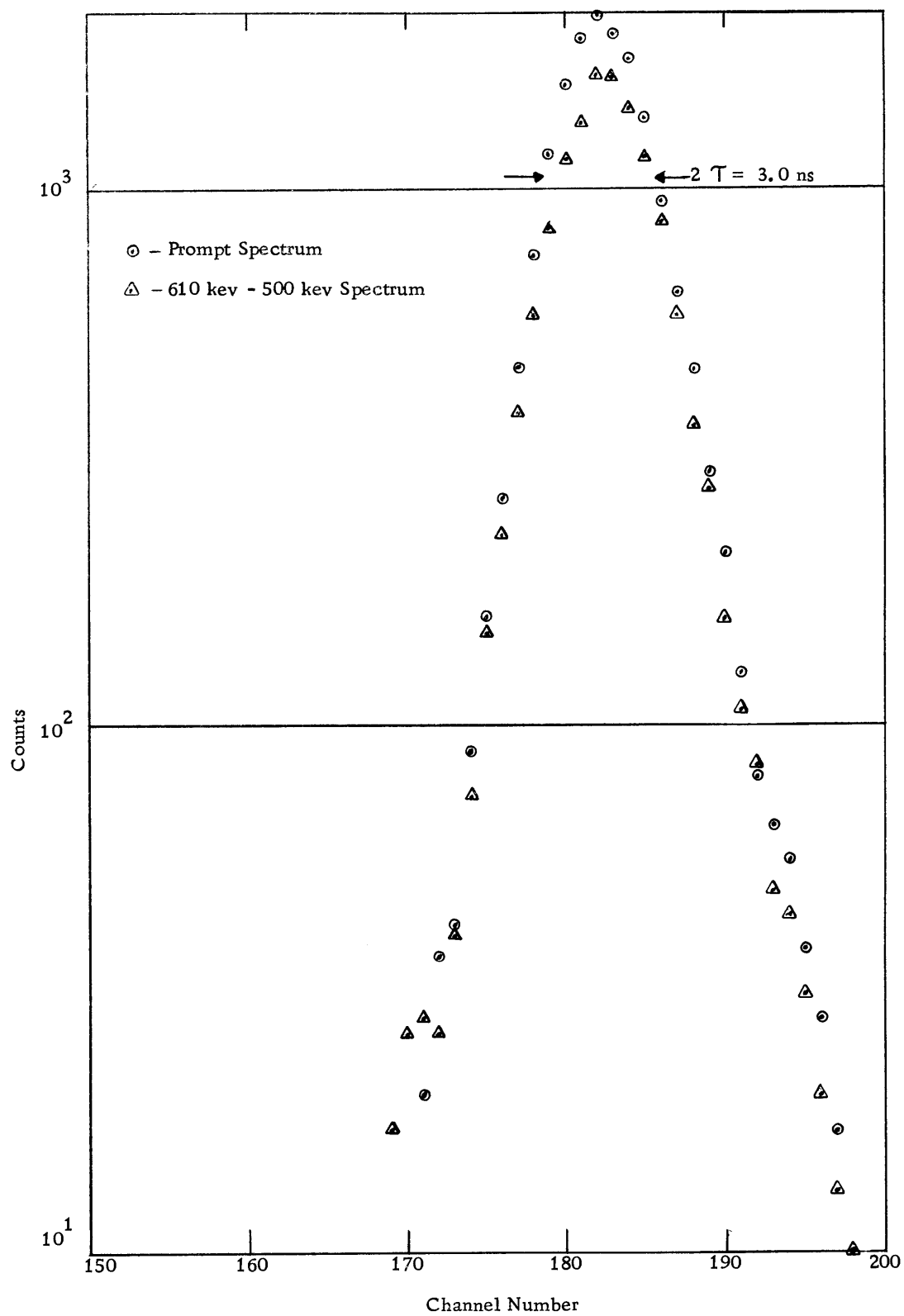


Figure 19. Delayed coincidence. 610 - 500 kev.

## DECAY SCHEME OF $\text{Zn}^{71}$

Figure 20 shows the decay scheme which was determined.

From the fact that a 513 kev level is excited in Coulomb excitation (16), and apparently no others, the 512 kev transition was placed at the bottom of the decay scheme. The 596 and 387 kev transitions formed the rest of the cascade giving rise to levels at 1108 and 1495 kev. The other coincidence cascade, 488-620-387 kev was then introduced producing only one additional level since the sum relationship of the  $512 + 596$  and the  $488 + 620$  kev gamma rays both agree accurately with the cross over transition energy of  $1108.2 \pm 0.2$  kev (within the experimental error!). Further use of the high precision of the measurements places the 1007 kev gamma ray as the transition between the 1495 and 488 kev levels. The 1475 kev gamma ray was assumed to be a transition to the ground state, and then the 987 fits into the scheme between the 1475 and 488 kev levels.

Tandon and Devare, in their study of  $\text{Zn}^{71}$  (42), displayed a total gamma ray absorption spectrum which is reproduced in Figure 21. Since an energy level at 2440 kev, indicated in this study, agrees exactly with the sum of the energies of 964.5 and 1475.6 kev, the 965 kev transition was placed in this cascade. The 143 kev transition was then placed on top of this to satisfy the coincidence relationships. The 143 was placed in coincidence with the 965 rather

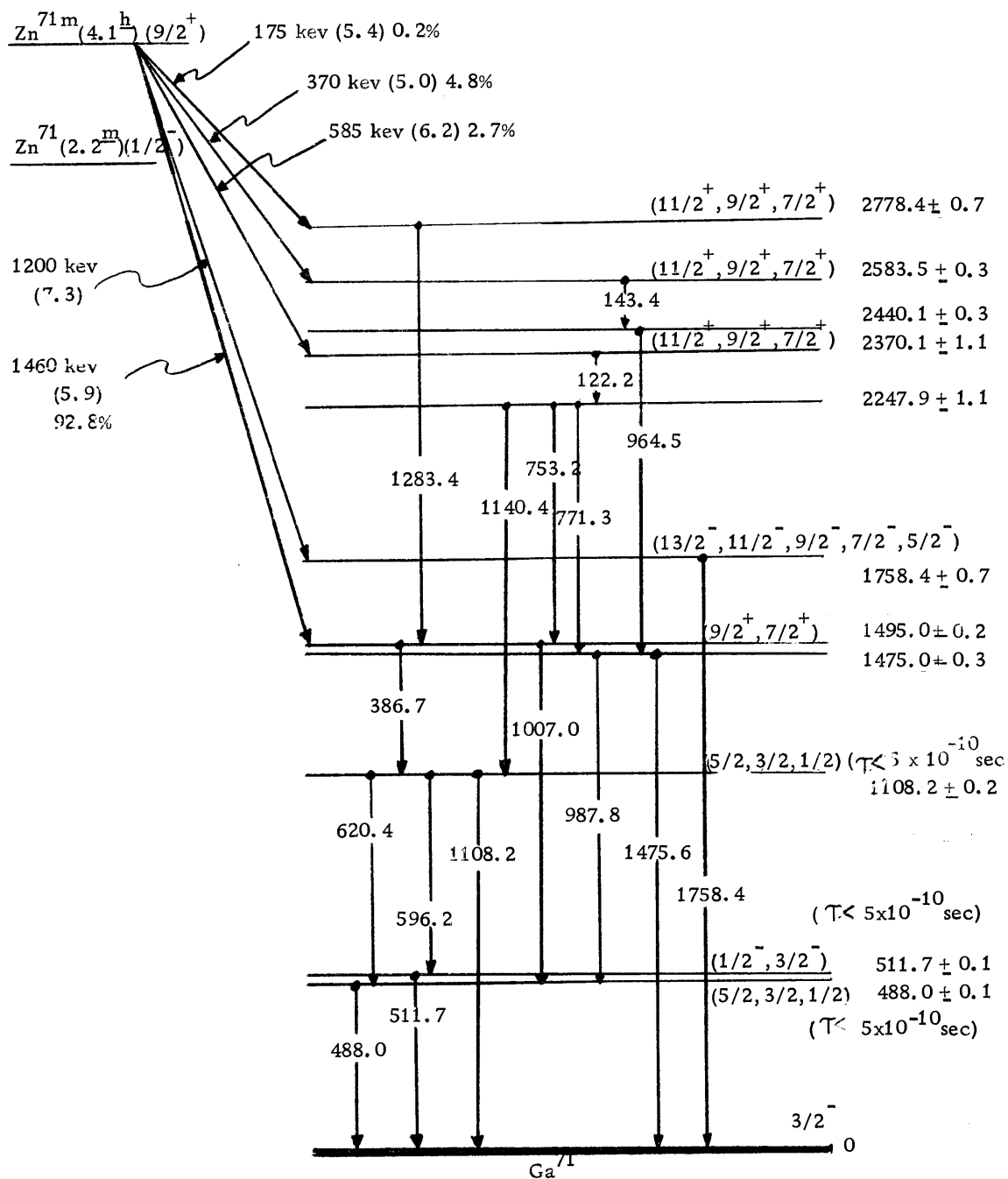


Figure 20. Decay scheme of 4.1 hour  $^{71}\text{Zn}$ .

than the 987 or the 1007 because of the indication of a sum peak at 2583 keV in the total absorption spectrum. The level at 2247 keV was chosen since there were three separate cascades which had an energy sum equal to this number. Further, the sum peak appears in Figure 21 at 2250 keV. The 1758 keV level was introduced as a separate state, due to the evidence of a small peak at 1760 keV in the total absorption spectrum. The position of the 122 keV transition posed a difficult problem, but it was finally placed above the 2247 level since there is a slight suggestion of a sum peak at 2370 keV in Figure 21.

The beta ray branching was deduced from the relative intensity data, as suggested previously. The uncertainties are quite large, but the results indicate the absence of branching to states below the 1495 keV level. In deducing these results, the only assumption made was that the branching to the ground state was zero. This is argued as follows: The absence of the 350 keV transition between isomeric states in  $\text{Zn}^{71}$  implies that a large angular momentum change is involved. In  $\text{Zn}^{71}$  the  $2p_{1/2}$  and  $1g_{9/2}$  levels are being filled which is a characteristic of many nuclei with long lived isomeric states associated with M4 transitions. Since the ground state of  $\text{Zn}^{71}$  decays by allowed beta decay to the  $\text{Ga}^{71}$  ground state whose spin is  $3/2^-$ , it is reasonable to assume that the  $\text{Zn}^{71}$  ground state is  $1/2^-$ . The

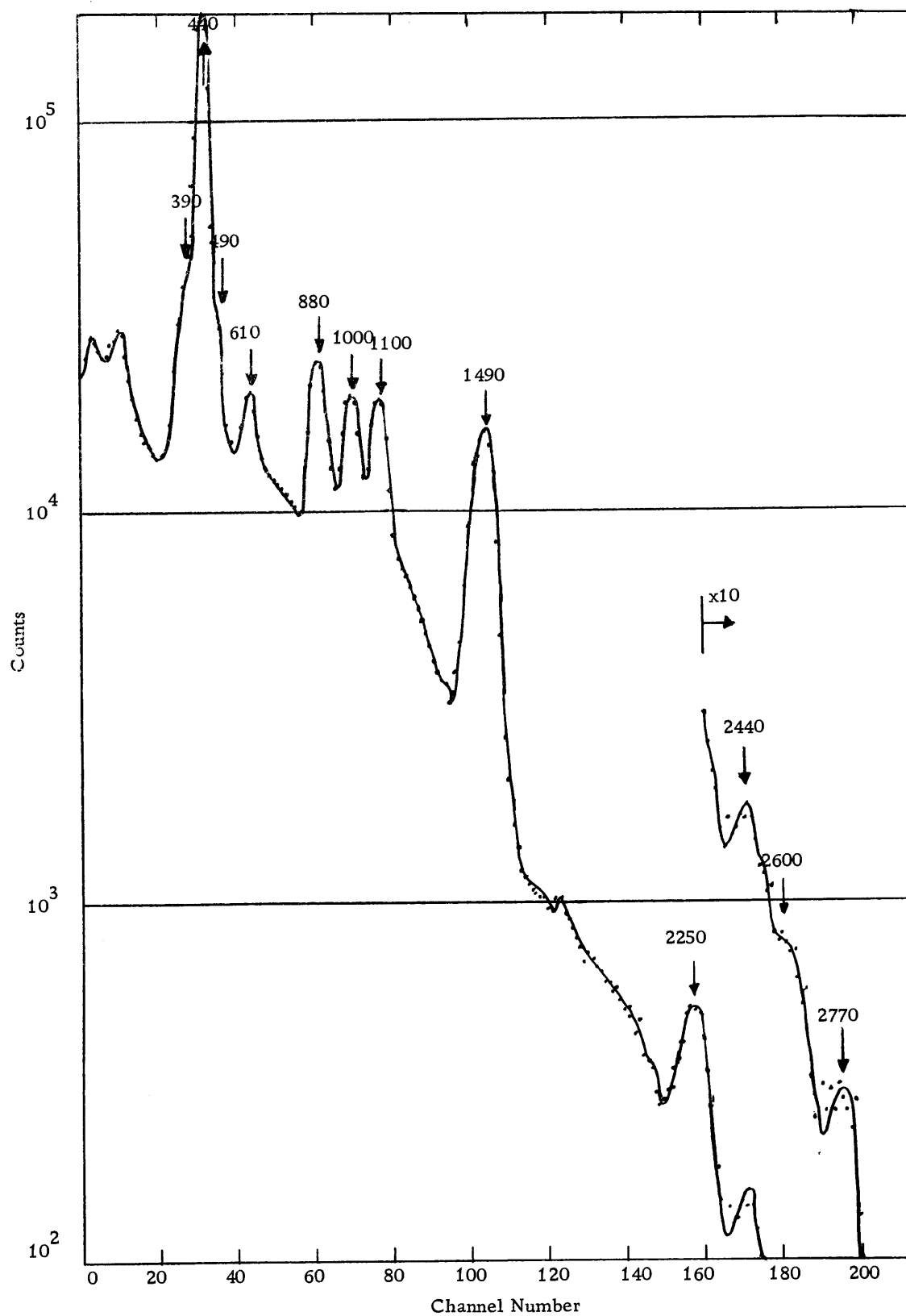


Figure 21. Total absorption gamma ray spectrum of  $\text{Zn}^{71}$ .

$\text{Zn}^{71m}$  state must then be  $9/2^+$ . Now, a beta transition from the  $9/2^+$  level to the  $3/2^-$  ground state in  $\text{Ga}^{71}$  would be at least third forbidden. The low branching ratios for the lower energy beta transitions explain why they would not be seen when superimposed upon the spectrum of the 1460 kev beta ray to the 1495 kev level found by Sonnino, Eichler, and Amiel (40).

The log ft values were calculated as follows: let

$\lambda_i$  = partial decay probability for the  $i$  th beta ray component,

$\beta_i$  = branching ratio to levels in  $\text{Ga}^{71}$  of the  $i$  th component,

$T_{\frac{1}{2}} = 4.1$  hour half life of  $\text{Zn}^{71}$

then

$$t_i = T_{\frac{1}{2}} / 0.693 \beta_i \quad (3-1)$$

The values of  $f(Z, E_e)$  were taken from tables for the analysis of beta decay data (45) and then

$$\log(ft)_i = \log_{10}[f(Z, E_e) \cdot t_i] \quad (3-2)$$

Energy levels of the decay scheme agree with the total absorption spectrum of Tandon and Devare, obtained using a 3" x 3" NaI well crystal. Tandon and Devare indicate on their figure the presence of sum peaks at the following energies: 390, 490, 610, 880, 1000, 1100, 1490, 2250, 2440, 2600 and 2770 kev. Further, a careful observation of the spectrum indicates a weak line at 1760 kev.



The poor resolution of NaI does not permit the separation of the various gamma ray complexes, and the energies cannot be measured as precisely as is possible with germanium detectors. With the exception of the 880 and the 1000 kev lines, all of these energies agree with the levels deduced for  $\text{Zn}^{71}$ . The 880 kev peak is probably the sum of the 390 and the 490, which still agrees with the scheme, as does the 1000 kev peak if it is the sum of the 390 and the 610. The sum peak intensities agree with those found by summing the individual gamma ray intensities.

On the basis of the Weisskopf single particle estimates for lifetimes of electromagnetic transitions in nuclei (5), the results of the delayed coincidence measurements show that each of the levels, 1108, 512 and 488 kev must decay either by E1, M1 or E2 radiations. Thus, a few things can be deduced about the spin assignments of these levels.

In Figure 22 the decay scheme of 2.2 minute  $\text{Zn}^{71}$  is shown (44). Transitions to both the 512 kev level and the ground state are both allowed which implies these levels must have spins of either  $1/2^-$  or  $3/2^-$ . This conclusion is based on the assumption of the spin assignments to the  $\text{Zn}^{71}$  states as  $1/2^-$  and  $9/2^+$ . The negative parity of the 512 kev level is suggested by the Coulomb excitation experiment (16).

If the 488 kev level had a spin of  $9/2$  or greater, with either

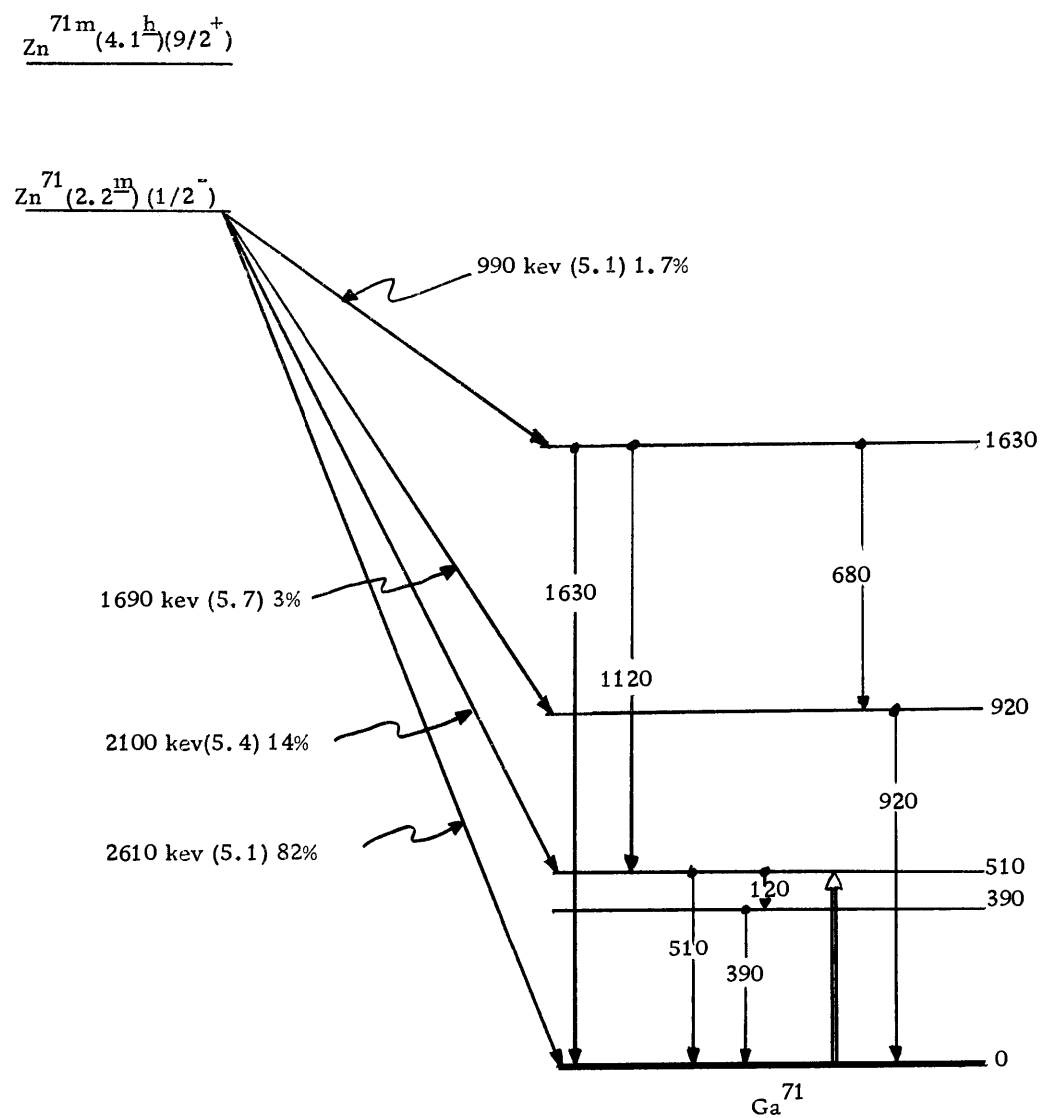


Figure 22. Decay scheme for 2.2 minute activity of  $\text{Zn}^{71}$ .

positive or negative parity, the lifetime of the state would have been long enough to be measured. If the spin were  $7/2^-$ , the level should have been produced by Coulomb excitation. If the spin were  $7/2^+$ , an M2 transition would be involved. Thus, it is argued that the 488 kev level has a spin of  $5/2$ ,  $3/2$ , or  $1/2$ .

The same arguments hold for the 1108 kev level.

Now, only the 1495 kev level is strongly fed by beta decay from  $\text{Zn}^{71}$ . The log ft value of 5.9 suggest an allowed transition. On the basis of the  $\text{Zn}^{71m}$  level being  $9/2^+$ , the 1495 kev level is either  $11/2^+$ ,  $9/2^+$ , or  $7/2^+$ . From the arguments for the 1108 kev level having spin  $5/2$  or less, and from the fact that Li and Monaro (27) measured the lifetime to be  $1.54 \times 10^{-10}$  seconds, it is concluded that the  $11/2$  spin possibility can be discarded since it would lead to a longer lifetime.

It must be emphasized that this decay scheme in Figure 20, is not unique, although the total absorption spectrum supports the level assignments. Note, for example, that the sum of 987.8 and 771.3 is just 1759.1, which agrees very closely with the measured transition energy of 1758.4 kev; in fact, their errors overlap. Thus, three alternative possibilities for these transitions are shown in Figure 23. In the first case, a, the level at 1758 does not appear; in the second case, b, a level appears at 987 kev; and third, case c, a level at 771 kev is inserted. The beta ray branching will not change

appreciably as the gamma rays involved have low intensities. The branching to the 1758 level becomes about 1% for cases b and c. In Figure 21 there is no evidence for a peak at 770 kev. This suggests that case c may be rejected. The 987 kev level of case b, could not be resolved from the 1000 kev peak of Figure 21, so case b is a possibility. Note, however, that the 1760 peak observed would have to be explained as a single gamma ray transition and, from Table 2, this is very weak. Case a cannot be rejected for similar reasons.

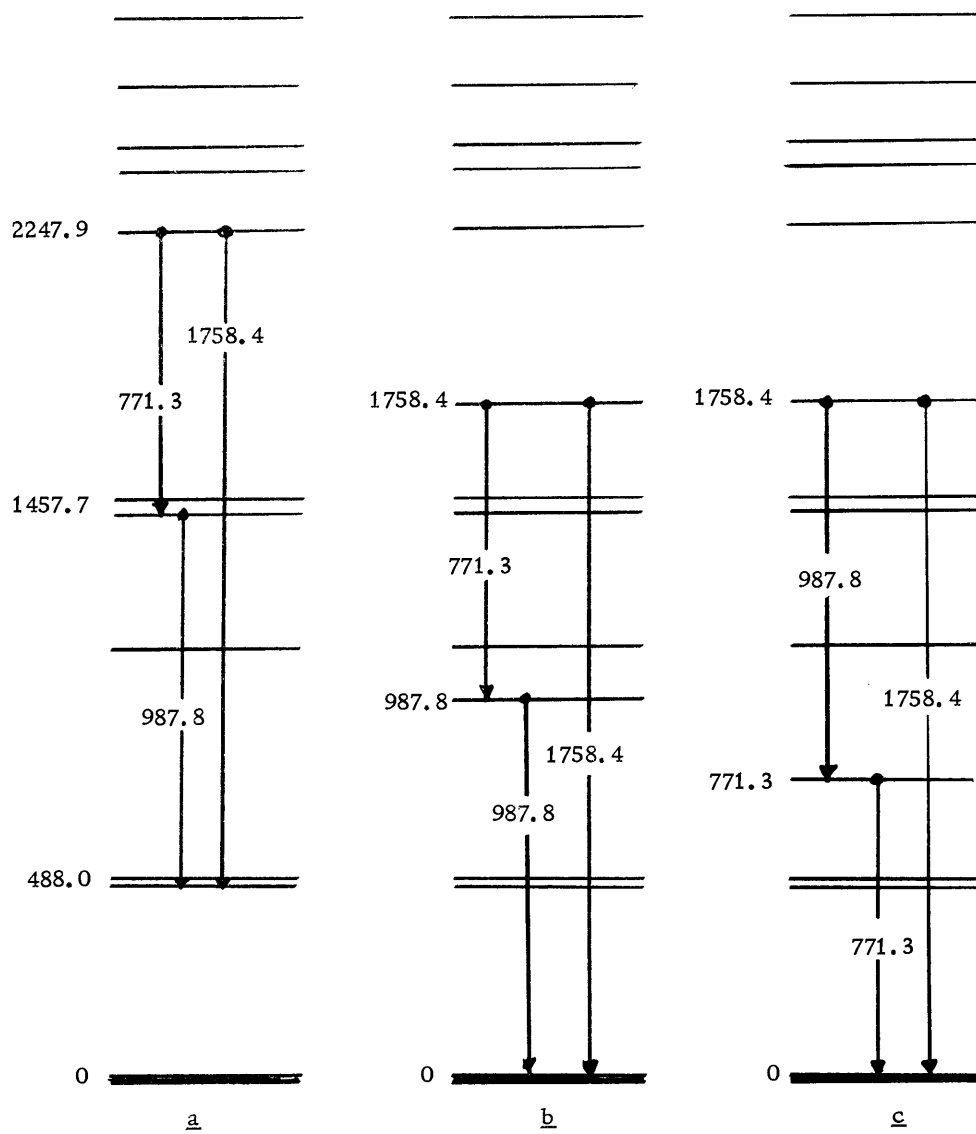


Figure 23. Alternative level schemes for  $\text{Ga}^{71}$ .

# UNIFIED MODEL FOR GA<sup>71</sup>

## Introduction

Bohr and Mottelson (7) first suggested the unification of the collective model with the single particle model. In one form, excited states of odd mass nuclei are described as arising from an interacting vibrating core and a single extra nucleon. More fundamental approaches have been developed in terms of the excitation of quasi-particles and phonons, such as the treatment of Kisslinger and Sorensen (24) on spherical nuclei. The model described here is closer to the form of Bohr and Mottelson.

Excitations in spherical nuclei can be described as vibrations of the nuclear surface about an equilibrium shape. A phonon of excitation is represented as a deformation of the surface having a quadrupole,  $Y_2^\mu(\theta, \phi)$ , angular dependence. The next higher energy phonon would have an octupole representation,  $Y_3^\mu(\theta, \phi)$ . A dipole term,  $Y_1^\mu(\theta, \phi)$ , is excluded since it represents a displacement of the center of mass, which can occur only under the action of an external force.

The surface shape is described by:

$$R = R_o \left[ 1 + \sum_{\lambda \mu} a_{\lambda \mu} Y_{\lambda}^{\mu*} \right] \quad (4-1)$$

where  $R_0$  is the mean equilibrium radius. The  $a_{\lambda\mu}$  are time dependent coefficients describing the amplitude of the surface oscillations. The kinetic energy is:

$$T = \frac{1}{2} \sum_{\lambda} B_{\lambda} |\dot{a}_{\lambda\mu}|^2 \quad (4-2)$$

where  $B_{\lambda}$  is a constant, dependent on  $\lambda$ , which may take an analytic form if some model is used to represent the nuclear matter (e. g. the hydrodynamic model of Bohr (6)). The potential energy becomes:

$$V = \frac{1}{2} \sum_{\lambda} C_{\lambda} |a_{\lambda\mu}|^2 \quad (4-3)$$

where  $C_{\lambda}$  is also a constant. From the Lagrangian,  $L = T - V$ , one can derive an equation of motion from which it is seen that each generalized coordinate,  $a_{\lambda\mu}$ , satisfies an equation for a simple harmonic oscillator with frequency

$$\omega = (C_{\lambda}/B_{\lambda})^{1/2} \quad (4-4)$$

Quantization is effected by defining amplitudes  $b_{\mu}$  and  $b_{\mu}^{+}$  such that

$$a_{\lambda\mu} = \left(\frac{\hbar}{2B_{\lambda}\omega_{\lambda}}\right)^{1/2} [b_{\mu} + (-1)^{\mu} b_{-\mu}^{+}] \quad (4-5)$$

where the  $b_{\mu}$  satisfy the commutation relations:

$$[b_{\mu}, b_{\mu'}^+] = \delta_{\mu\mu'}, \quad (4-6)$$

$b_{\mu}^+$  and  $b_{\mu}$  are the boson creation and annihilation operators, respectively; if  $\lambda = 2$  then they operate on quadrupole phonon states.

$N_{\mu}$  is the occupation number of such a state, that is, the number of phonons of quadrupole order in the state. Thus,

$$\langle N_{\mu} | b_{\mu} b_{\mu}^+ | N_{\mu} \rangle = N_{\mu} + 1 \quad (4-7)$$

$$\langle N_{\mu} | b_{\mu}^+ b_{\mu} | N_{\mu} \rangle = N_{\mu}$$

The nuclear model can now be constructed. In the case of a spherical nucleus, all particles move in the same average potential; however, if there is a deformation of the surface, the particles see variations in the new potential and hence their motion is affected. This provides an interaction between the particles and the surface deformation. The total Hamiltonian becomes;

$$H = H_c + H_p \quad (4-8)$$

where  $H_c$  is the collective core Hamiltonian. For vibrational phonon states,  $H_c$  has eigenvalues  $n\hbar\omega$  where  $n = 0, 1, 2, 3, \dots$

$H_p$  is the particle Hamiltonian, and from the argument above, it must be dependent upon the surface deformation. Thus,



$$H_p = \sum_{i=1}^A [T_i + V(a_i r_i)] \quad (4-9)$$

For one particle in the field of a deformed core, the potential is taken to be of the form,  $V(r - R)$ , where  $R$  is given by equation 4-1 and defines the nuclear surface. Expanding this potential in a Taylor's Series about the mean radius  $R_o$  gives:

$$\begin{aligned} V(a, r) = V(r - R) &= V(r - R_o) + \left. \frac{dV(r - R)}{dR} \right|_{R=R_o} \Delta R + \dots \\ &= V(r - R_o) - \left[ \left. \frac{dV(r - R)}{dr} \right|_{R=R_o} R_o \sum_{\lambda \mu} a_{\lambda \mu} Y_{\lambda}^{\mu*} + \dots \right] \quad (4-10) \end{aligned}$$

The  $V(r - R_o)$  term is taken to be the spherical optical model potential with the Saxon-Woods form factor;

$$\frac{1}{1 + \exp\left[-\frac{r - R_o}{a}\right]}$$

which generates the single particle states. Then the interaction term is

$$H_{int} = - \left. \frac{dV(r - R)}{dr} \right|_{R=R_o} R_o \sum_{\lambda \mu} a_{\lambda \mu} Y_{\lambda}^{\mu*} = k(r) \sum_{\lambda \mu} a_{\lambda \mu} Y_{\lambda}^{\mu*} \quad (4-11)$$

Note from the form of  $k(r)$  that the interaction takes place only near the nuclear surface where the particle density is changing and hence  $V$  is changing. The problem is then to solve the equation

$$(H_c + H'_p + H_{int})\Phi = E\Phi \quad (4-12)$$

where

$$H'_p = \sum_{i=1}^A T_i + V(r - R_o) \quad (4-13)$$

Starting with the Schrodinger equation

$$(H_c + H'_p)\Phi_o^I = \epsilon_o \Phi_o^I \quad (4-14)$$

with

$$\epsilon_o = E_{sp}^j + E_c^R \quad (4-15)$$

the perturbation energy is

$$E_{int}^{II'} = \langle \Phi_o^{I'} | H_{int} | \Phi_o^I \rangle \quad (4-16)$$

where  $\Phi_o^I$  is a combination of the particle and core states which couple to good total angular momentum I. These basis states are

$$\Phi_o^I = |j, NR, IM\rangle = \sum_m C(jRI; mM - m) |NRR_\mu\rangle |jm\rangle \quad (4-17)$$

where  $R_\mu$  is the z component of the angular momentum of the core.

The matrix  $(E_{sp}^j + E_c^R + E_{int}^{II'})$  must be diagonalized and the eigenvalues give the energy levels of the coupled system.

### Intermediate Coupling Model

In the weak coupling limit of the model described in the above paragraphs, there is a ground state with a zero phonon core of angular

momentum  $R = 0$  coupled to one single particle state of angular momentum  $j$ . The lowest excited state is formed by coupling this single particle state to a one phonon vibrational state of angular momentum two. This excited state can have any angular momentum between values  $|j - 2| \leq I \leq j + 2$ . The degeneracy of the level is  $(2R + 1)$  or  $(2j + 1)$ , whichever is smaller.

This simple model has not been successful in describing level schemes in odd  $A$  nuclei. However, an extended version has given very good results when applied to various nuclei. This version assumes a coupling of intermediate strength. Braunstein and de-Shalit (9) applied the extended version to  $\text{Au}^{197}$ , and the energy level scheme was successfully calculated and good results were obtained for the magnetic moments of the ground and first excited states. Thankappan and True (43) assumed a parameterized spin-spin interaction for the coupling and were able to calculate the energy levels in  $\text{Cu}^{63}$ . The resultant states form a multiplet of levels having a "center of mass" at the energy of the one phonon excited level in the even-even core nucleus (25). Bouten and Van Leuven (8) calculated the level schemes for all of the odd mass copper isotopes. The results of their calculations for  $\text{Cu}^{63}$  were verified qualitatively by Blair (2).

Following Bouten and Van Leuven the extended version of the model is called the Unified Model. Allowance is made for more

complicated configurations of the excited levels than is permitted for the weak coupling model. In particular, single particle states, other than the lowest lying orbital, are allowed to contribute admixtures to a given state. Further, the effect of the two phonon states of the core coupled to a single particle states are allowed to contribute also.

A given level may be a mixture of several single particle states coupled to various vibrational core states. This last prediction was verified for  $\text{Cu}^{63}$  by the results of Blair (2) who excited single particle states by the  $\text{Ni}^{62}(\text{He}^3, d)\text{Cu}^{63}$  reaction. The spectroscopic factors he determined supported the conclusions of Bouten and Van Leuven as to the relative amounts of admixtures. In the weak coupling form of the unified model, the multiplet of states should have zero cross sections for stripping reactions which can only excite single particle states. The appearance of finite cross sections for the lowest excited states is evidence for the breakdown of the simple model.

The generalization of equation 4-17 requires that N, R, and j take on more than one value, i. e.

$$\Phi_o^I = \sum_{jNR} a(j, NR, I) \sum_m C(jRI \ 0 \ M-m) |NRR_\mu > |jm> \quad (4-18)$$

Using these wave functions, the interaction matrix elements are calculated and the resultant matrix diagonalized as a function of the

coupling parameter discussed below.

Because the interaction operator, equation 4-11, is linear in  $a_{\lambda\mu}$  it cannot contribute to the diagonal matrix elements. The diagonal matrix elements are given by  $E_c^R + E_{sp}^j$ , and these values are taken from experiment or introduced as parameters. The single particle energies are not well known. There are several studies which present values for  $E_{sp}^j$  in various regions of A (e. g. Kisslinger and Sorensen (24)), but the separation energies between single particle states are left as adjustable parameters for this calculation. Spins and energies of the core states were taken from the experiment discussed in the Scattering Experiment Chapter.

Off diagonal elements involve only  $H_{int}$  and so:

$$E_{int}^{II'} = \langle j' N' R', I' M' | k(r) \sum_{\lambda\mu} a_{\lambda\mu} Y_{\lambda}^{\mu*}(\theta, \phi) | j, NR, IM \rangle \quad (4-19)$$

Here, only a single particle outside the core is considered, so in equation 4-9 the sum over all nuclear particles is reduced to one term. Also, only quadrupole ( $\lambda = 2$ ) excitations are considered since higher order vibrational modes occur at energies of about 3 mev. which is higher than the energies which are concerned with here. (When the positive parity levels are considered, the octupole ( $\lambda = 3$ ) vibrational state will be considered.) In terms of the boson creation and destruction operators, the matrix elements become:

$$E_{\text{int}}^{\text{II}'} = \left(\frac{\hbar\omega}{2C}\right)^{1/2} \langle j', N'R', I'M' | k(r) \sum_{\mu} (-1)^{\mu} [b_{\mu} + (-1)^{\mu} b_{-\mu}^+] Y_2^{-\mu}(\theta, \phi) | j, NR, IM \rangle \quad (4-20)$$

$b_2$  and  $Y_2$  are both irreducible tensor operators of rank two, so using equation 6.22 from Rose (37) equation 4-20 becomes

$$E_{\text{int}}^{\text{II}'} = \left(\frac{\hbar\omega}{2C}\right)^{1/2} \langle n'\ell' | k(r) | n\ell \rangle \delta_{MM'} \delta_{II'} (-1)^{j' + R - I} \langle \frac{1}{2} \ell' j' || Y_2 || \frac{1}{2} \ell j \rangle [(2j' + 1)(2j + 1)]^{1/2} \langle N'R' || b_2 + b_2^+ || NR \rangle W(j'R'jR; I2) \quad (4-21)$$

The reduced matrix elements of  $Y_2$  are evaluated specifically (de-Shalit and Talmi, (13));

$$\begin{aligned} \langle \frac{1}{2} \ell' j' || Y_2 || \frac{1}{2} \ell j \rangle &= (-1)^{j' - 1/2} \left[ \frac{2j + 1}{4\pi} \right]^{1/2} C(j' j 2; \frac{1}{2} - \frac{1}{2} 0) \\ &\quad (\ell + \ell' \text{ even}) \\ &= 0 \quad (\ell + \ell' \text{ odd}) \end{aligned} \quad (4-22)$$

Reduced matrix elements for  $b_2$  are tabulated by Choudhury (12) and  $W(j'R'jR; I2)$  is a Racah coefficient. Some selection rules are immediately apparent, i. e.  $I = I'$ ,  $M = M'$ ,  $\ell + \ell'$  is even, and  $\Delta N = +1$ .

The level energies of  $\text{Zn}^{70}$ , the core nucleus, were chosen from those determined in the  $\text{Zn}^{70}(\alpha, \alpha')$  experiment of the next chapter. The first excited state is a one phonon  $2^+$  state at 875 kev.

The two phonon  $2^+$  level is at 1750 kev. These are the only levels considered. (The two phonon levels at 1960 kev ( $0^+$ ) and 2360 kev ( $4^+$ ) were introduced for one calculation, but it was determined that they have a negligible effect on the low lying levels. Also, from the  $\text{Zn}^{70}(\alpha, \alpha')$  experiment these levels are excited only weakly and are not expected to be important.)

For calculation of negative parity states, the single particle orbitals considered were the  $2p_{3/2}^-$ ,  $1f_{5/2}^-$ , and  $2p_{1/2}^-$ . The next higher lying single particle level is the  $1g_{9/2}^+$ , which will be included in the calculation of positive parity states. Values for

$$E_1 = E(1f_{5/2}^-) - E(2p_{3/2}^-)$$

and

$$E_2 = E(2p_{1/2}^-) - E(2p_{3/2}^-)$$

are suggested by Bouten and Van Leuven (8) at 1.36 and 1.81 Mev respectively, for  $\text{Cu}^{63}$ . Kisslinger and Sorensen (24) suggest values of  $E_1 = 0.95$  Mev and  $E_2 = 2.25$  Mev for  $Z = 30$  and  $N = 34$  nuclei. Using these values as a guide, small changes were made in  $E_1$  and  $E_2$  until a best fit to the experimental decay scheme of  $\text{Ga}^{71}$  was obtained.

Radial wave functions were chosen in two forms: first, they were the radial wave functions of a harmonic oscillator potential, and second, the wave functions generated by a Saxon-Woods potential.

Oscillator wave functions allowed an analytic solution for the radial integral. They took the following form;

$$\begin{aligned} R_{1f}(r) &= \sqrt{\frac{2p^{9/2}}{\Gamma(9/2)}} e^{-\frac{pr^2}{2}} r^3 \\ R_{2p}(r) &= \sqrt{\frac{2p^{5/2}}{\Gamma(7/2)}} e^{-\frac{pr^2}{2}} r(5/2 - pr^2) \end{aligned} \quad (4-23)$$

The parameter  $p$  is the oscillator constant and was determined in the following manner. From Hofstadter (21), the root-mean-square radius of the nucleus determined by electron scattering is calculated from:

$$r_{\text{RMS}}^2 = \int r^2 \rho(r) 4\pi r^2 dr \quad (4-24)$$

where  $\rho(r)$  is the charge distribution in the nucleus. If a uniform distribution of radius  $R_o$  is considered, then the relationship

$$r_{\text{RMS}}^2 = \frac{3}{5} R_o^2$$

is obtained. From de-Sahlit and Talmi (13) it is shown that the overlap integral,

$$I = \int R_{1\ell'}^*(r) R_{1\ell}(r) r^2 dr = \left[ \frac{\sqrt{pp'}}{1/2(p + p')} \right]^{3/2} \quad (4-25)$$

is insensitive to variations in  $\ell$  since the major contribution of  $R_{n\ell}$  is near the origin. A reasonable approximation to  $p$  can then be determined by calculating;



$$\langle r^2 \rangle = \int_0^\infty R_{1f}(r) r^2 R_{1f}(r) dr = \frac{3}{5} (r_o A^{1/3})^2 \quad (4-26)$$

where  $r_o = 1.23 f$  and  $A = 70$ . The result for  $p$  is  $0.89 f^{-2}$ .

Wave functions for the Saxon-Woods potential were found from a numerical solution of the Schrodinger equation;

$$\left[ \frac{d^2}{dr^2} - \frac{\ell(\ell+1)}{r^2} + V(r) \right] R_{n\ell}(r) = 0 \quad (4-27)$$

where

$$V(r) = \frac{V_o}{1 + \exp\left[\frac{r - R_o}{a}\right]} ; \quad R_o = 1.3 A^{1/3} f, \quad a = 0.67 f \quad (4-28)$$

The problem was programed for the CDC-3300 computer of the Oregon State University Computer Center. A listing of the program is shown in Appendix B2<sup>3</sup>. In this program, called BSWF, the binding energy of a given level is inserted along with values for the mean radius  $R_o$  and surface diffuseness parameter  $a$ . The binding energy of the ground state is just the binding energy of a proton to  $Zn^{70}$ , which is 7.8 Mev. Wave functions for the next two single particle levels were calculated using  $E_1 = 1.0$  and  $E_2 = 2.0$  Mev. The parameters were taken from proton scattering data (34), except for  $V_o$  which was determined by the computer program.

---

<sup>3</sup>Appreciation is extended to Mr. Frank Schmittroth for use of this program.

The interaction  $k(r)$  was also chosen in two possible forms.

First, a Gaussian shape was considered:

$$k(r) = \frac{V_o}{2\sigma} \exp\left[-\left(\frac{r - R_o}{2\sigma}\right)^2\right] \quad (4-29)$$

where  $R_o = 1.25A^{1/3}f$ ,  $\sigma = 0.55f$ , and  $V_o$  is unknown. These parameters were taken from Hofstadter (21). This function,  $k(r)$ , is symmetric about the mean radius  $R_o$ . The second choice for the interaction was suggested by the definition in equation 4-11, namely,  $k(r) = R_o dV/dr$ , where  $V(r)$  has the Saxon-Woods form, equation 4-28. Values for this function were calculated and inserted in the radial integrals. The parameters were the same as for the wave function calculation.

For the Gaussian interaction with oscillator wave functions, integrals were calculated by hand. For the other cases, however, a computer program was written to perform the integration numerically. This program is listed in Appendix B1.

The matrix resulting from calculating the matrix elements of  $H$ , equation 4-8, was diagonalized using a program<sup>4</sup> on the CDC-3300 computer. This program calculates eigenvectors along with eigenvalues. Off diagonal elements involve an adjustable coupling parameter  $\xi$ , which is given explicitly by:

---

<sup>4</sup>The program is a modification of one obtained from the Quantum Chemistry Program Exchange, Indiana University.

$$\xi = V_o \left( \frac{\hbar\omega}{2C_2} \right)^{1/2} \quad (4-30)$$

Note that the deformation parameter  $\beta_\lambda$  in the collective model is given by:

$$\beta_\lambda = \sqrt{2\lambda + 1} \left( \frac{\hbar\omega_\lambda}{2C_\lambda} \right)^{1/2} \quad (4-31)$$

Thus, if  $\beta_2$  was known,  $V_o$  could be calculated.

In summary, three forms of calculations were made and compared. Type I had a Gaussian form for the interaction and Harmonic Oscillator wave functions. Type II used a Gaussian interaction with Saxon-Woods wave functions. Type III used a derivative Saxon-Woods interaction and Saxon-Woods wave functions.

Figure 24 shows the results from Type I. The single particle spacings,  $E_1$  and  $E_2$ , were varied over rather wide ranges so this is only a typical result. The Type II calculation is shown in Figure 25 and Type III in Figure 26.

For Type I there was no set of values for  $E_1$ ,  $E_2$ , and  $\xi$ , which came very close to giving results in agreement with Figure 20, the experimental decay scheme. However, Type II, and particularly, Type III calculations gave very good agreement for the first three excited levels. For Type III this occurs for  $E_1 = 0.70$  Mev and  $E_2 = 1.80$  Mev. The position of the  $5/2^-$  level is very sensitive to the choice of  $E_1$ , while the  $1/2^-$  state is comparatively insensitive to

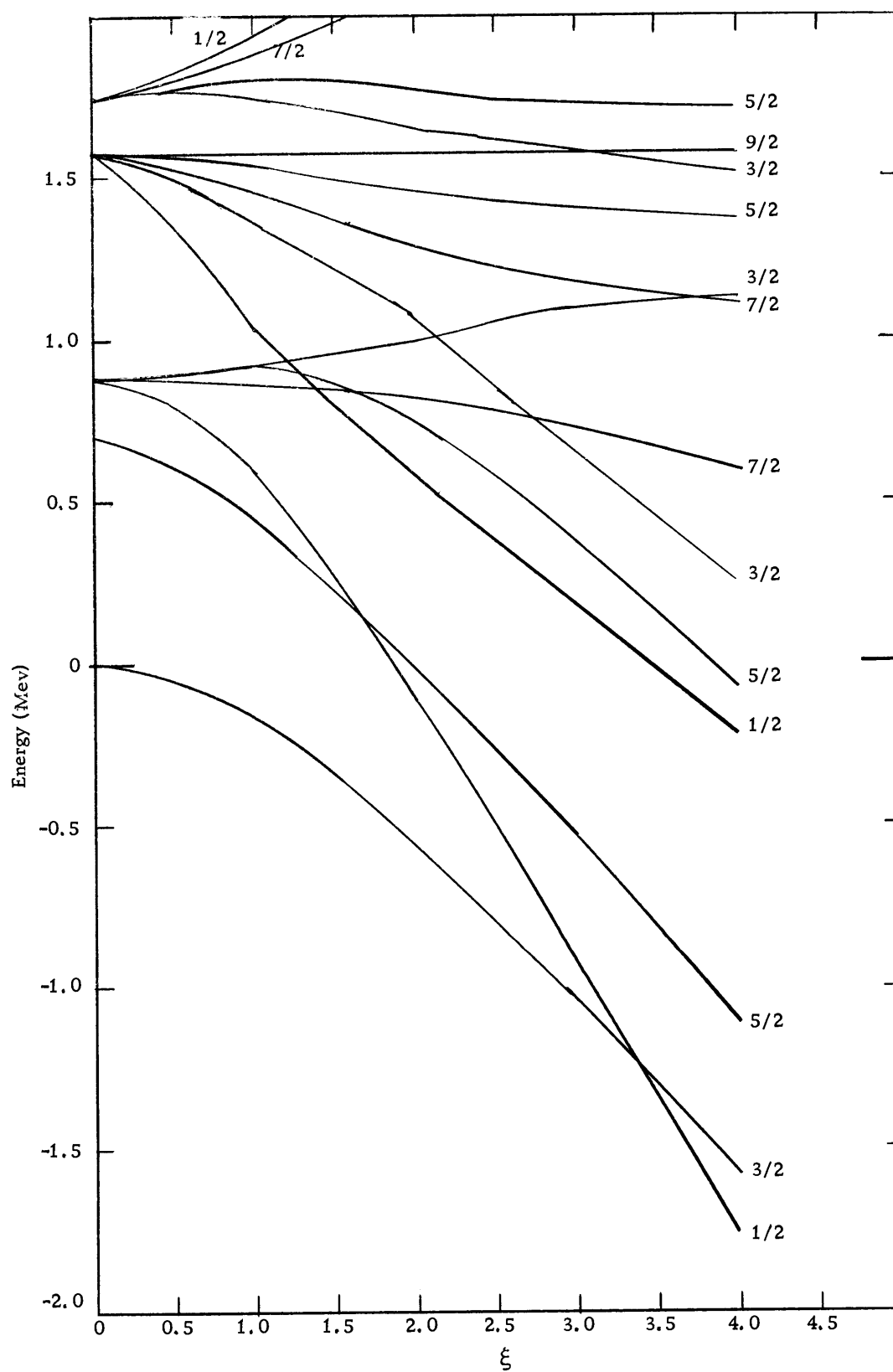


Figure 24. Type I calculation.  $E_1 = 0.70 \text{ MeV}$ ,  $E_2 = 2.00 \text{ MeV}$ .

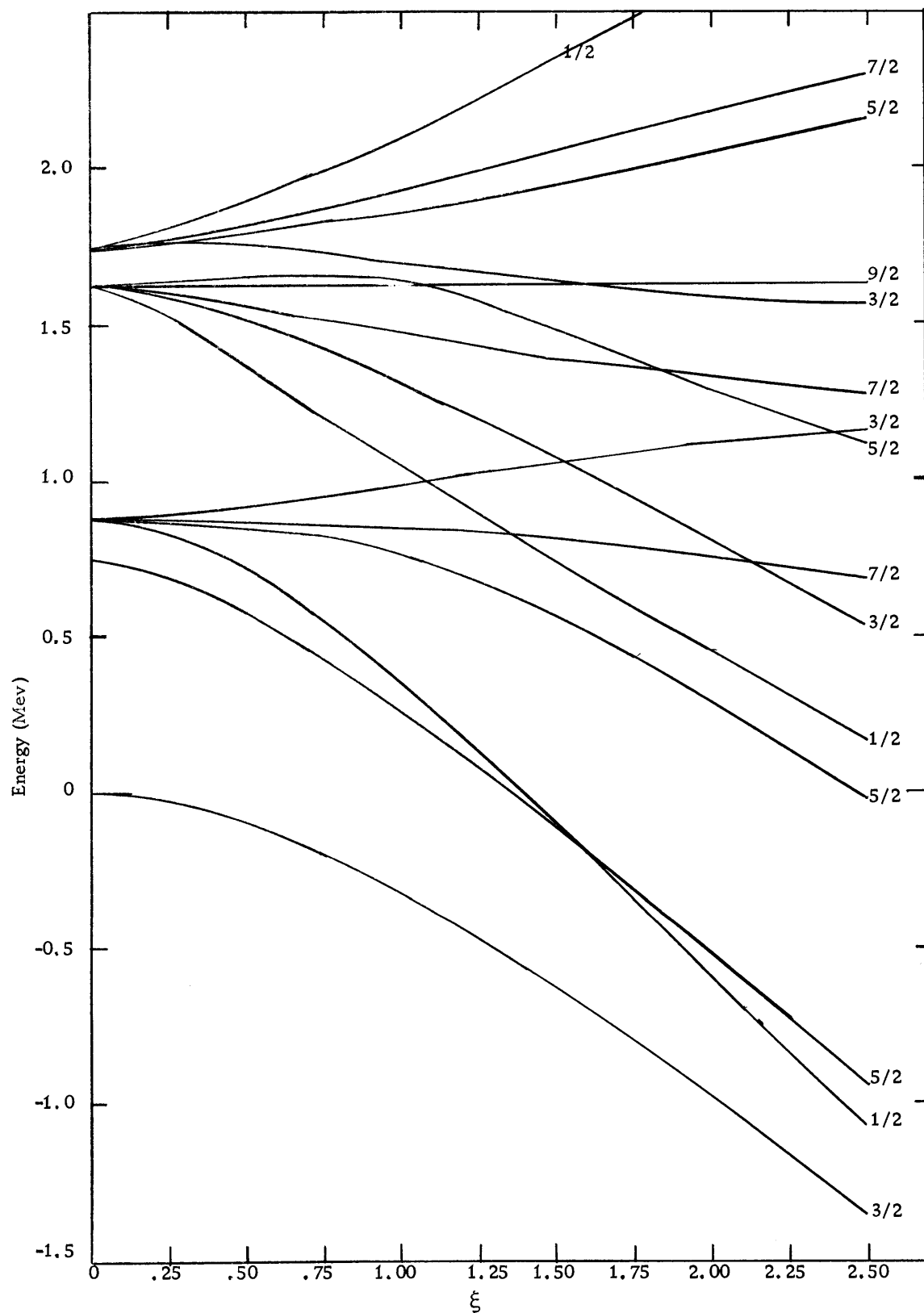


Figure 25. Type II calculation.  $E_1 = 0.75$  Mev,  $E_2 = 2.00$  Mev.

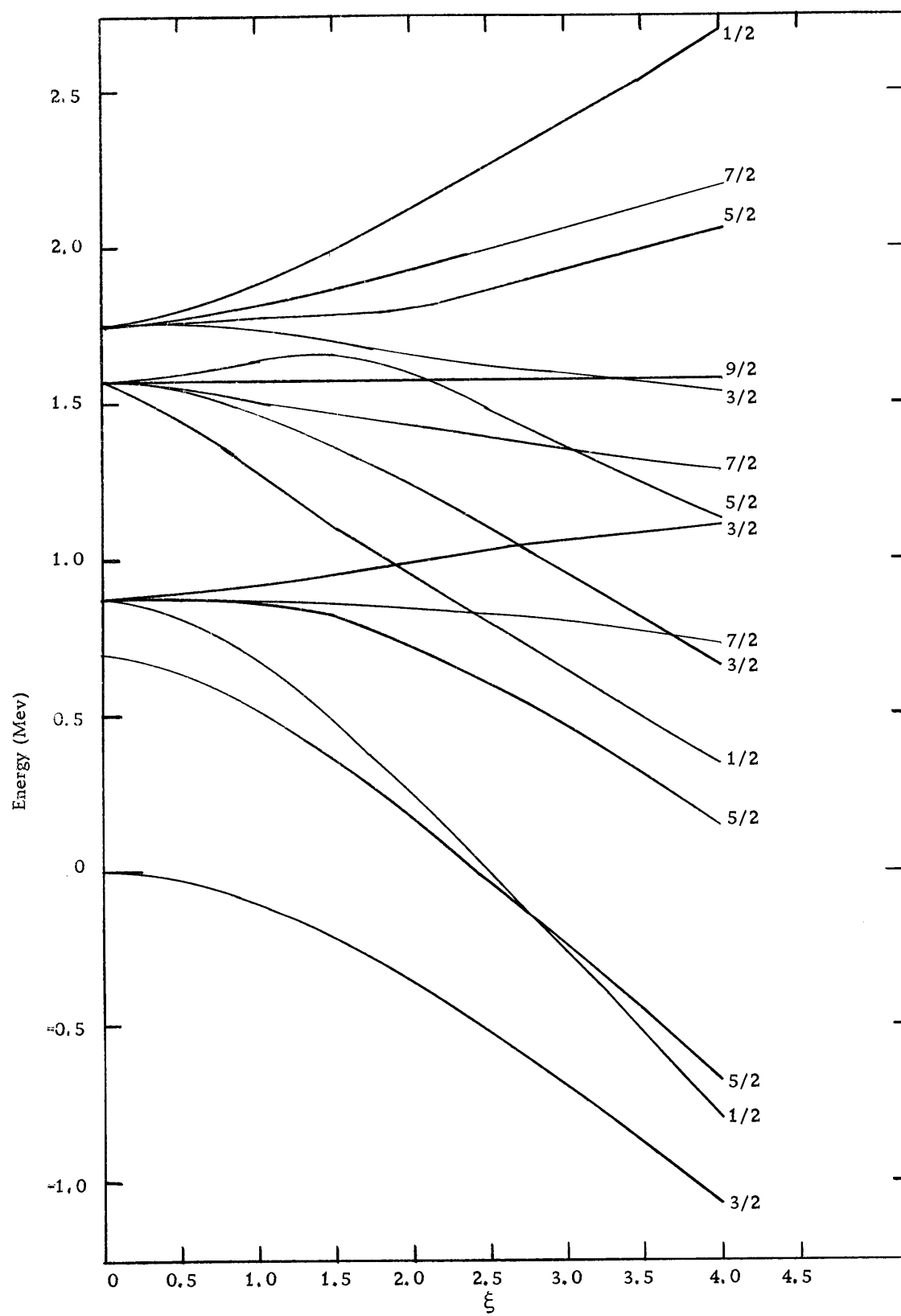


Figure 26. Type III calculation.  $E_1 = 0.70 \text{ Mev}$ ,  $E_2 = 1.80 \text{ Mev}$ .

the variation of  $E_2$ .

Figure 27 shows a comparison of the calculation with experiment. The best fit occurs for a value of  $\xi$  equal to 2.50. Table 3 lists the coefficients for the corresponding eigenvector, showing the rather complete mixing of the various states, particularly, the admixtures of single particle states.

Table 3. Eigenvector coefficients  $a(j, NR, I)$  for low lying states in  $\text{Ga}^{71}$ .

Basis State	3/2(g. s. )	5/2(488)	1/2(512)	5/2(1108)
<u>Negative Parity States</u>				
$ 3/2, 00, 3/2\rangle$	0.863	-	-	-
$ 3/2, 12, 1/2\rangle$	-	-	-0.745	-
$ 3/2, 12, 3/2\rangle$	-0.410	-	-	-
$ 3/2, 12, 5/2\rangle$	-	0.415	-	-0.781
$ 5/2, 00, 5/2\rangle$	-	-0.771	-	-0.305
$ 1/2, 00, 1/2\rangle$	-	-	-0.531	-
$ 3/2, 22, 1/2\rangle$	-	-	0.267	-
$ 3/2, 22, 3/2\rangle$	0.029	-	-	-
$ 3/2, 22, 5/2\rangle$	-	0.202	-	-0.256
$ 5/2, 12, 1/2\rangle$	-	-	0.302	-
$ 5/2, 12, 3/2\rangle$	0.212	-	-	-
$ 5/2, 12, 5/2\rangle$	-	-0.389	-	-0.423
$ 1/2, 12, 3/2\rangle$	-0.202	-	-	-
$ 1/2, 12, 5/2\rangle$	-	0.203	-	0.207
<u>Positive Parity States</u>				
	<u>9/2(1495)</u>			
$ 9/2, 00, 9/2\rangle$	0.791			
$ 3/2, 13, 9/2\rangle$	-0.604			
$ 5/2, 13, 9/2\rangle$	-0.090			

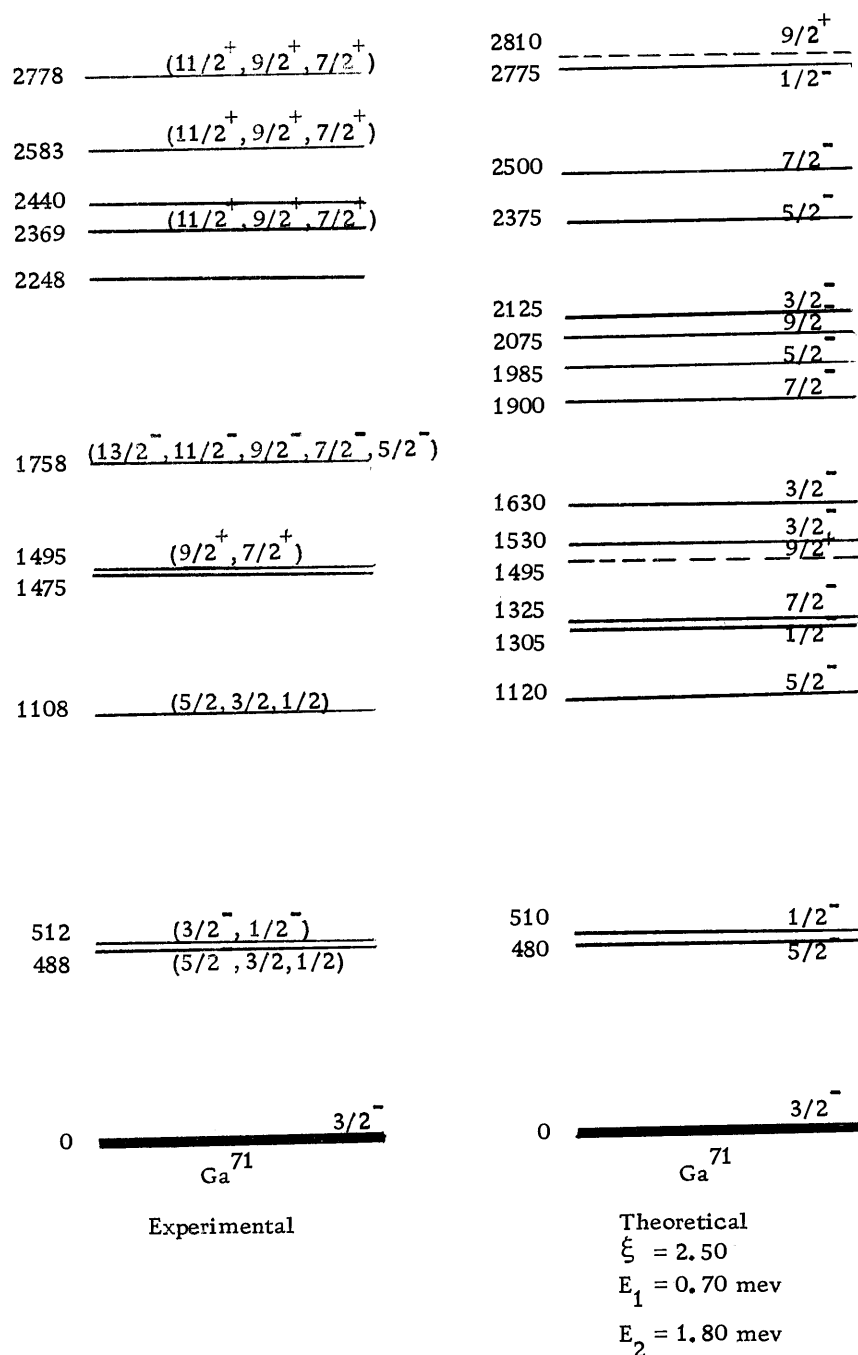


Figure 27. Comparison of experimental and theoretical level schemes for  $\text{Ga}^{71}$ .



Positive parity states were also considered since from the decay scheme of Figure 20, there are apparently several positive parity levels in  $\text{Ga}^{71}$ . The  $1g_{9/2}^+$  single particle state is coupled to the positive parity core states. Also, the couplings of  $2p_{3/2}^-$  and  $1f_{5/2}^-$  single particle states to the  $3^-$  octupole phonon state of the core are considered. These couplings are reasonable since the energy of the  $1g_{9/2}$  state is expected to be about three Mev (24), and the  $3^-$  state is at 2.81 Mev. Considering the states  $|9/2, 00, 9/2\rangle$ ,  $|3/2, 13, 9/2\rangle$ , and  $|5/2, 13, 9/2\rangle$  the Hamiltonian was diagonalized. The perturbation term is given by equation 4-19 with  $\lambda = 3$ . Note that  $\eta$ , given by

$$\eta = \left( \frac{\hbar\omega_3}{2C_3} \right)^{1/2} V_o = \frac{\beta_3 V_o}{\sqrt{7}} \quad (4-32)$$

is not the same as  $\xi$ , since  $\beta_2$  and  $\beta_3$  are different, in general. The value of  $E_3 = E(1g_{9/2}) - E(2p_{3/2})$  was taken as a parameter along with  $\eta$ . The  $3 \times 3$  matrix was diagonalized as a function of variations in these two parameters. The results are shown in Figure 28 for the Type III calculation. The eigenvector for the fit of the 1495 kev level is given in Table 3. For  $E_3$ , Kisslinger and Sorensen (24) suggest a value of 3.0 Mev for the  $Z = 30$ ,  $N = 34$  nuclei. However, the calculations of negative parity levels indicate that the best fit to experiment is obtained if the Kisslinger and Sorensen values are

reduced by 25%, hence in Figure 28, curves for  $E_3$  equal to 2.3 and 3.0 Mev are shown. Only the 1495 level is fitted accurately for  $\eta = 1.25$ , although the 2778 is fairly close to the 2810 kev degenerate level. These positive parity levels are shown as dotted lines in the level scheme of Figure 27.

To check for mixtures of quadrupole and octupole excitations, the positive parity state  $|9/2, 12, 9/2\rangle$  was also considered. The matrix element involving this state involves the coupling parameters  $\xi$  and not  $\eta$ . The value  $\xi = 2.50$  was used. The results are shown in Figure 29 with  $E_3 = 2.3$  Mev. Only the 1495 level is described at a value of  $\eta = 0.75$ .

The effect of second order terms in the expansion of  $V(r-R)$  was considered. Since the second order matrix elements are small and contribute a correction to the first order terms of only a few percent, and have little effect on the eigenvalues, they were not included in the calculations. Also, the two phonon states  $O^+$  and  $4^+$  were not included in the calculations since a separate calculation indicated that their inclusion has a very small effect on the eigenvalues of interest.

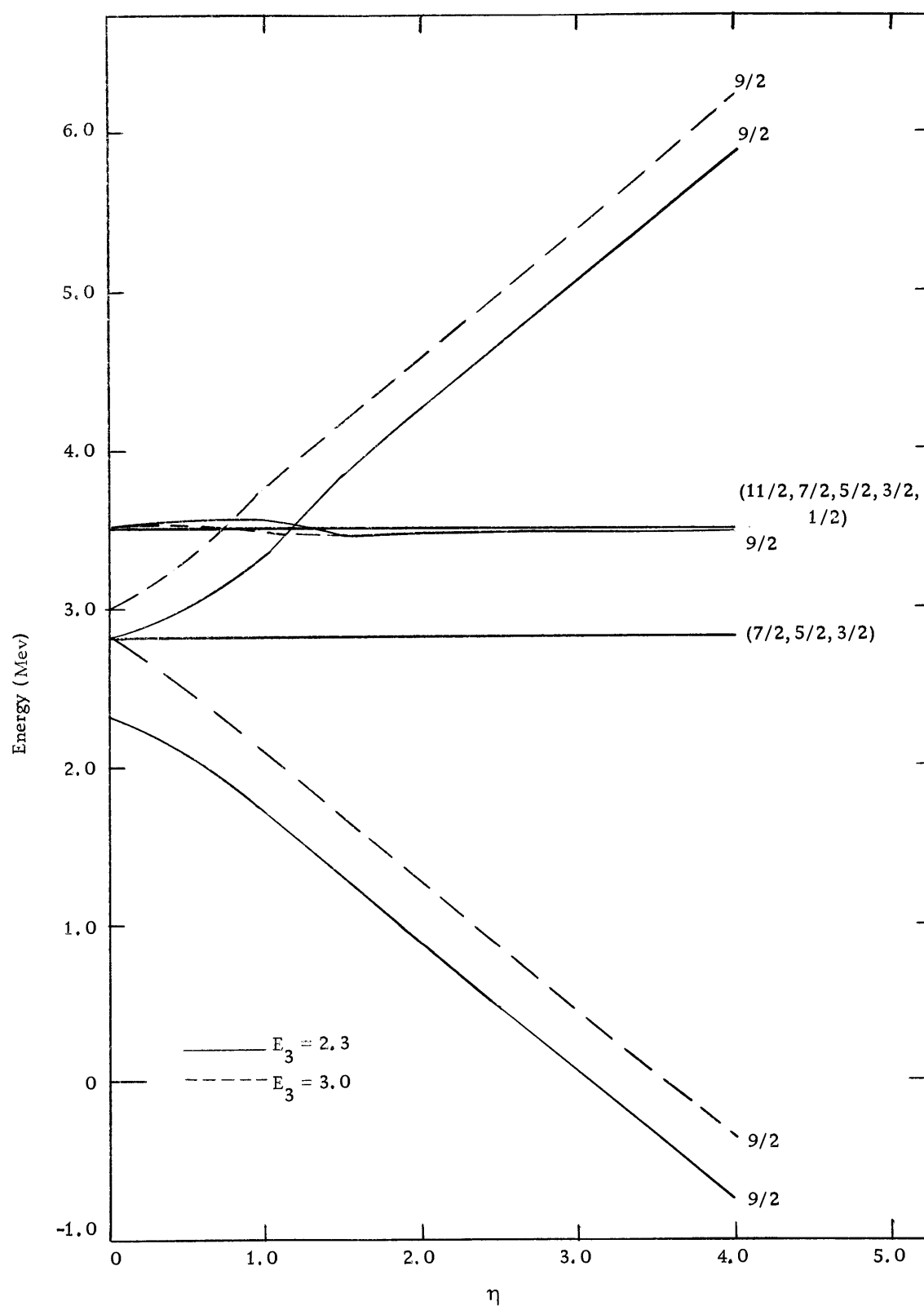


Figure 28. Positive parity levels - Type III calculation.

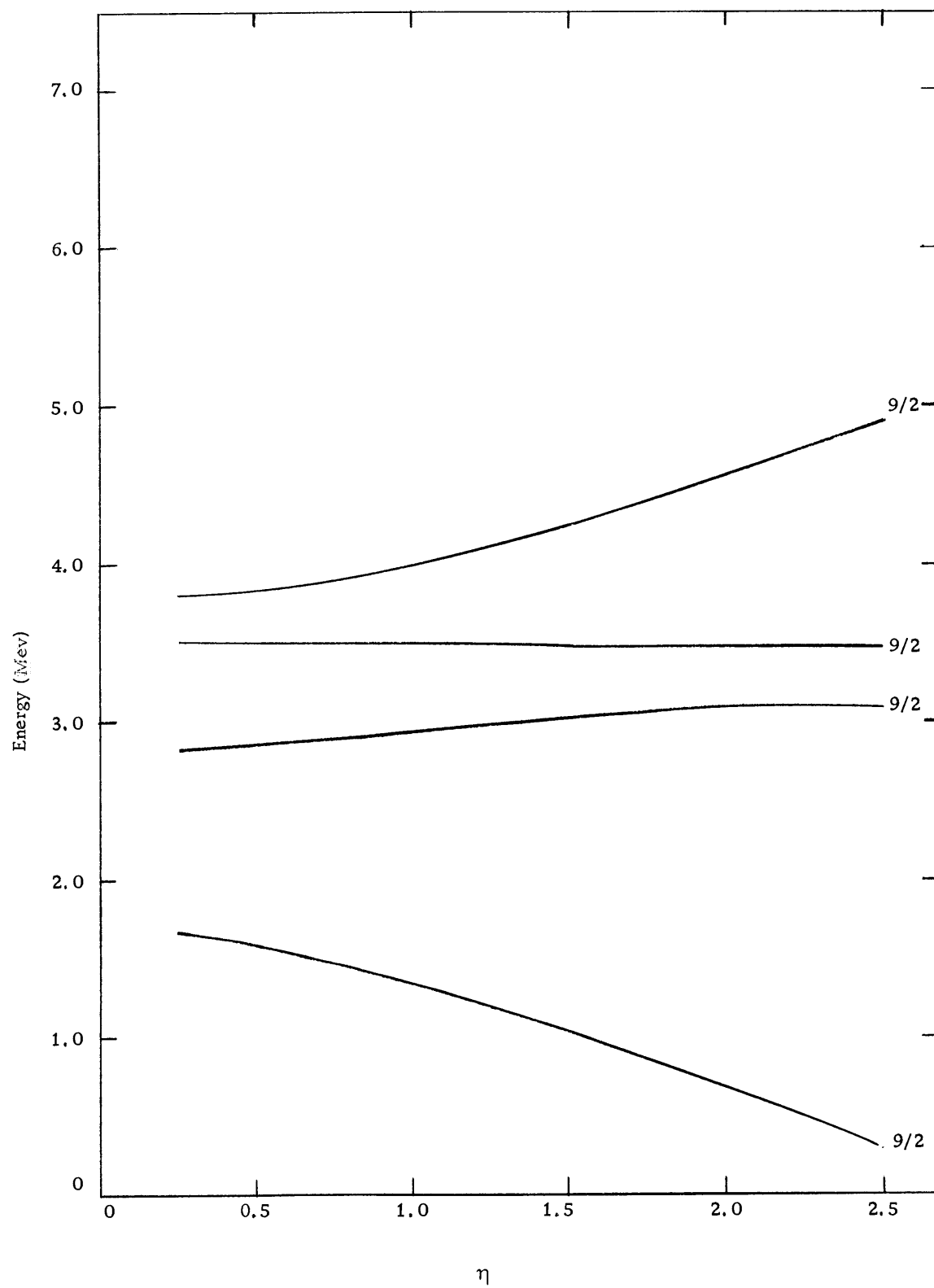


Figure 29. Positive parity levels including quadrupole excitation.

INELASTIC SCATTERING OF ALPHA PARTICLES FROM  $\text{Zn}^{70}$ Apparatus and Procedure

The experiment was designed for the 60" cyclotron of the University of Washington. The external beam from the accelerator passed through a shielding area into the target room and into the 60" scattering chamber. The beam was analyzed and focussed to present 42.5 Mev alpha particles on the target, at currents, as measured in a Faraday cup, up to 0.1 microamperes. The beam was collimated by a slit system consisting of the following: a beam defining slit, an anti-scattering slit, a beam defining slit, and a clean-up slit. The latter slit was to prevent alpha particles scattered by the slit edges from reaching the detector. All slit dimensions were  $1/16'' \times 1/4''$ . The slit system was checked for its scattering properties by running the beam at full current with no target in position and monitoring the detector output as a function of angle. A negligible count due to scattered particles was found.

The scattering chamber provided for remote operation of the target changer and the detector position. The target changer itself permitted the mounting of eight separate target holders on a rotating circular wheel and allowed very accurate repositioning of the targets. Detectors were mounted on arms which rotated about the target axis.

Their angular positions could be set to within  $\pm 0.01^\circ$ . The detectors were positioned nine inches from the center of the target and shielded with lead and paraffin to prevent detection of scattered gamma rays and neutrons from the collimator system. A massive lead collar surrounded the slit system as further shielding against the large gamma ray background.

The detectors were lithium drifted silicon surface barrier detectors, with depletion layers of two millimeters and surface areas of  $80 \text{ mm}^2$ . This thickness is about two times greater than is necessary for stopping 40 Mev alpha particles. The detectors were mounted on separate rotating arms, so that, together with the target, a horizontal plane was defined. One detector was placed in a fixed position at an angle of  $40^\circ$  with respect to the beam direction and was referred to as the monitor counter. It remained fixed in position for the duration of the experiment. A  $1/8$ " thick brass collimator with a slit of dimensions of  $1/8$ " x  $3/8$ " was placed over the face of each detector. The brass was thick enough to stop all particles which did not fall on the slit.

Electronic connections were made with feedthrough connectors in the scattering chamber walls. These outlets in turn were connected to a patch panel in the target room which was matched to a remote panel in the counting room located next to the accelerator control room. Figure 30 is a block diagram of the electronics.

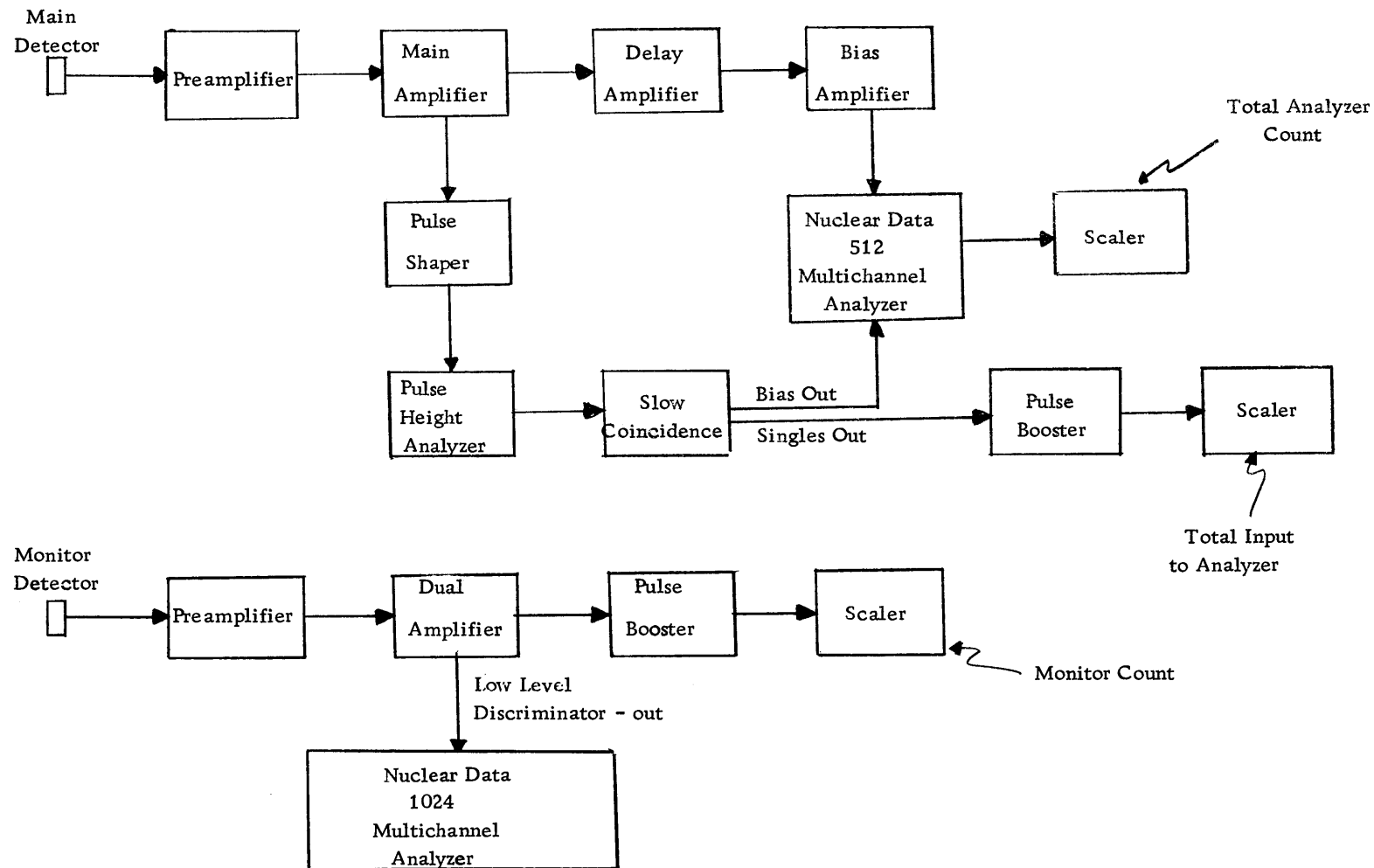


Figure 30. Block diagram of electronics for inelastic scattering experiment.

The Ortec Bias Control Unit, for biasing the detectors, contains a detector current meter for monitoring the reverse (leakage) current. This is a useful feature for watching the detector performance since one sign of a faulty detector is the appearance of large leakage currents. The monitor detector, when initially tested, exhibited a rather large leakage current. The current decreased a great deal as the chamber pressure dropped, until the monitor became comparable in performance with the main detector. The leakage current was monitored carefully throughout the experiment, but no sign of malfunction of either detector was indicated over the three day duration of the experiment. Operation of the detectors was checked by inserting small alpha particle sources near the collimator slits and observing the detector output in the counting room. These sources were removed before the final pump down of the scattering chamber began.

The electronic analysis was set to scan the entire scattered alpha particle spectrum. A low level discriminator was used to reject low energy noise pulses in order to reduce the analyzer dead time. The monitor detector was connected to a separate system which permitted monitoring of the count as well as a scanning of the alpha particle spectrum. A discriminator was added so only particles in the elastic peak were counted; this number was then used for normalizing the cross section data. By monitoring the total



coincidence counts and comparing this number with the total analyzer count, that is, the actual number of pulses analyzed, a measure of the dead time of the multichannel analyzer could be found. This number indicated the dead time to be on the order of 1% for all runs.

The target material was obtained from Oak Ridge as a separated isotope in the form of ZnO powder with the following impurity specifications:  $\text{Zn}^{70}$  (85.9%),  $\text{Zn}^{68}$  (4.46%),  $\text{Zn}^{67}$  (0.81%),  $\text{Zn}^{66}$  (3.71%), and  $\text{Zn}^{64}$  (5.08%). The separated isotope of  $\text{Zn}^{68}$  (99.3%) was also obtained to be used to provide a check on the contributions of the impurities to the spectrum of scattered particles.

Target foils were produced by the following procedure<sup>5</sup>: The ZnO powder was dissolved in dilute  $\text{H}_2\text{SO}_4$  and the solution was then neutralized with NaOH. The solution was placed in a small electro-deposition chamber; a small amount of detergent was added to the solution in order to prevent bubbles from forming on the electrodes which would greatly reduce the plating efficiency and quality. A stirring motor also helped to prevent this effect and to keep the ion concentration uniform.  $\text{Zn}^{70}$  was plated out of solution onto a stainless steel foil at a current of about 20 milliamperes. The plated surface was washed with water and the apparatus disassembled. By flexing the foil, the plated metal was dislodged. The metal was then

---

<sup>5</sup>Thanks are expressed to Mrs. Joanne Sauer of the University of Washington Cyclotron Laboratory for preparing the target foils.

placed in a small diameter, thin walled, tantalum cylinder, whose ends were then crimped closed. A pin hole was punched into the cylinder wall which had become slightly flattened. The cylinder now became the boat for the Zn source in a vacuum evaporation system. The target backing material was a  $40 \text{ microgram/cm}^2$  thick carbon film. This film was placed with its surface facing the pinhole. The hole acts as a collimator for the zinc atoms being evaporated. This procedure was necessary because zinc has a low vapor pressure, making it difficult to control the direction of the evaporating atoms from the usual open boat geometry.

Target thicknesses were  $250 \text{ } \mu\text{g/cm}^2$  for  $\text{Zn}^{70}$  on  $40 \text{ } \mu\text{g/cm}^2$  of carbon, and  $500 \text{ } \mu\text{g/cm}^2$  for the selfsupporting  $\text{Zn}^{68}$  target foil. These are only estimates based on the measured mass of material deposited on the backing. Films were mounted on a small aluminum frame which in turn was mounted on the wheel of the target changer. Targets of polyethylene and mylar were also prepared for use as calibration sources. Actually, the oxygen contamination and the carbon backing were used as calibration sources, but the calibration lines were checked with a separate target.

With the target aligned so that its plane surface was perpendicular to the beam (i. e. a target angle of  $0^\circ$ ), the scattered alpha particle spectrum was measured for scattering from the  $\text{Zn}^{70}$  and the mylar targets. Data was taken in two degree intervals over the

range from 20 to 54° in the scattering angle. For comparative purposes, data was accumulated at several positions, for the scattered spectrum from  $\text{Zn}^{68}$ . At a scattering angle of 44°, the target angle was changed to 25° to compensate for the increasing path length of the scattered alpha particles in the target.

The data, accumulated on the Nuclear Data 512 Channel Analyzer, was punched on paper tape. The tape in turn was read out onto a typewriter. This procedure was used to save beam time because of the slow speed of the typewriter. The monitor count and each of the scaler outputs were recorded.

To assure that the target was not deteriorating due to the beam bombardment, the ratio of the beam count to the monitor count was calculated after each run. Values of this ratio fluctuated slightly, but no upward trend was seen, which would have indicated a loss of target material.

### Data Analysis and Results

Using the usual kinematical relationships for the inelastic scattering of a mass four particle from mass 12 and 16 particles and using the excitation energies for states in  $\text{C}^{12}$  and  $\text{O}^{16}$ , respectively, (32) a computer program calculated the energies of the scattered particles as a function of angle. From these results, peaks in the spectra due to oxygen and carbon were identified and used to

construct a calibration curve (which turned out to be very linear).

This procedure was carried out for each angle. Figure 31, a typical scattered particle spectrum at  $34^\circ$ , indicates the impurity lines used in the calibration. The scale factor for each run was used to calculate energies of all the peaks appearing in the spectrum. Averages for the energies are listed in Table 4. Errors listed are the standard errors compounded with the uncertainties in the estimation of the peak position.

Table 4. Levels energies in  $\text{Zn}^{70}$ .

Energy (kev)	Spin Parity ( $J^\pi$ )
0	$0^+$
$875 \pm 10$	$2^+$
$1750 \pm 10$	$2^+$
$1940 \pm 15$	$(0^+)$
$2360 \pm 20$	$(4^-)$
$2810 \pm 10$	$3^-$
$2990 \pm 20$	
$3295 \pm 15$	$3^-$
$3425 \pm 15$	
$3765 \pm 15$	
$4145 \pm 10$	
$4510 \pm 20$	
$4635 \pm 20$	
$4840 \pm 20$	
$5000 \pm 15$	
$5225 \pm 15$	
$5325 \pm 15$	
$5525 \pm 20$	
$5695 \pm 30$	
$5945 \pm 30$	

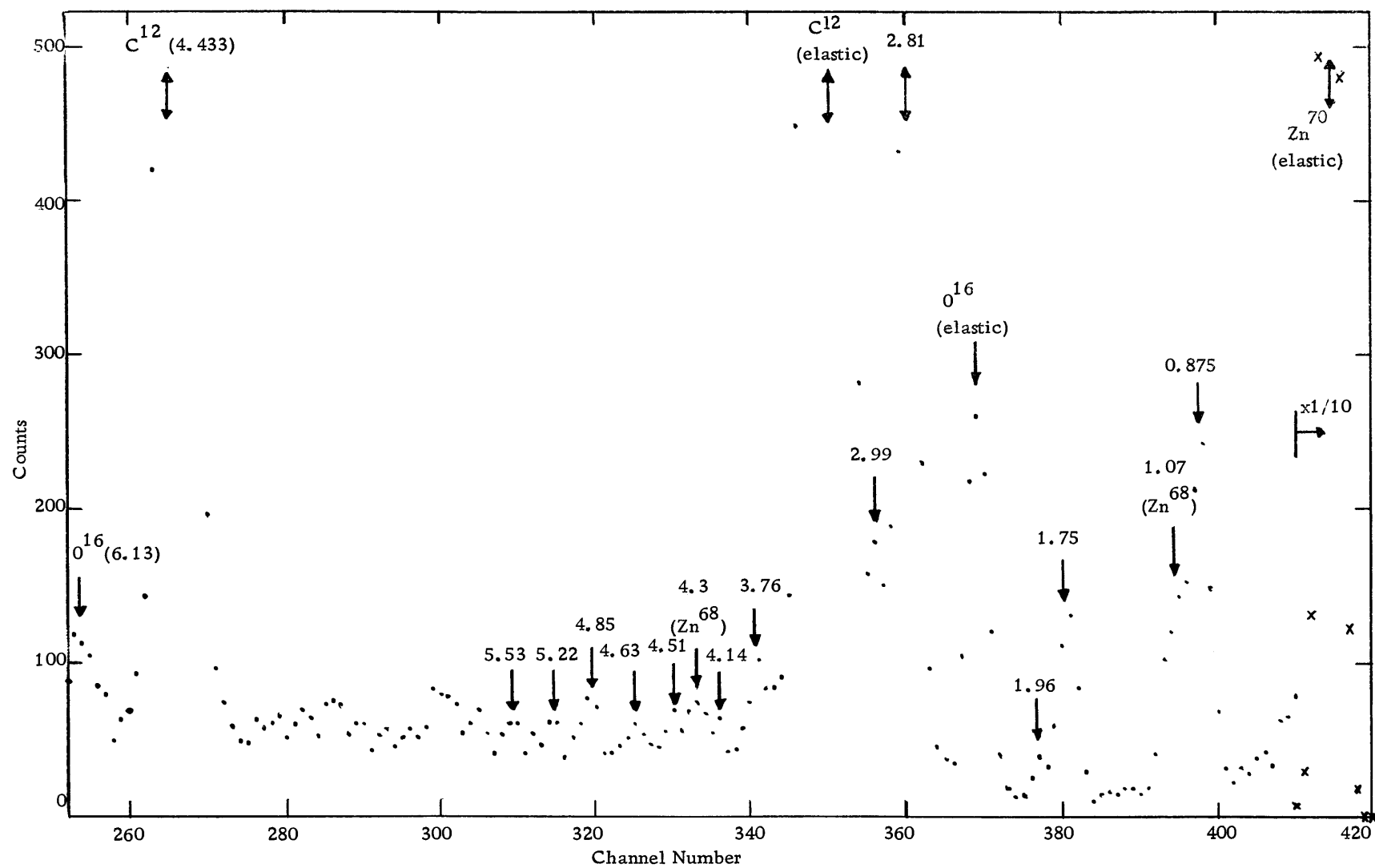


Figure 31. Typical scattered alpha particle spectrum -  $\theta = 34^\circ$ .

The only point of comparison with other investigations of  $\text{Zn}^{70}$ , is the energy and spin of the first excited state. Robinson, et al., (36) used Coulomb excitation to excite the first  $2^+$  level at  $887.1 \pm 0.7$  kev. From the experimental results here, the first level is found at  $875 \pm 10$  kev. The uncertainty is mostly due to the uncertainty in determining the position of the peak. The low counting rates and low (about 150 kev (FWHM)) energy resolution prevented making channel number assignments any closer than 0.1 to 0.2 channels. For determining the peak channel position, a symmetric shape for the peak was assumed. In actuality, the peaks are asymmetric; the slope is greater on the low energy side. Thus, the discrepancy between the two values for the energy of the first excited state may be due to this error in the determination of the peak position.

Energy loss by the particle in traversing the target has been taken into account. Before this effect was considered, the energy measurement gave 871 kev; the correction thus accounts for only about 0.5%. The procedure is explained using Figure 32. Assume, for the scattering by carbon, that on the average the alpha particles traverse one-half of the backing and are then scattered into the detector. The particles have a decreased energy due to the kinematical losses for exciting a  $\text{C}^{12}$  level. The scattered particle also loses energy in traversing the zinc. The oxygen calibration lines were found in a similar manner, except that on the average the particles

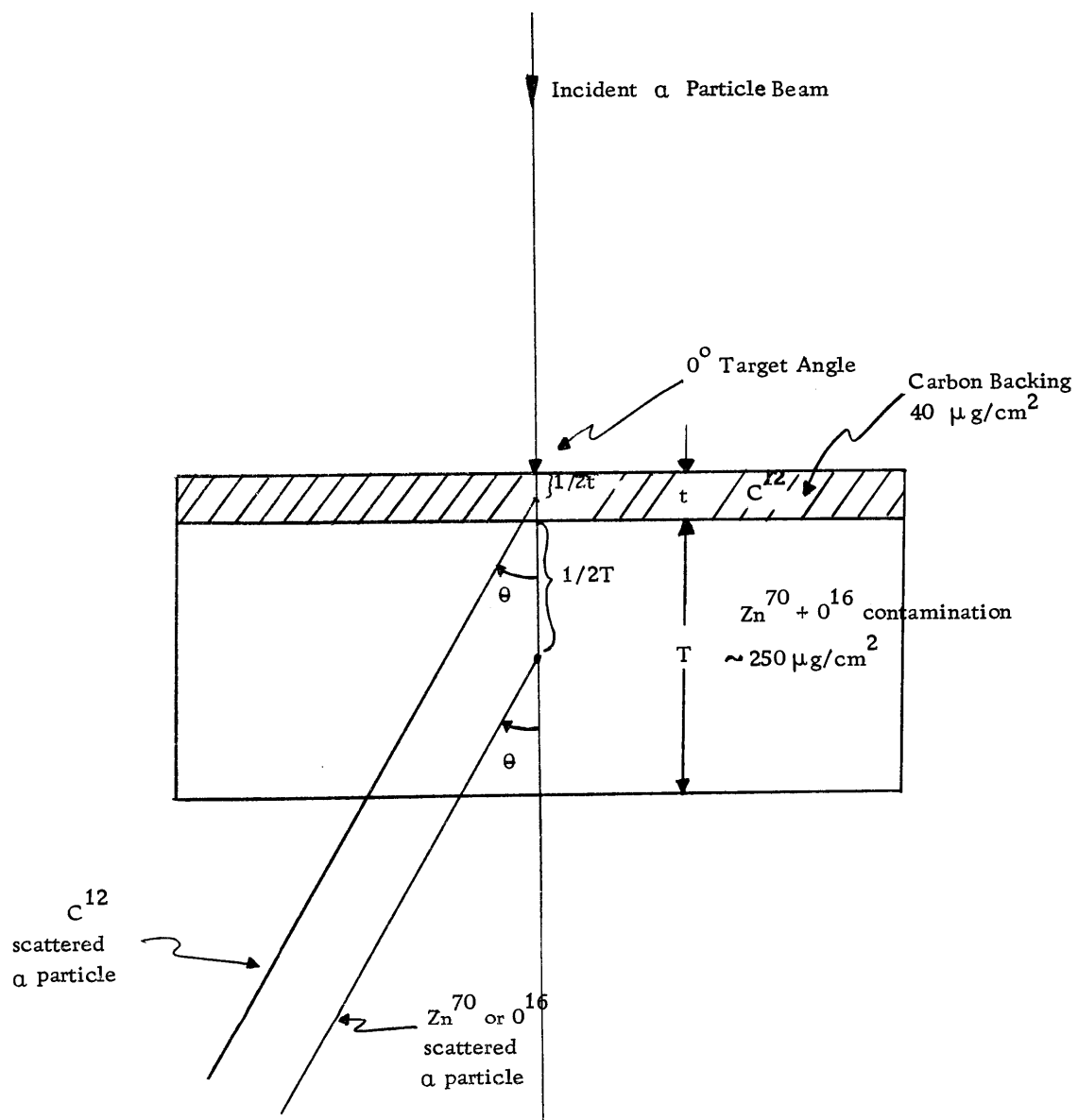


Figure 32. Geometry for computing energy losses in the target.

traverse the carbon backing and one-half of the zinc before being scattered. This procedure was used for the zinc scattered particles also.

For the purposes of experiment, the differential cross section  $\sigma(\theta)$  is defined by the following expression:

$$\Delta n = I N_s \sigma(\theta) \Delta \Omega_n \quad (5-1)$$

$\Delta n$  = the number of particles of a particular energy seen by the detector.

$I$  = the beam intensity in number of particles per square centimeter per second.

$N_s$  = the number of scatterers in the path of the beam.

$\sigma(\theta)$  = the cross section per unit solid angle for the scattering of a particle into the detector.

$\Delta \Omega_n$  = the solid angle subtended by the detector n.

In practice this equation is difficult to apply because of the difficulty in measuring  $N_s$ . This measurement requires a knowledge of the absolute thickness of the target, the density of the target material, the uniformity of the target, and the area of the beam where it strikes the target. (The beam may wander over the target, also.)

These are all uncertain quantities, so a relative cross section is frequently measured, in which  $N_s$  is never determined. The method used here to obtain absolute cross sections makes use of the results



of Broek (10) in the scattering of 43 Mev alpha particles from nickel and zinc isotopes. These results are presented as a universal curve in which the ratio of the absolute elastic cross section to the Rutherford cross section is plotted versus the center of mass scattering angle. The curve is shown in Figure 33 where the ratio of the cross sections is called  $B(\theta_c)$ .

The analysis of the data begins with the formation of the following ratio;

$$R(\theta_L) = \frac{\Delta n}{\Delta m} = \frac{IN_s \sigma(\theta_L) \Delta \Omega_n^L}{IN_s \sigma(40_L) \Delta \Omega_m^L} \quad (5-2)$$

where  $\Delta m$  is the number of counts recorded in the monitor counter. It is seen that the  $N_s$  factor drops out as does the intensity  $I$ . Now from the curve, Figure 33,

$$\sigma(\theta_c) = \sigma_{RUTH}(\theta_c) B(\theta_c) \quad (5-3)$$

Then,

$$\sigma(\theta_c) = R(\theta_c) K$$

where

$$K = \left[ \frac{\sigma(40) \Delta \Omega_m}{\Delta \Omega_n} \right] \quad (5-5)$$

and so

$$K = \frac{\sigma_{RUTH}(\theta_c) B(\theta_c)}{R(\theta_c)} \quad (5-6)$$

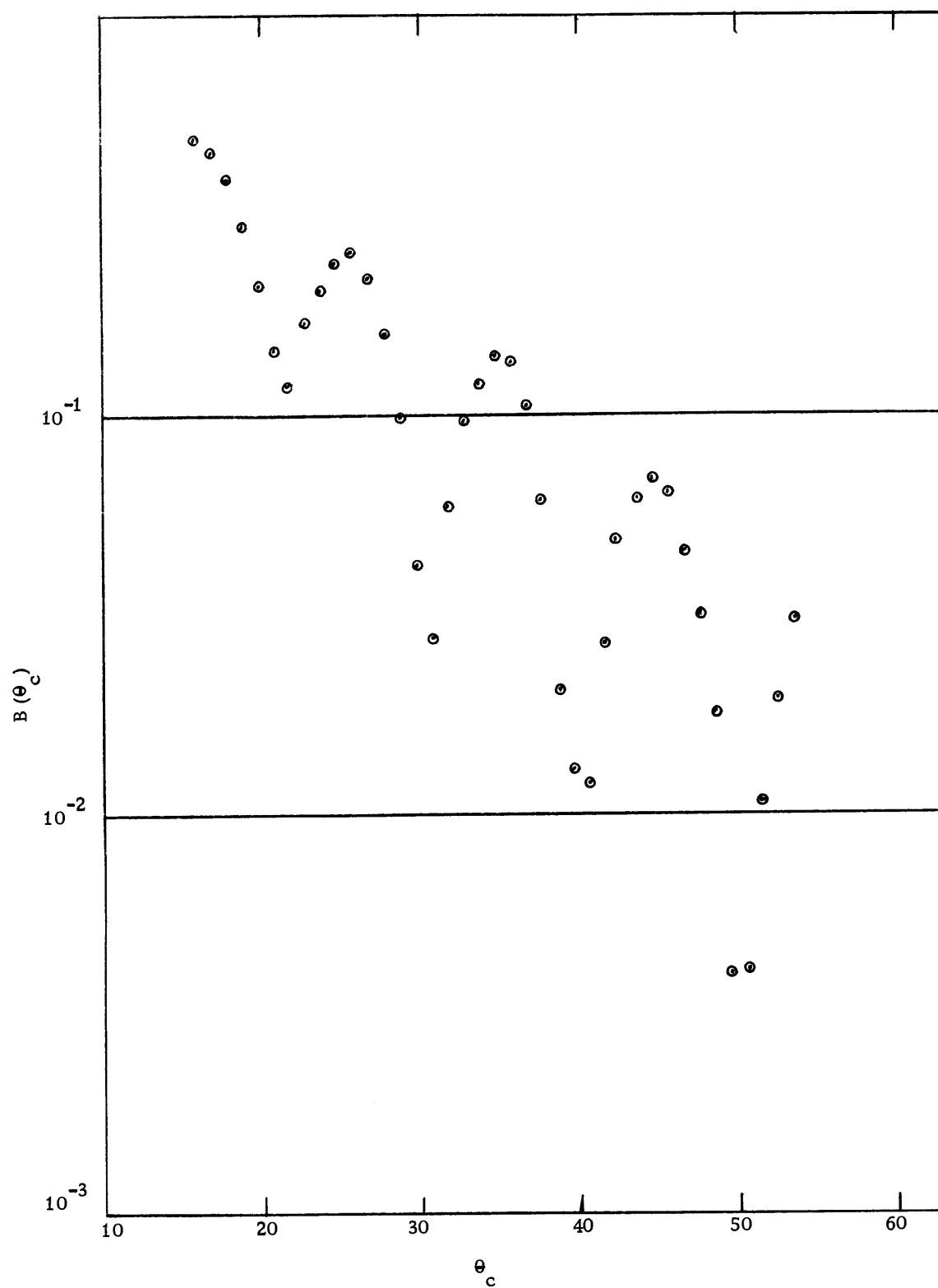


Figure 33. Ratio of differential elastic scattering cross section to Rutherford cross section  $-B(\theta_c)$ .

$R(\theta_L)$  must be transformed into center of mass coordinates.

Let

$$R(\theta_L) = \frac{\sigma(\theta_L) \Delta\Omega_n^L}{\sigma(40_L) \Delta\Omega_m^L} \quad (5-7)$$

and

$$R(\theta_c) = \frac{\sigma(\theta_c) \Delta\Omega_n^c}{\sigma(40_c) \Delta\Omega_m^c} \quad (5-8)$$

The solid angle correction expression is given as follows (19):

$$\sigma(\theta_L) \Delta\Omega_n^L = \sigma(\theta_c) \Delta\Omega_n^c \quad (5-9)$$

where

$$\frac{\Delta\Omega_n^L}{\Delta\Omega_n^c} = \frac{\sin\theta_L d\theta_L}{\sin\theta_c d\theta_c} = \frac{1 + \gamma \cos\theta_c}{(1 + \gamma^2 + 2\gamma \cos\theta_c)^{3/2}} = \beta \quad (5-10)$$

and

$$\gamma = \left( \frac{M' + m'}{M + m} \frac{mm'}{MM'} \frac{T}{Q - W' + T} \right)^{1/2} \quad (5-11)$$

For inelastic scattering,  $M = M'$ ,  $m = m'$ , and  $Q = 0$ . So if  $M = 70$ ,  $m = 4$ ,  $T = 42.5$  Mev, and taking  $W'$  less than 5 Mev (the excitation energy of the target nucleus) then to good accuracy,  $\gamma = 0.0572$ .

So now,

$$\sigma(\theta_L) = \sigma(\theta_c) \frac{\Delta\Omega_m^c}{\Delta\Omega_n^L} = \beta \sigma(\theta_c) \quad (5-12)$$

$$\sigma(40_L) = \sigma(40_c) \frac{\Delta\Omega_m^c}{\Delta\Omega_n^L} = \beta \sigma(40_c) \quad (5-13)$$

Then

$$R(\theta_L) = \frac{\beta_{\sigma}(\theta_c) \Delta \Omega_n^L}{\beta_o \sigma(40_c) \Delta \Omega_m^L} \quad (5-14)$$

$$= \frac{\beta_{\sigma}(\theta_c) \beta \Delta \Omega_n^c}{\beta_o \sigma(40_c) \beta_o \Delta \Omega_m^c} \quad (5-15)$$

Finally, the relationship between  $R(\theta_L)$  and  $R(\theta_c)$  is given by:

$$R(\theta_c) = (\beta_o / \beta)^2 R(\theta_L) \quad (5-16)$$

The Rutherford cross section is calculated from the usual formula:

$$\sigma_{RUTH}(\theta_c) = \left[ \frac{Z_1 Z_2 e^2}{2 \mu v_o^2} \right] \frac{1}{\sin^4 \theta_c / 2} \quad (5-17)$$

The energy of the incident particle in the center of mass system is found from

$$E_c = \frac{1}{2} \mu v_o^2 = \left( \frac{m_2}{m_1 + m_2} \right) E_L \quad (5-18)$$

Values of  $K$  which are calculated vary somewhat for the various angles. Those values which seem to deviate most radically from the mean arise from those values of  $B(\theta_c)$  which lay in the dips of the curve. The curve is changing rapidly at these points and accurate values for  $B(\theta_c)$  are very difficult to determine. So, it is not surprising that the corresponding values of  $K$  are poorly determined.

It must be pointed out that the data which make up the curve of Figure 33 show uncertainties of the order of 20 percent. Thus, the cross sections should not be trusted any closer than this as a minimum. Figures 34-41 show the final results for the absolute differential cross sections. The value of  $K$  chosen was the average of the values calculated for each angle. The error is given by the average deviation from the mean. So  $K = 5.3 \pm 0.2$ .

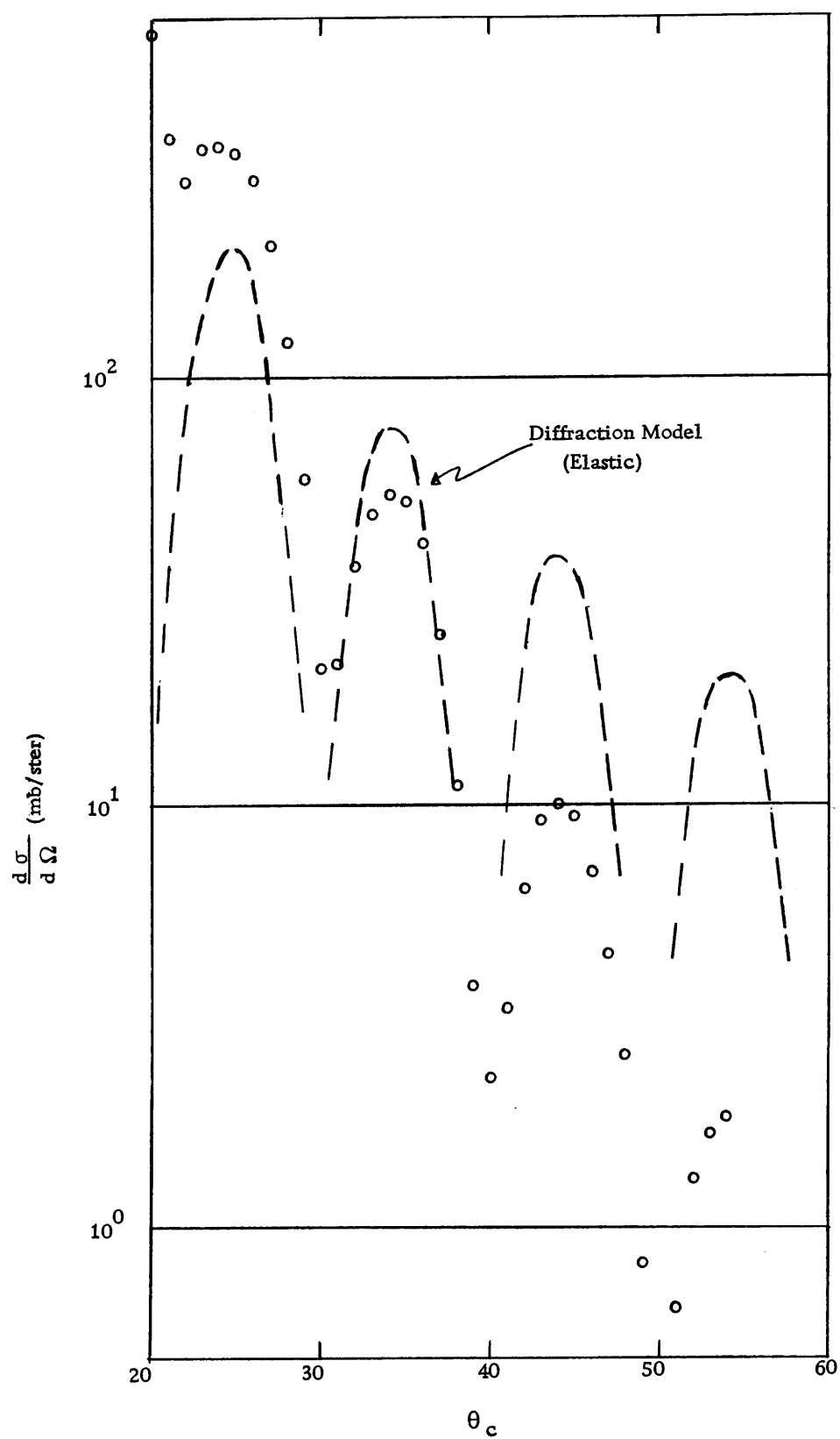


Figure 34. Differential elastic scattering cross section.  $Q = 0$ .

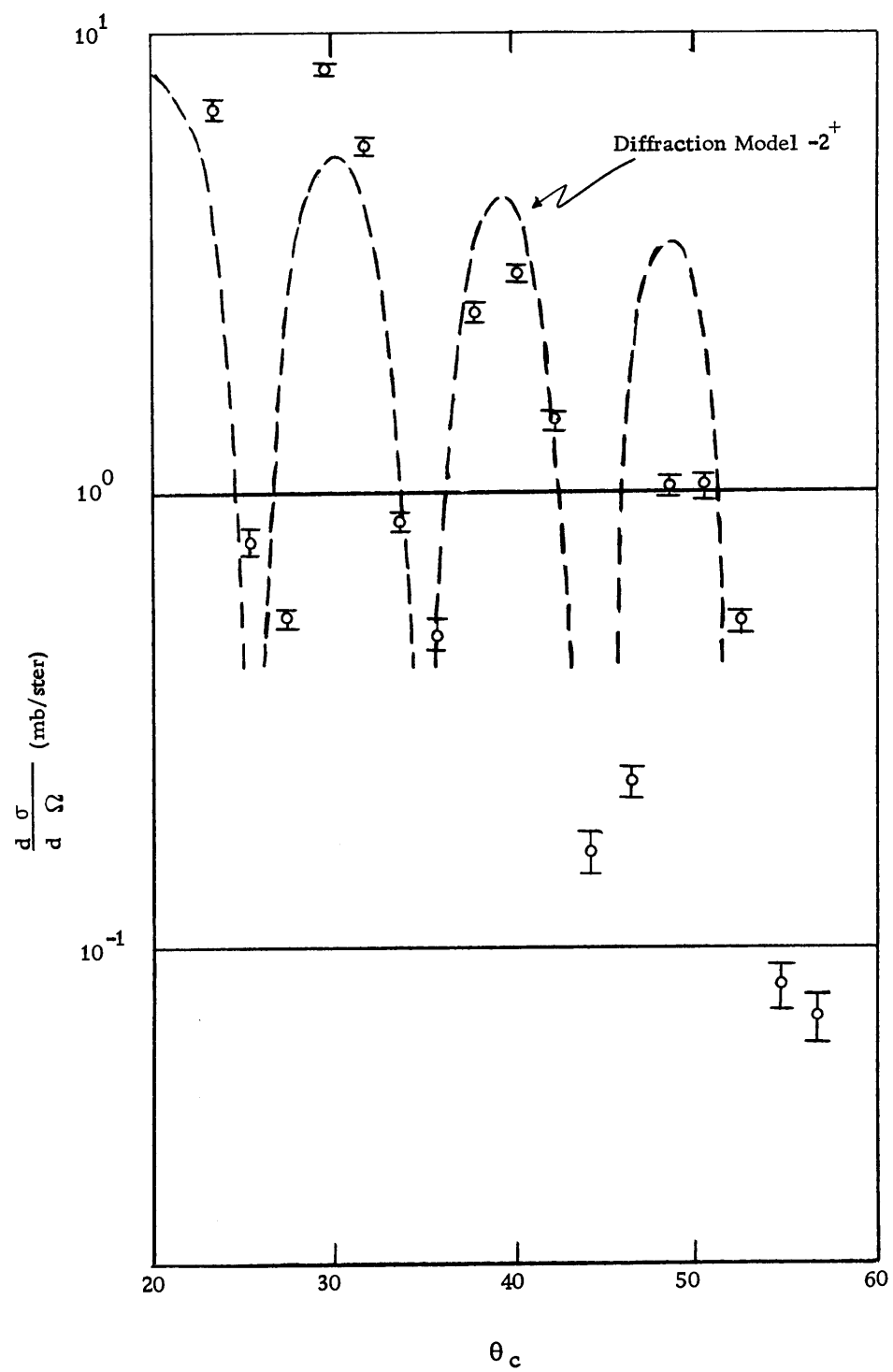


Figure 35. Differential scattering cross section.  $Q = -875$  kev.

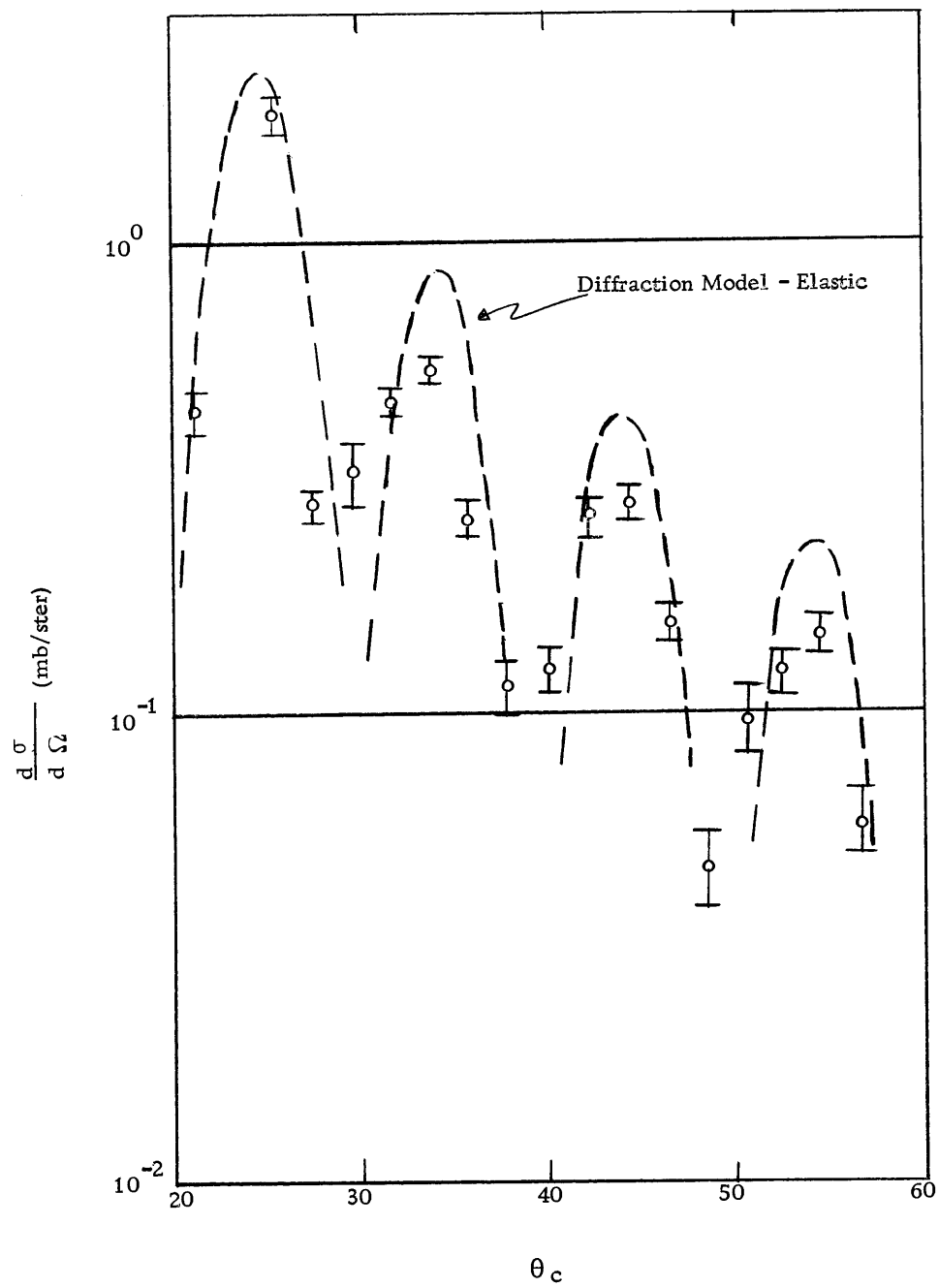


Figure 36. Differential scattering cross section.  $Q \approx 1750$  kev.



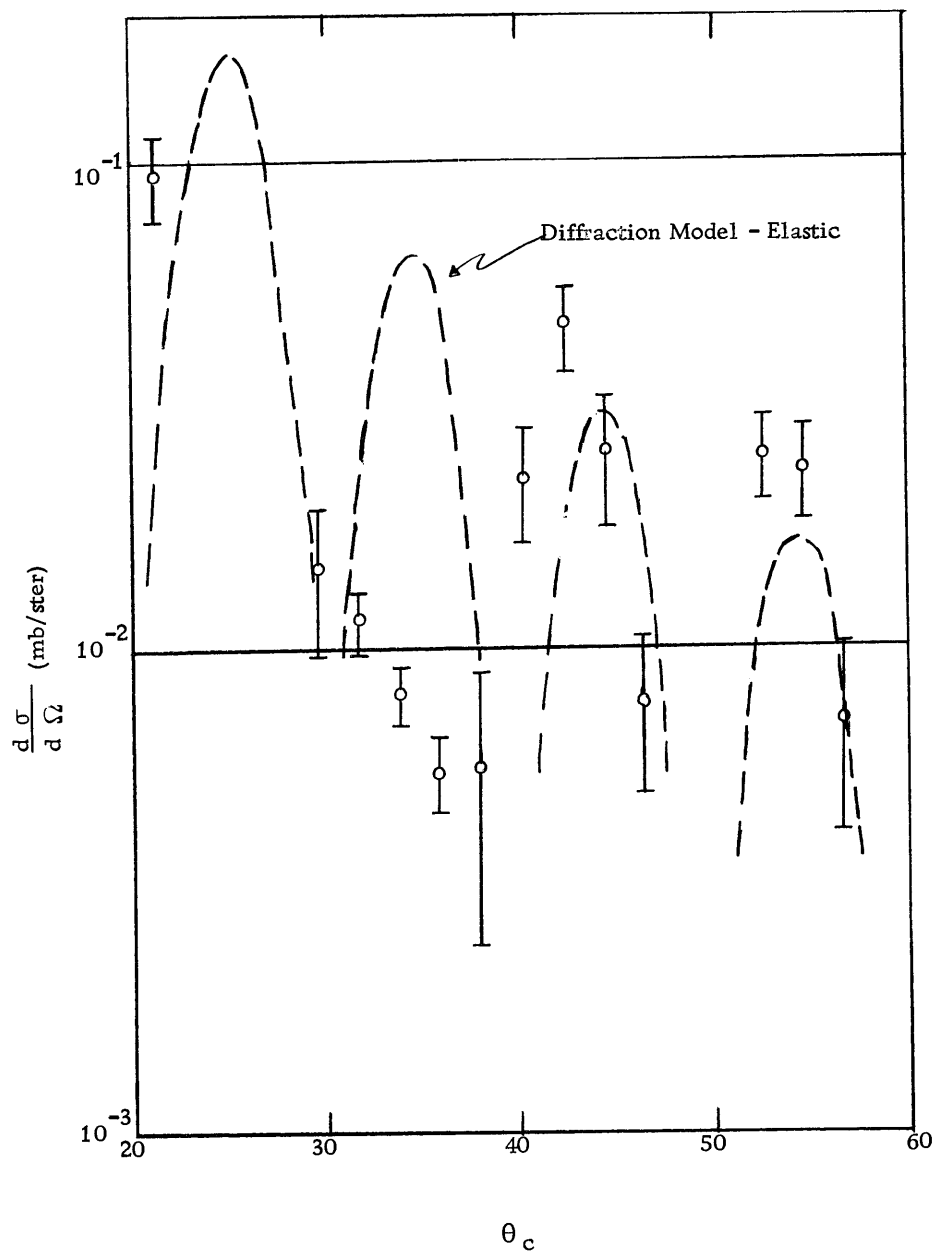


Figure 37. Differential scattering cross section.  $Q = -1960$  kev.

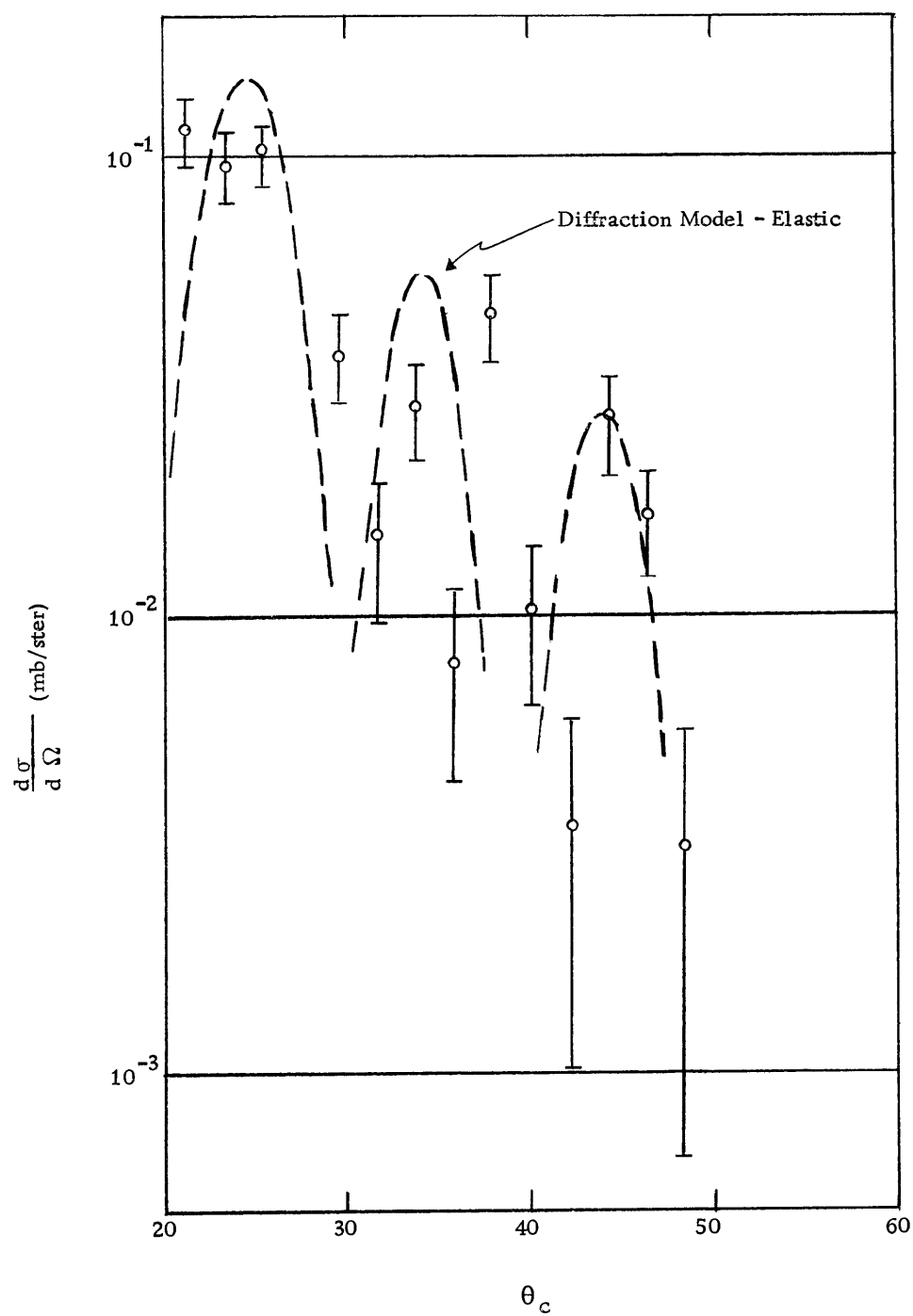


Figure 38. Differential scattering cross section.  $Q = -2360$  kev.

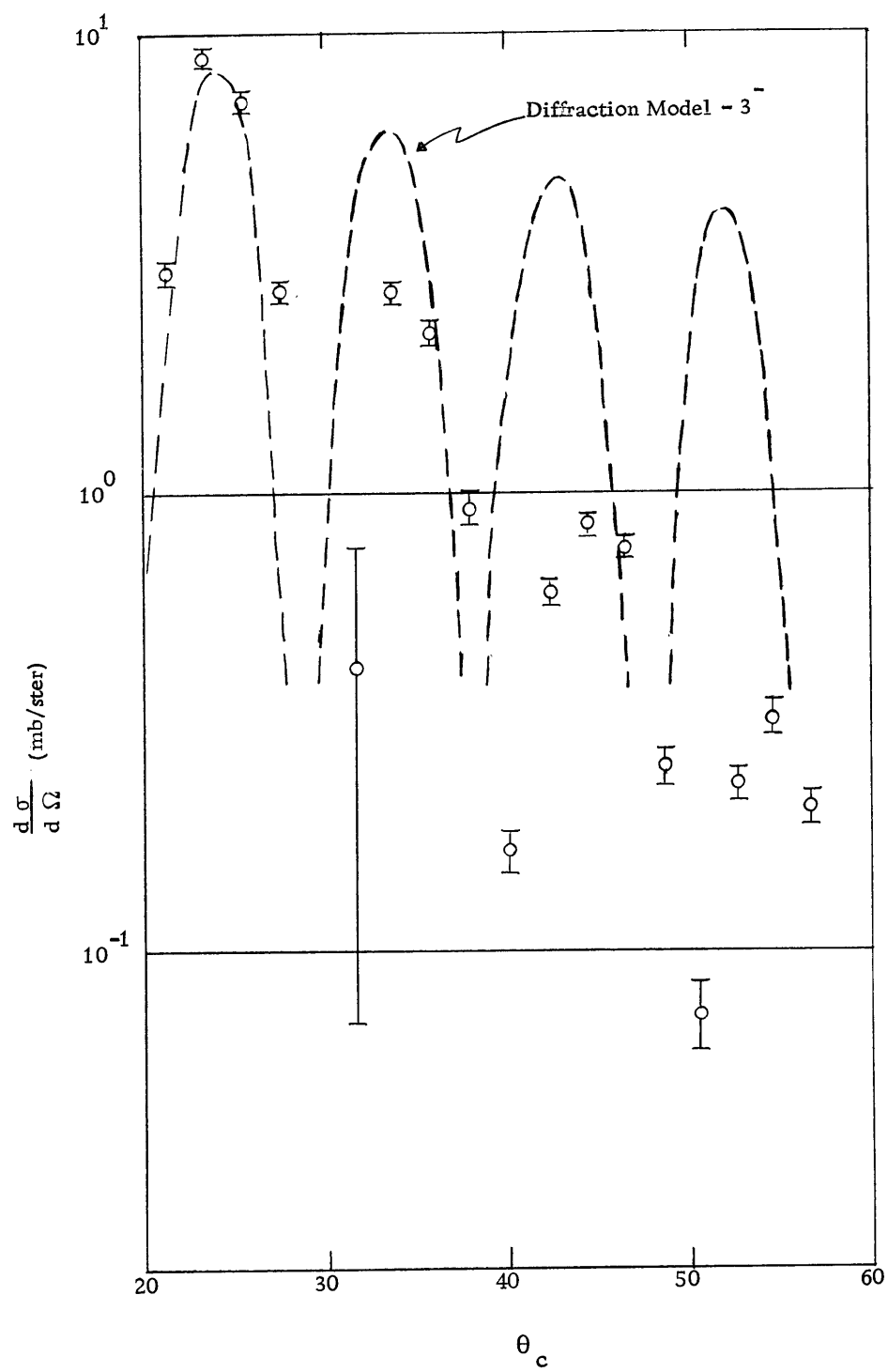


Figure 39. Differential scattering cross section.  $Q = -2810$  kev.

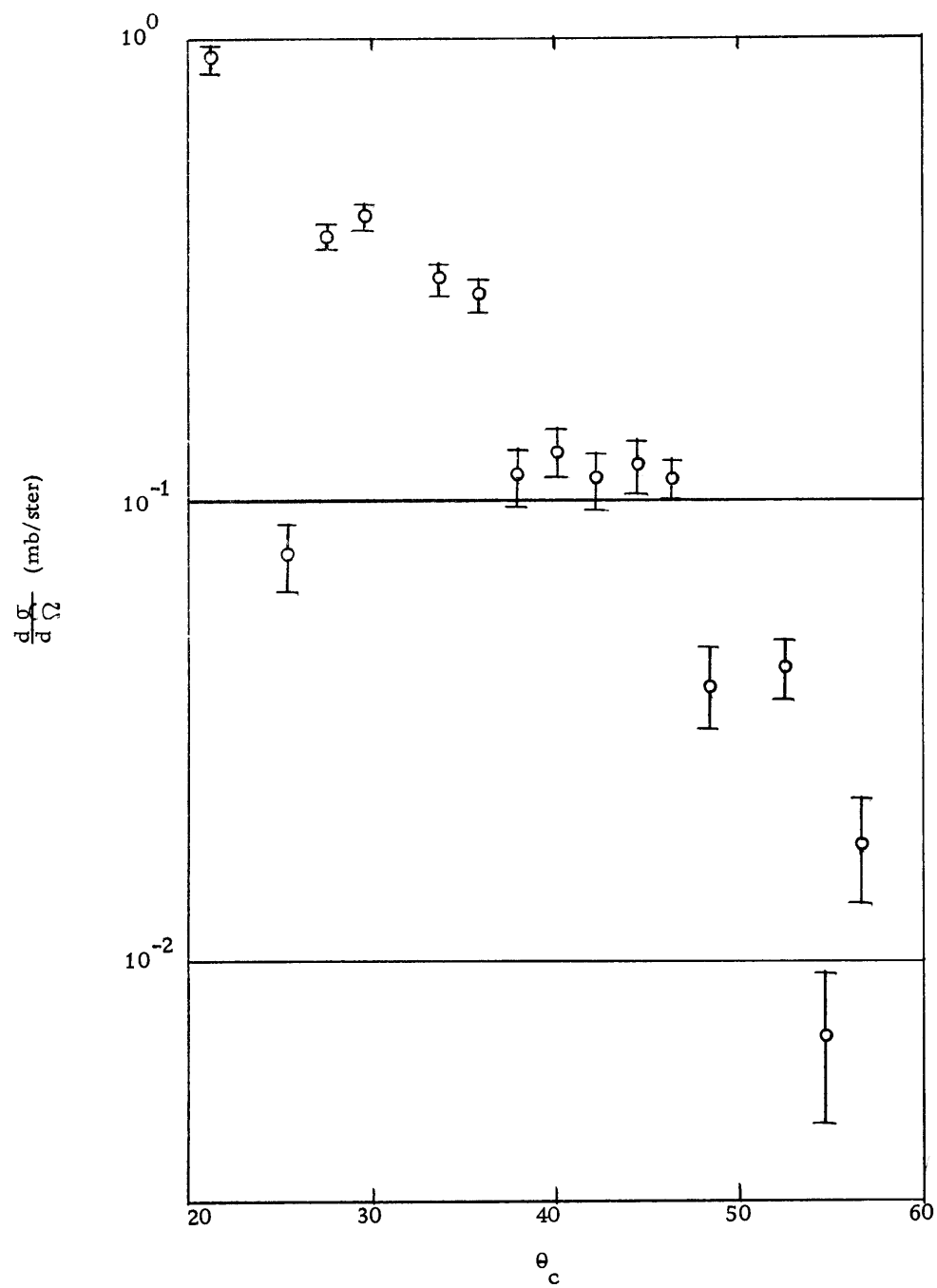


Figure 40. Differential scattering cross section,  $Q = -2990$  kev.

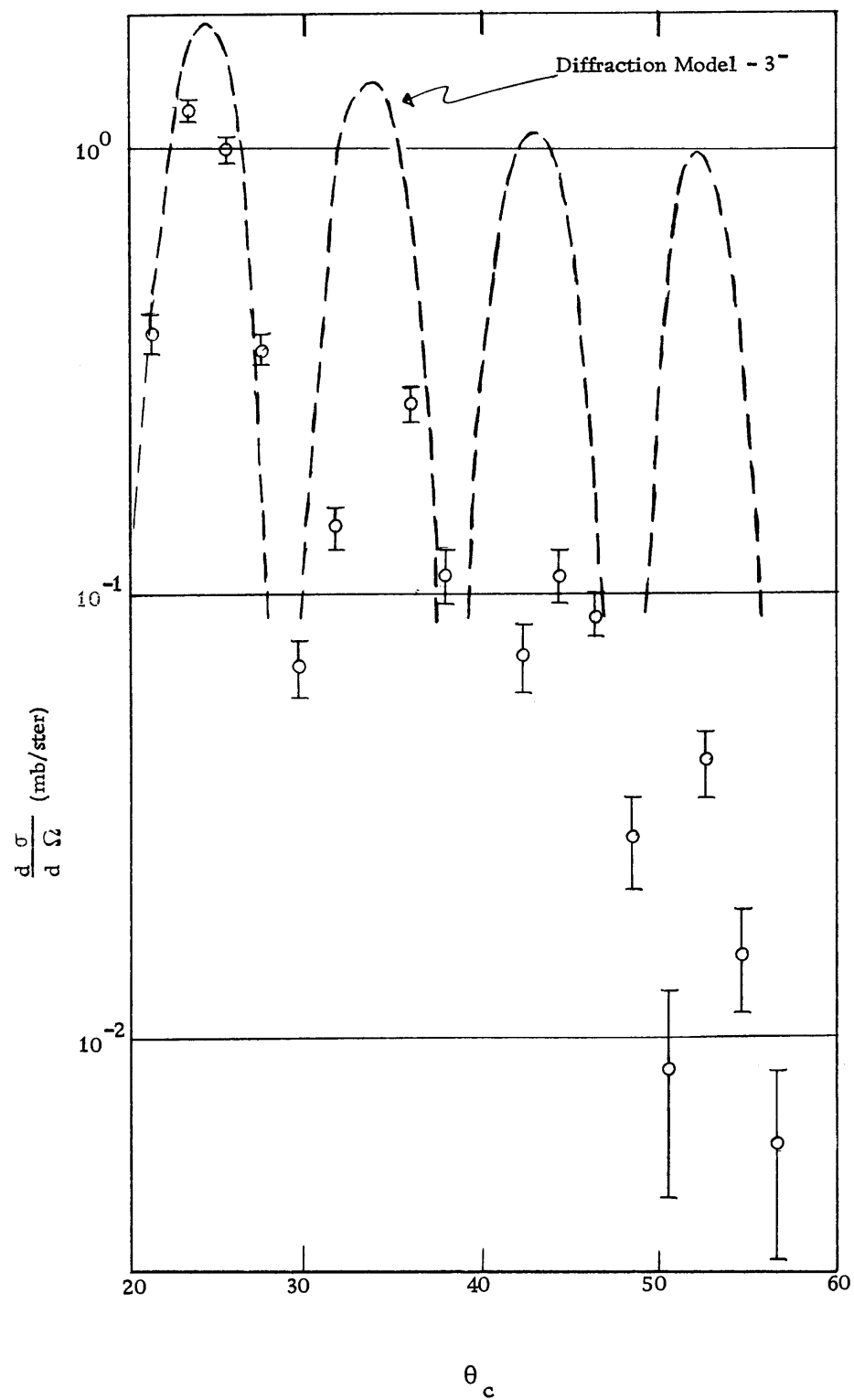


Figure 41. Differential scattering cross section.  $Q = -3295$  kev.

## DISCUSSION OF SCATTERING EXPERIMENT

### Introduction

An understanding of the cross sections obtained from alpha particle scattering has been achieved through the introduction of the theory of direct reactions. The direct reaction theory is based on the assumption the interaction of an incident projectile with a nucleus involves a small fraction of all the target particles. This is just opposite to the basic assumption of the Compound Nucleus Model, in which the incident particle is absorbed by the nucleus and shares its energy with all of the target nucleons. Direct reaction theory is able to account for the oscillating, diffractionlike, angular distributions of many types of reactions, in particular, elastic and inelastic scattering cross sections. The formalism most widely used in direct reaction theory is that of Distorted Wave Born Approximation (DWBA). The interaction potential between the projectile and a target nucleon is treated as a perturbation between distorted incoming and outgoing waves. The distorted waves are generated by an optical potential. Since the optical potential is determined phenomenologically, parameters are determined by fitting calculated elastic cross sections to experimental distributions. The calculations, of course, require a fast computer.

A simple method of describing some of the features of elastic and inelastic scattering cross sections has been developed for the case of incident projectiles which are strongly absorbed, such as alpha particles,  $\text{He}^3$  particles, and deuterons (3). The problem is viewed as the scattering of a plane wave from a perfectly absorbing sphere; analogy is made to Fraunhofer scattering of light from a black disc. For elastic scattering, the usual diffraction pattern for a plane wave incident upon an opaque disc of radius  $R_o$  is obtained:

$$\frac{d\sigma}{d\Omega} = (kR_o)^2 \left[ \frac{J_1(2kR_o \sin\theta/2)}{2kR_o \sin\theta/2} \right]^2 \quad (6-1)$$

where  $J_1(x)$  is the first order Bessel function,  $\theta$  is the scattering angle, and  $k$  is the wave number of the scattered particle.

In the spherical nuclei, where excitations can be described as excitations of surface oscillations or vibrational phonons, the diffraction model has been applied by Blair (3) to inelastic processes. The surface of the nucleus projected on the plane perpendicular to the incident wave no longer has a circular shadow but has a shape given by:

$$R = R_o \left[ 1 + \sum_{\lambda\mu} a_{\lambda\mu} Y_{\lambda}^{\mu*} \right] \quad (6-2)$$

where  $a_{\lambda\mu}$  is related to phonon creation and destruction operators, equation 4-5. Cross sections for one phonon excitations of order  $l$

become:

$$\frac{d\sigma}{d\Omega}(0 \quad \ell) = (kR_o)^2 \sum_{\substack{m=-\ell, \\ \ell+2, \\ \ell}}^{\ell} \left( \frac{2\ell+1}{4\pi} \right) \left( \frac{\hbar\omega}{2c} \right)_{\ell} \left[ \frac{(\ell-m)! (\ell+m)!}{(\ell-m)! (\ell+m)!} \right] J_{|m|}^2(kR_o \theta) \quad (6-3)$$

In equation 6-3, note that for  $\ell$  even (odd) only the even (odd) order Bessel functions appear. The odd (even) order Bessel functions have even (odd) parity. Upon comparing equation 6-3 with equation 6-1, the Blair Phase Rule appears; namely, odd  $\ell$  phonon states have distributions which are in phase with the elastic cross sections, while even  $\ell$  phonon states have distributions which are out of phase.

Equations 6-1 and 6-3 can reproduce the periodicity of the experimental angular distributions, but these relations cannot predict the magnitude of the cross sections except in the forward direction. As the angle increases, the magnitude of the calculated cross section does not decrease fast enough to fit experimental distributions. The difference has been shown (4) to be a result of the assumption of a sharp nuclear surface, i. e. the "sharp cutoff" model of Blair. By considering a diffuse region at the nuclear surface rather than an abrupt change in density, all of the features of the elastic (14) and inelastic (4) cross sections can be explained.

Inopin and Berezhnoy (23) have shown that cross sections can be given by:



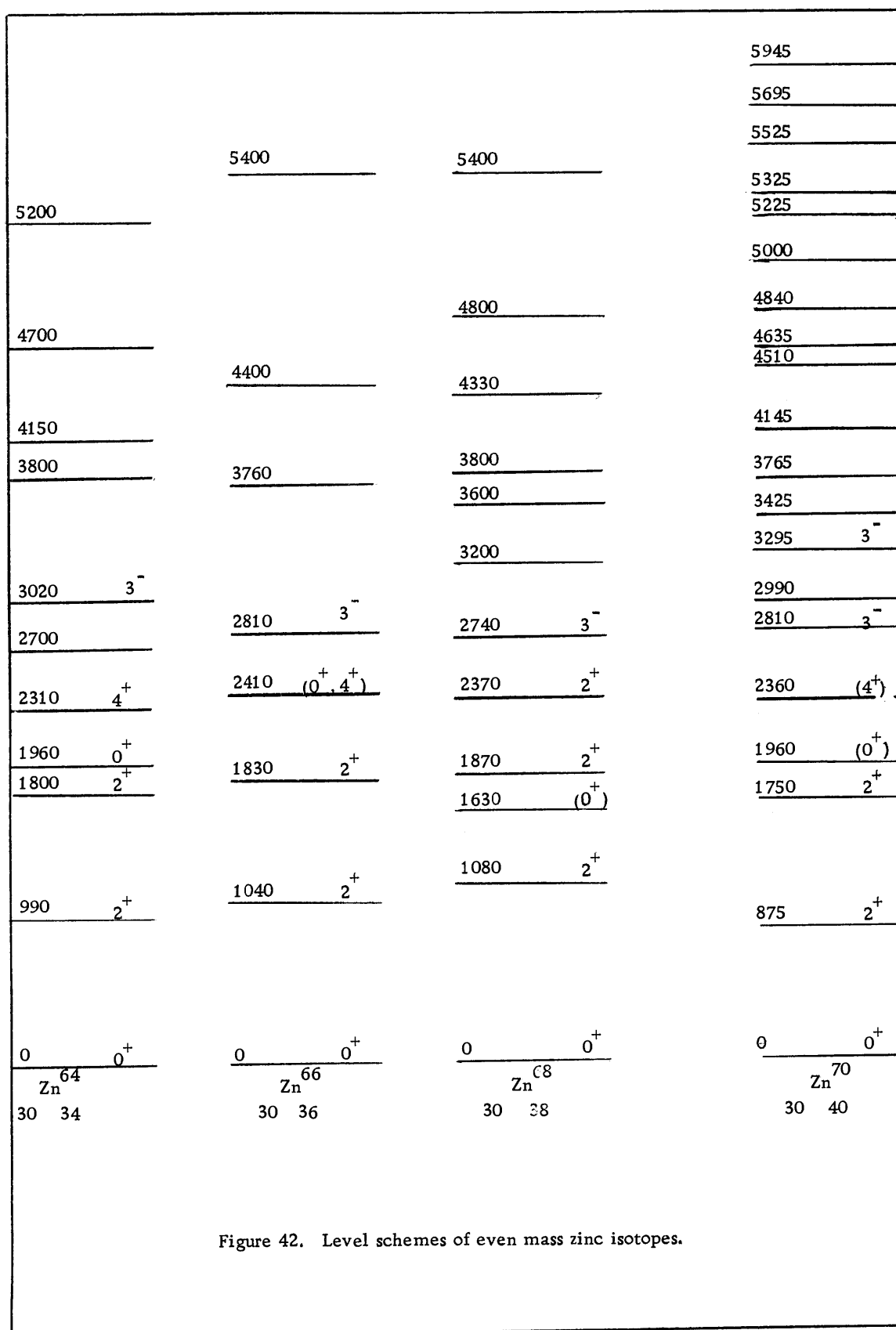
$$\left. \frac{d\sigma}{d\Omega} \right|_{\text{exp}} = \left. \frac{d\sigma}{d\Omega} \right|_0 F^2(\theta) \quad (6-4)$$

where  $d\sigma/d\Omega|_0$  is found from equation 6-1 or 6-3.  $F^2(\theta)$  is a continuous function of the scattering angle and results from the assumption of a diffuse boundary layer; this function is the same for elastic and inelastic scattering.

### Discussion of Results

Table 4 indicates spins and parities deduced for several of the levels whose cross sections were determined. The phase rule permits definite assignments of parity to the 875, 2810, 3295, and 3425 kev levels as is shown in Figures 34 through 41.

Figure 42 is a comparison of the level scheme of  $\text{Zn}^{70}$  with schemes of the isotopes  $\text{Zn}^{64}$ ,  $\text{Zn}^{66}$ , and  $\text{Zn}^{68}$  (10, 28). Comparison, particularly with the  $\text{Zn}^{64}$  scheme, suggests the following spin assignments: 875 ( $2^+$ ), 1750 ( $2^+$ ), 1940 ( $0^+$ ), 2360 ( $4^+$ ), and 2810 ( $3^-$ ). The vibrational model predicts a triplet of levels at an energy twice that of the first excited  $2^+$  state. These levels result from the coupling of two  $l = 2$  phonons to resultant total spins of  $0^+$ ,  $2^+$ , and  $4^+$ . The degeneracy is removed by residual interactions, producing a triplet of levels whose "center of mass" lies at  $2\hbar\omega$  ( $\hbar\omega = 875$  kev). The 1750, 1940, and 2360 kev levels will be tentatively identified as members of this triplet.



In each of the Figures 36, 37, and 38, the differential cross sections for exciting the triplet of levels, a periodicity of the peaks occurs. The maxima of these peaks appear intermediate to those for the elastic and the positive parity distributions. This type of behavior is seen in the cross section for the excitation of a  $4^+$  level in  $\text{Ni}^{58}$ . Buck (11) has shown the result can be attributed to an interference between two modes of excitation of a  $4^+$  spin state. One mode of excitation results from the application of a  $a_{2m}^2$  which operates once. The other excitation mode is a two step process in which  $a_{2m}$  operates twice.

The positions of the maxima in the angular distribution in Figure 41 allows an assignment of negative parity to the 3295 kev level. Since the 2810 kev level has been identified as a  $3^-$  state, the 3295 kev level, as the next higher negative parity state, might be considered for a  $5^-$  assignment. However, the energy is low and a calculation using equation 6-3 for a  $\ell = 5$  transition indicates there should be no dip in the cross section at  $20^\circ$ , in contrast to the distribution for a  $\ell = 3$  transition. In Figure 41 it is apparent that a dip does occur at  $20^\circ$ , thus ruling out a  $5^-$  assignment. Broek (10) discussed the existence of additional  $3^-$  levels in  $\text{Zn}^{64}$ ,  $\text{Zn}^{66}$ , and  $\text{Zn}^{68}$ , isotopes, but in those isotopes, the second  $3^-$  level lies about 1.5 Mev higher in energy than the first level.

The level at 3760 kev has a counterpart in the level schemes

of the other zinc isotopes shown in Figure 42; however, none of these levels have been identified.

Using equations 6-1 and 6-3, sharp cutoff diffraction model cross sections were calculated. Maxima in the theoretical distributions agree with the positions of maxima in the experimental cross sections when  $R_o$  has the value 7.15 f. For the alpha particle,  $R = r'_o \times A^{1/3}$ , where  $r'_o = 1.31$  f (35), and for the  $Zn^{70}$  nucleus  $R = r_o \times A^{1/3}$ , where  $r_o = 1.23$  f. This value of  $r_o$  is in agreement with the value determined by Wilson and Sampson (46) for the other zinc isotopes,  $r_o = 1.23 \pm 0.2$  f.

Equations 6-1 and 6-4 are used to find  $F^2(\theta)$  for the elastic cross section. The cross section of equation 6-3 for  $\ell = 3$  is then used to find  $\beta_3^2 F^2(\theta)$ . The  $F$  function is the same for each case and  $\beta_3$  can be computed. Using the  $F$  function,  $\beta_2$  is then computed. Values of  $\beta_2$  and  $\beta_3$  obtained are small, i. e.  $\beta_2 = 0.10$  and  $\beta_3 = 0.07$ . (These values are a factor of two smaller than other calculations). The difference is due primarily to the error in  $B(\theta_c)$  and, to a lesser degree, to the statistical uncertainty in the experimental cross sections. Using equations 6-3 and 6-4 for  $\ell = 2$  and  $\ell = 3$ , the ratio of the quadrupole to octupole deformation was determined to be  $\beta_2/\beta_3 = 1.5$ . Since this value can be determined from the experimental data and  $R(2^+)/R(3^-)$ , where  $R$  is defined in equation 5-2, the error introduced from  $B(\theta_c)$  is avoided. Thus, the ratio

$\beta_2/\beta_3$  has an estimated uncertainty of about  $\pm 0.2$ .

Stelson and McGowan (41) reported a value of  $\beta_2 = 0.228$  for  $\text{Zn}^{70}$  deduced from the results of Coulomb excitation experiments. Wilson and Sampson (46) indicate several values of  $\beta_2$  for each of the even-even isotopes of zinc; the different values depending on the method of determination. For inelastic scattering of 22 Mev alpha particles  $\beta_2$  is of the order of 0.19 for these isotopes. These analyses suggest the values for  $\beta_2$  and  $\beta_3$  for  $\text{Zn}^{70}$  determined above are too small.

Considering the first  $2^+$  levels in the zinc isotopes of Figure 42, it is seen that the energy increases as the neutron number changes from 34 to 36 to 38; however, at  $N = 40$  the energy suddenly shifts downward. Similarly, the  $3^-$  level energies decrease with increasing  $N$  until  $N = 40$  where the energy suddenly shifts upward. Stelson and McGowan (41) noticed this effect in the zinc and germanium isotopes at  $N = 40$  and suggested the  $N = 38$  nuclei are less susceptible to quadrupole deformation. Sharff-Goldhaber and Weneser (38) first noted the sudden changes in the energy of the first excited states which occur as  $A$  is varied; they indicated such phenomena occur at shell closures. Thus, it is concluded a minor neutron shell has filled at  $N = 40$ .

These results support the description of  $\text{Zn}^{70}$  as a "good" vibrational nucleus. Further, the energy of the second excited level

is exactly twice the energy of the first level, in agreement with predictions of the vibrational model.

## CONCLUSIONS

The value of the high precision gamma ray energy and relative intensity measurements in deducing decay schemes has been demonstrated. In particular, several ambiguities in the decay scheme have been eliminated by the present study. Results of the gamma ray analysis are in essential agreement with those reported by Li and Monaro (27). However, precision of the energy measurements in this study is better by almost an order of magnitude. In addition, several gamma rays (i. e. 1140, 1283, and 1758 kev) were detected which were not reported previously. Measurements of the lifetimes of several levels in  $\text{Ga}^{71}$  also agree.

In Figure 20 the assignment of  $1/2^-$  to  $\text{Zn}^{71}$  and of  $9/2^+$  to  $\text{Zn}^{71m}$  can be explained by the fact that the pairing energy for two equivalent nucleons increases rapidly with the orbital angular momentum. Thus, in 2.2 Minute  $\text{Zn}^{71}$  the 41st neutron is in a  $2p_{1/2}$  state and the 39th and 40th neutrons are coupled as  $1g_{9/2}$  particles even though the  $2p_{1/2}$  neutron level lies lower than the  $1g_{9/2}$  level. The 4.1 hour  $\text{Zn}^{71m}$  state is then viewed as a single  $1g_{9/2}$  neutron outside of the closed  $2p_{1/2}$  subshell.

The  $9/2^+$  level decays by allowed beta emission to positive parity states in  $\text{Ga}^{71}$ , particularly to the 1495 kev level. The beta decay probability is about  $6 \times 10^{-5} \text{sec}^{-1}$ . From the energies of the

beta transitions in the decay of  $\text{Zn}^{71}$  and  $\text{Zn}^{71m}$  (44), the energy separation between these two states of  $\text{Zn}^{71}$  is estimated to be  $350 \pm 50$  kev. Considering the M4 gamma ray transition of 350 kev as a single neutron transition, the decay probability is  $1 \times 10^{-5} \text{sec}^{-1}$ . There should be competition between the two possible modes of decay of the isomeric level. A careful search was made for gamma rays in the energy region of 350 kev; if a gamma ray is present, its relative intensity is less than 0.001. Bohr and Mottelson (7) report a hindrance factor of 0.06 for the M4 transition between the isomeric states of  $\text{Zn}^{69}$ . Since the gamma decay of  $\text{Zn}^{69}$  is probably a simple  $1g_{9/2}$  to  $2p_{1/2}$  neutron transition, while for  $\text{Zn}^{71m}$  a recoupling of three neutrons is involved, it seems reasonable to argue that the hindrance factor will be somewhat smaller than 0.06 for the  $\text{Zn}^{71}$  transition. Considering such a small hindrance factor along with the decay probabilities above, the intensity of the 350 kev gamma ray would be less than 0.001.

Unified Model predictions for energy levels in  $\text{Ga}^{71}$  are in good agreement with the energies of the first three excited levels in the experimental scheme. These are negative parity states. The 1495 and 2778 kev levels of positive parity are also fitted to the experimental scheme. Calculations for these two levels involve two parameters,  $E_3$  and  $\eta$ , and almost any combination of  $E_3$  and  $\eta$  could predict the same energies. This ambiguity is removed by requiring



certain consistencies between the calculations for the positive and negative parity levels. Thus, the value for  $E_3$  was chosen to be 25% smaller than the value suggested by Kisslinger and Sorensen (24). This reduction was suggested by the results found for  $E_1$  and  $E_2$ , which also had to be reduced by the 25% factor to obtain agreement between experiment and theory. The values of the coupling parameters for best fit came out to be  $\xi = 2.50$  and  $\eta = 1.25$ . From the definitions  $\xi = \beta_2 V_0 / \sqrt{5}$  and  $\eta = \beta_2 V_0 / \sqrt{7}$ , values for  $V_0$  were calculated using  $\beta_2 = 0.18$  and  $\beta_3 = 0.12$ ; (The value of  $\beta_3$  follows from the ratio  $\beta_2 / \beta_3 = 1.5$  determined in the last chapter.)  $V_0$  then has the values of 31 and 28 Mev, respectively. This agreement points out the consistency in the calculations. (In calculating wave functions for the Saxon-Woods potential in Chapter 4,  $V_0$  was of the order of 40 Mev, the exact value being sensitive to the binding energy chosen.)

In Figure 29 for the positive parity level calculation, results were shown for the case where the calculated eigenstates were mixtures of octupole-single particle states and quadrupole-single particle states. Only the 1495 kev level was described for a value of  $\eta = 0.75$ . This value of  $\eta$  leads to a value of  $V_0 = 17$  Mev. By comparing these results to those in the previous paragraph, where only octupole-single particle state mixtures were included, it is apparent that mixtures of octupole and quadrupole excitations do

not occur.

The fitting of the calculated energy levels to experiment is not a very sensitive test of the model. A much more demanding test would be agreement between calculated and experimental values of static nuclear moments and of transition probabilities. The magnetic dipole moment for the eigenvector of Table 3 was calculated using the formula:

$$\begin{aligned}
 \langle \mu \rangle_{I=M} = \mu_N \left[ \frac{I(2I+1)}{I+1} \right]^{1/2} \sum_{\substack{j, N, R \\ j', N', R'}} a(j, NR, I) a(j', N'R', I) \left\{ g_R (-1)^{I+j-R} \right. \\
 \times \delta_{NN'} \delta_{RR'} \delta_{jj'} \delta_{\ell\ell'} [R(R+1)(2R+1)]^{1/2} W(RR II; 1 j) \\
 + g_\ell (-1)^{R-\ell+\frac{1}{2}+j+j'-I} \delta_{RR'} \delta_{NN'} \delta_{\ell\ell'} [(2j+1)(2j'+1)]^{1/2} \\
 \times W(jj' II; 1 R) W(\ell\ell jj'; 1 \frac{1}{2}) + g_s (-1)^{\ell+\frac{1}{2}+R+I} \delta_{NN'} \delta_{RR'} \delta_{\ell\ell'} \\
 \left. \times (3/2)^{1/2} [(2j+1)(2j'+1)]^{1/2} W(jj' II; 1 R) W(jj' \frac{1}{2} \frac{1}{2}; 1 \ell) \right\} \quad (7-1)
 \end{aligned}$$

The electric quadrupole moment was calculated using:

$$\begin{aligned}
\langle Q \rangle_{I=M} = \langle r^2 \rangle \left[ \frac{I(2I-1)(2I+1)}{(I+1)(2I+3)} \right] \sum_{\substack{jNR \\ j'N'R'}} a(j, NR, I) a(j', N'R', I) \left\{ \frac{16\pi}{5} \right. \\
x (1-Z^2/A)(-1)^{I+j-R} [2j'+1]^{1/2} \langle j' || Y_2 || j \rangle \delta_{NN'} \delta_{RR'} \\
x W(jj'II; 2R) + \frac{3Z}{\sqrt{5}\pi} \left( \frac{\hbar\omega}{2C} \right)^{1/2} (-1)^{I-j} \delta_{jj'} \delta_{\ell\ell'} [(-1)^{R'} (2R'+1)]^{1/2} \\
x \langle N'R' || b^+ || NR \rangle + (-1)^R (2R+1)^{1/2} \\
x \langle N'R' || b || NR \rangle \left. W(RR'II; 2j) \right\} \quad (7-2)
\end{aligned}$$

(These equations are derived in Appendix A.) Results are shown in Table 5, along with the single particle estimates. Note that the calculation of  $Q$  comes out with the wrong sign. This implies that this model is not adequate for calculating quadrupole moments.

Table 5. Static nuclear moments.

Energy Level (kev)	$\mu_{\text{exp}}$ (nuclear magnetons)	$\mu_{\text{calc}}$	$Q_{\text{exp}}$ ( $\times 10^{-24} \text{ cm}^2$ )	$Q_{\text{calc}}$
g.s.	2.565	+2.56	+0.147	-0.15
488	-	+1.20		
512	-	-0.51		
1108	-	+1.73		
	$\mu_{\text{sp}} = 3.79$		$Q_{\text{sp}} = +0.0625$	

In Table 5 the agreement between  $\mu_{\text{exp}}$  and  $\mu_{\text{calc}}$  seems extremely fortuitous, particularly, considering the large correction to the single particle estimate which has to be made. The agreement for  $Q$  is not very good; the result is dominated by the collective term which is negative in sign.

Short lifetimes of the 488, 512, and 1108 keV levels in  $\text{Ga}^{71}$  suggest that only M1 and E2 transitions are involved. Reduced transition probabilities are calculated as follows;

$$\begin{aligned}
 B(E2) = \frac{2I'+1}{2I+1} \left| \sum_{\substack{jNR \\ j'N'R'}} a(j', N'R', I') a(j, NR, I) \right\{ (-1)^{I'+j-R} [(2j'+1)(2j+1)]^{1/2} \\
 \times W(jj'II'; 2R) \gamma_1 \langle j' || Y_2 || j \rangle \delta_{NN'} \delta_{RR'} \\
 + \gamma_2 (-1)^{I'-j} [(2R+1)(2R'+1)]^{1/2} [ (-1)^R \langle N'R' || b || NR \rangle \\
 + (-1)^{R'} \langle N'R' || b^+ || NR \rangle] W(RR'II'; 2j) \delta_{jj'} \delta_{\ell\ell'} \} \Big|^2 \quad (7-3)
 \end{aligned}$$

where

$$\gamma_1 = (1 - Z/A^2) \langle r^2 \rangle \quad \gamma_2 = \frac{3}{4\pi} \left( \frac{\hbar\omega}{2C} \right)^{1/2} Z e R_o^2$$

and

$$\begin{aligned}
B(M1) = & \frac{3}{4\pi} \mu_N^2 (2I'+1) \left| \sum_{jj'NR} a(j', NR, I') a(j, NR, I) \left\{ (-1)^{I'+R+\ell} \frac{1}{2} [(2j+1) \right. \right. \\
& \times (2j'+1)]^{1/2} [g_\ell (-1)^{j+j'} [\ell(\ell+1)(2\ell+1)]^{1/2} W(j'j\ell\ell; 1 \frac{1}{2}) \\
& + g_s (\frac{3}{2})^{1/2} W(j'j \frac{1}{2} \frac{1}{2}; 1 \ell)] W(j'jI'I; 1 R) \delta_{\ell\ell'} + g_R (-1)^{I+j+R} [R(R+1) \\
& \times (2R+1)]^{1/2} W(RR'I'I'; 1 j) \delta_{\ell\ell'} \delta_{jj'} \left. \right\} \Big|^2 \quad (7-4)
\end{aligned}$$

(These equations are derived in Appendix A.) The transition probabilities are found from:

$$\lambda = \frac{8\pi(L+1)}{L[(2L+1)!!]} 2 \frac{k^{2L+1}}{h} B(L) \quad (7-5)$$

Results are listed in Table 6 along with single particle estimates. Calculated lifetimes are much faster than the single particle estimates, a result of the collective enhancement which was also noticed in the calculation of the quadrupole moment. There are two points for a detailed comparison with the experimental results. First, there is the ratio of the relative intensities of the 620 and 596 kev gamma rays which is 2.3. Results shown in Table 6 suggest a value of about 0.1, and the single particle estimates give a ratio of 8.5. The second point of comparison is that of the B(E2) value for the 512 kev transition. Fagg, Geer, and Wolicki (16) report a value of  $1.2 \times 10^{-50}$  for the B(E2) reduced transition probability determined by Coulomb excitation. The inverse transition probability for gamma

Table 6. Transition probabilities.

Transition Energy (kev)	I <sub>o</sub>	I <sub>f</sub>	$\lambda_{\text{calc}}(\text{sec}^{-1})$	$\lambda_{\text{sp}}(\text{sec}^{-1})$	$\lambda_{\text{exp}}(\text{sec}^{-1})$
620 (E2)	5/2	5/2	$1.20 \times 10^{13}$	$1.53 \times 10^9$	$> 2.0 \times 10^9$
620 (M1)	5/2	5/2	$4.00 \times 10^{13}$	$1.34 \times 10^{10}$	"
596 (E2)	5/2	1/2	$5.34 \times 10^{14}$	$1.64 \times 10^9$	"
596 (M1)	5/2	1/2	0	0	"
512 (E2)	1/2	3/2	$5.85 \times 10^{15}$	$1.53 \times 10^9$	"
512 (M1)	1/2	3/2	$2.43 \times 10^{14}$	$1.52 \times 10^{13}$	"
488 (E2)	5/2	3/2	$9.60 \times 10^{15}$	$1.93 \times 10^8$	"
488 (M1)	5/2	3/2	$1.25 \times 10^{13}$	$8.28 \times 10^{12}$	"

ray emission is found from (1): ( $I_i = \frac{1}{2}$  and  $I_f = \frac{3}{2}$ )

$$B(E2)_\gamma = \frac{2I_f + 1}{2I_i + 1} B(E2)_{\text{Coulomb}} \quad (7-6)$$

Thus, the experimental value of  $B(E2)_\gamma$  is  $2.4 \times 10^{-50}$ . From equation 7-3 the theoretical value is  $3.1 \times 10^{-50}$ . These two comparisons of data suggest that the 512 kev level may be described by eigenvectors of Table 3 but the higher energy levels may not.

In Chapter 4, the spins of the levels in  $\text{Ga}^{71}$ , as predicted by the model, agree with the assignments deduced from the decay data. There is another argument for the  $1/2^-$  assignment to the 512 kev level. Alder, et al., (1) show that for Coulomb excitation of an odd A nucleus in the vibrational region, the reduced E2 transition probability is given by:

$$B(E2; I_o \rightarrow I_f) = \frac{1}{5} \frac{2I_f + 1}{2I_o + 1} B(E2; I = 0 \rightarrow I = 2)_{\text{ph}} \quad (7-7)$$

where  $B(E2)_{\text{ph}}$  is the transition probability for excitation of the adjacent even-even nucleus and is given by:

$$B(E2; I = 0 \rightarrow I = 2)_{\text{ph}} = \left(\frac{3}{4\pi} Z e R_o^2\right)^2 \beta_2^2 \quad (7-8)$$

Using  $B(E2) = 1.2 \times 10^{-50}$  and setting  $R_o = 1.23 A^{1/3}_f$  and  $I_o = 3/2$ ,  $\beta_2$  was calculated for various values of  $I_f$ . The results are as follows:  $\beta_2 = 0.18$  ( $I_f = 1/2$ ),  $\beta_2 = 0.09$  ( $I_f = 3/2$ ),  $\beta_2 = 0.06$

( $I_f = 5/2$ ), and  $\beta_2 = 0.05$  ( $I_f = 7/2$ ). Unless the interaction between the proton and the  $\text{Zn}^{70}$  core is very strong, the deformation parameter should not be very different from that of the core, e. g.

$\beta_2 \approx 0.18$ . It is concluded that the 512 keV level has spin and parity of  $1/2^-$ , in agreement with the model predictions.

In summary, it appears reasonable to describe the structure of  $\text{Ga}^{71}$  in terms of the Unified Model. Agreement between the low lying energy levels which were calculated theoretically and those determined experimentally, and the consistency in the parameters which are determined, e. g.  $E_1$ ,  $E_2$ ,  $E_3$ , and  $V_0$ , support this conclusion. Also, some of the more sensitive quantities, such as the magnetic dipole and electric quadrupole moments, are in good or reasonable agreement with experiment. Calculated gamma ray transition probabilities are verified somewhat by experiment, but data is very sparse.

Arguments are reasonable which lead to the experimental spin and parity assignments of the low lying levels of  $\text{Ga}^{71}$ . However, these results are not conclusive and a more direct determination of the spins is needed. Also, a more direct determination of the level energies is needed to provide verification of the deduced level scheme. (For example, they can be determined from inelastic scattering of nuclear particles from  $\text{Ga}^{71}$ .) Particularly, a search



should be made for  $3/2^-$  and  $7/2^-$  levels in the 1500 kev region, since these levels are predicted by the model.

## BIBLIOGRAPHY

1. Alder, K. et al. Study of nuclear structure by electromagnetic excitation with accelerated atoms. *Reviews of Modern Physics* 28:428-542. 1956.
2. Blair, A. G.  $\text{Ni}^{62,64}(\text{He}^3, \text{d})\text{Cu}^{63,65}$  reaction. *Physical Review* 140:B648-B654. 1965.
3. Blair, J. S. Inelastic diffraction scattering. *Physical Review* 115:928-938. 1959.
4. Blair, J. S., D. Sharp and L. Wilets. Inelastic scattering by deformed nuclei. *Physical Review* 125:1625-1638. 1962.
5. Blatt, J. M. and V. F. Weisskopf. *Theoretical nuclear physics*. New York, Wiley, 1952. 864 p.
6. Bohr, A. The coupling of nuclear surface oscillations to the motion of individual nucleons. *Det Kongelige Danske Videnskabernes Selskab Matematisk-fysiske Meddelelser* 26(14): 1-40. 1952.
7. Bohr, A. and B. Mottelson. *Collective and individual particle aspects of nuclear structure*. 2d ed. Kobenhavn, Ejnar Munksgaard, 1957. 174 p. (Original ed. in *Det Kongelige Danske Videnskabernes Selskab Matematisk-fysiske Meddelelser* 27(16):1-174)
8. Bouten, M. and P. Van Leuven. Cu isotopes by the unified model. *Nuclear Physics* 32:499-503. 1962.
9. Braunstein, A. and A. de-Shalit. New evidence for core excitation in  $\text{Au}^{197}$ . *Physics Letters* 1:264-266. 1962.
10. Broek, H. W. Collective excitations in  $\text{Ni}^{58,60,62}$  and  $\text{Zn}^{64,66,68}$ . *Physical Review* 130:1914-1925. 1963.
11. Buck, B. Excitation of two-phonon states by inelastic alpha-particle scattering. *Physical Review* 127:940-942. 1962.

12. Choudhury, D. C. Intermediate coupling calculations in the unified nuclear model. Det Kongelige Danske Videnskabernes Selskab Matematisk-fysiske Meddelelser 28(4):1-15. 1954.
13. de-Shalit, A. and I. Talmi. Nuclear shell theory. New York, Academic Press, 1963. 573p.
14. Drozdov, S. I. The scattering of fast neutrons by non spherical nuclei II. Soviet Physics, JETP 1:588-591. 1955.
15. Edwards, W. F. and C. J. Gallagher. The decay of  $\text{Se}^{75}$ . Nuclear Physics 26:649-657. 1961.
16. Fagg, L. W., E. H. Geer and E. A. Wolicki. Coulomb excitation of V, Ni, Ga, and Rb. Physical Review 104:1073-1076. 1956.
17. Glendenning, N. K. Theoretical predictions for the spectra of the odd-mass xenon and tellurium isotopes. Physical Review 119:213-217. 1960.
18. Grahame, D. C. and G. T. Seaborg. The distribution of minute amounts of material between liquid phases. Journal of the American Chemical Society 60:2524-2528. 1938.
19. Green, A. E. S. Nuclear physics. New York, McGraw-Hill, 1955. 535p.
20. Green, R. F. and R. E. Bell. Notes on a fast time-to-amplitude converter. Nuclear Instruments 3:127-132. 1958.
21. Hofstadter, Robert. Electron scattering and nuclear structure. Reviews of Modern Physics 28:214-254. 1956.
22. Hollander, Jack M. The impact of semiconductor detectors on gamma ray and electron spectroscopy. 1965. 130p. (United States Atomic Energy Commission, UCRL-16307)
23. Inopin, E. V. and Yu. A. Berezhnoy. Effect of nuclear surface diffuseness on diffraction scattering. Nuclear Physics 63:689-694. 1965.
24. Kisslinger, L. S. and R. A. Sorensen. Spherical nuclei with simple residual forces. Reviews of Modern Physics 35:853-915. 1963.

25. Lawson, R. D. and J. L. Uretsky. Center of gravity theorem in nuclear spectroscopy. *Physical Review* 108:1300-1304. 1957.
26. Leblanc, J. M., J. M. Cork and S. B. Burson. Radioactivities of  $Zn^{69}$  and  $Zn^{71}$ . *Physical Review* 97:750-753. 1955.
27. Li, A. C. and Sergio Monaro. Gamma radiation from  $Zn^{71}$  and  $Zn^{71m}$ . *Nuclear Physics* A91:353-364. 1967.
28. Lin, E. K. Inelastic scattering of deuterons from Zn and Se isotopes. *Nuclear Physics* 73:613-624. 1965.
29. Marion, J. B., Visiting Associate, California Institute of Technology, Dept. of Physics. Unpublished compilation of gamma ray standards. Pasadena, California, 1966.
30. Marlow, K. W. Determination of some energy levels in light and medium weight nuclei with a precision gamma ray scintillation spectrometer. *Nuclear Physics* 51:684-689. 1964.
31. Marlow, K. W. Further precision gamma ray measurements with a scintillation spectrometer. *Nuclear Physics* 61:13-16. 1965.
32. National Research Council, Nuclear Data Group. Nuclear Data Sheets. Washington, D. C., 1955 et seq. various paging.
33. Newton, T. D. Decay constants from coincidence experiments. *Physical Review* 78:490. 1950.
34. Perey, F. G. Optical model analysis of proton elastic scattering in the range of 9 to 22 Mev. *Physical Review* 131:745-763. 1963.
35. Preston, M. A. Physics of the nucleus. Reading, Massachusetts, Addison-Wesley, 1962. 661p.
36. Robinson, R. L. et al. Gamma ray energies determined with a lithium drifted germanium detector. *Nuclear Physics* 74:281-288. 1964.
37. Rose, M. E. Elementary theory of angular momentum. New York, Wiley, 1957. 248p.

38. Sharff-Goldhaber, G. and J. Weneser. System of even-even nuclei. *Physical Review* 98:212-214. 1955.
39. Sommerfeldt, Raymond Walter. Perturbed directional correlation in  $\text{Ta}^{181}$ . Ph.D. thesis. Corvallis, Oregon State University, 1964. 110 numb. leaves.
40. Sonnino, T., E. Eichler and S. Amiel. The decay of 4.1 hour  $\text{Zn}^{71}$ . *Nuclear Physics* 54:568-576. 1964.
41. Stelson, P. H. and F. K. McGowan. Coulomb excitation of the first  $2^+$  state of even nuclei with  $58 \leq A \leq 82$ . *Nuclear Physics* 32:652-668. 1962.
42. Tandon, P. N. and H. G. Devare. On the decay of the 4-hour activity of  $\text{Zn}^{71}$ . *Nuovo Cimento* 32:388-395. 1964.
43. Thankappan, V. K. and W. W. True. Properties of the low lying  $\text{Cu}^{63}$  levels. *Physical Review* 137:793-799. 1965.
44. Thwaites, T. T. and W. W. Pratt. Decay of the  $\text{Zn}^{71}$  isomers. *Physical Review* 124:1526-1531. 1961.
45. U. S. National Bureau of Standards. Tables for the analysis of beta spectra. Washington, D. C., 1952. 61p. (Applied Mathematics Series-13)
46. Wilson, H. L. and M. B. Sampson. Scattering of 22 Mev alpha particles by  $\text{Fe}^{56}$ ,  $\text{Zn}^{64}$ ,  $\text{Zn}^{66}$ , and  $\text{Zn}^{68}$ . *Physical Review* 137:B305-B314. 1965.

## APPENDICES

## APPENDIX A

DERIVATIONS OF FORMULAS FOR  
UNIFIED MODEL CALCULATIONSMagnetic Dipole Moment

The magnetic moment operator is given by:

$$\mu = (g_\ell \ell_z + g_s S_z + g_R R_z) \mu_N \quad (\text{A1-1})$$

where  $g_\ell = 1$  for a proton outside of a closed core,  $g_s = 5.585$ , and  $g_R \approx Z/A$  from the approximation of a spinning, uniformly charged sphere.  $R_z$  is the  $z$  component of angular momentum of the spinning core. The magnetic dipole moment is then given by:

$$\langle \mu \rangle_{M=I} = \langle IM | \mu | IM \rangle_{M=I} \quad (\text{A1-2})$$

For the core plus proton model the eigenfunctions are given by:

$$\begin{aligned} |IM\rangle &= \sum_{j'N'R'} a(j', N'R', I) |j', N'R', IM\rangle \\ &= \sum_{j'N'R'} \sum_{m'} a(j', N'R', I) C(j'R'I; m'M-m') |j'm'\rangle |N'R'R'_\mu\rangle \end{aligned} \quad (\text{A1-3})$$

So

$$\begin{aligned}
\langle \mu \rangle_{M=I} &= \sum_{\substack{jNR \\ j'N'R'm'}} \sum_m a(j, NR, I) a(j', N'R', I) C(jRI; mM-m) C(j'R'I; m'M-m') \\
&\times \{ \langle j' | g_{\ell} \ell_z + g_s s_z | j \rangle \delta_{NN'} \delta_{RR'} \\
&+ \delta_{jj'} \langle N'R' | g_R R_z | NR \rangle \}_{M=I} \quad (A1-4)
\end{aligned}$$

Consider the first term in equation A1-4. From Rose (37) equation 6.24 the matrix elements of an irreducible tensor operator of rank  $L$  is:

$$\begin{aligned}
\langle j'_1 j'_2 j'm' | T_{LM}(1) | j_1 j_2 jm \rangle &= C(jLj'; mMm') (-1)^{j_2+L-j'_1-j'} \delta_{j'_1 j_1} \delta_{j'_2 j_2} \\
&\times [(2j'_1 + 1)(2j + 1)]^{1/2} \\
&\times W(j_1 j j'_1 j'; j_2 L) \langle j'_1 | | T_L(1) | | j_1 \rangle \quad (A1-5)
\end{aligned}$$

Now,  $\ell_z$  is a first rank tensor, so

$$\begin{aligned}
\langle \ell' s' j' m' | \ell_z | \ell s j m \rangle &= C(j_1 j'; m m') (-1)^{1/2-\ell-j'} \delta_{ss'} [(2\ell'+1)(2j+1)]^{1/2} \\
&\times W(\ell j \ell' j'; \frac{1}{2} 1) \langle \ell' | | \ell | | \ell \rangle \quad (A1-6)
\end{aligned}$$

where

$$\langle \ell' | | \ell | | \ell \rangle = \sqrt{\ell(\ell+1)} \delta_{\ell\ell'} \quad (A1-7)$$

Then,



$$\begin{aligned}
\langle \mu_{\ell} \rangle = & g_{\ell} \sum_{\substack{jNR \\ j'N'R' m'}} \sum_m a(j, NR, I) a(j', N'R', I) C(jRI; m, M-m) C(j'R'I; m'M-m') \\
& \times \delta_{NN'} \delta_{RR'} C(jlj'; mom') (-1)^{1/2-\ell-j'} \delta_{ss'} [(2\ell'+1)] \\
& \times \frac{1}{2} \delta_{\ell\ell'} W(\ell j \ell' j'; \frac{1}{2} 1) \quad (A1-8)
\end{aligned}$$

Using the symmetry relations for the Clebsch-Gordon coefficients (Rose 37) and the Racah coefficients and making use of the summation relation

$$\begin{aligned}
\sum_{\beta} C(abe; \alpha\beta) C(edc; \alpha+\beta, \delta) C(bdf; \beta\delta) = [(2e+1)(2f+1)]^{1/2} \\
\times W(abcd; ef) C(afc; \alpha, \beta+\delta) \quad (A1-9)
\end{aligned}$$

then

$$\begin{aligned}
\langle \mu_{\ell} \rangle_{I=M} = & g_{\ell} \delta_{\ell\ell'} \delta_{NN'} \delta_{RR'} (-1)^{R+\ell+3/2} W(\ell\ell jj'; \frac{1}{2}) W(jj' II; 1R) \\
& \times [(2j+1)(2j'+1)]^{1/2} [\ell(\ell+1)(2\ell+1)]^{1/2} \left[ \frac{I(2I+1)}{I+1} \right]^{1/2} \quad (A1-10)
\end{aligned}$$

The other terms in equation follow in essentially the same manner and the final expression for the magnetic dipole moment is,

$$\begin{aligned}
\langle \mu \rangle = & \mu_N \left[ \frac{I(2I+1)}{I+1} \right]^{1/2} \sum_{\substack{jNR \\ j'N'R'}} a(j, NR, I) a(j', N'R', I) \\
& \times \left\{ g_R (-1)^{I+j-R} \delta_{NN'} \delta_{RR'} \delta_{jj'} \delta_{\ell\ell'} [R(R+1)2R+1] \right\}^{1/2} \\
& \times W(RR II; 1j) + g_\ell (-1)^{R-\ell+1/2+j+j'-I} \delta_{RR'} \delta_{NN'} \delta_{\ell\ell'} [(2j+1) \\
& \times (2j'+1)]^{1/2} [\ell(\ell+1)(2\ell+1)]^{1/2} W(jj' II; 1R) W(\ell\ell jj'; 1 \frac{1}{2}) \\
& + g_s (-1)^{\ell+1/2+R-I} \delta_{NN'} \delta_{RR'} \delta_{\ell\ell'} \left[ \frac{\sqrt{3}}{2} [(2j+1)(2j'+1)] \right]^{1/2} \\
& \times W(jj' II; 1R) W(jj' \frac{1}{2} \frac{1}{2}; 1\ell) \Big\} \quad (A1-11)
\end{aligned}$$

### Electric Quadrupole Moment

The electric quadrupole moment operator  $Q_{op}$  for the core plus proton model is given by, (7)

$$Q_{op} = \sqrt{\frac{16\pi}{5}} (1 - Z/A^2) r^2 Y_{20}(\theta, \phi) + \frac{3}{\sqrt{5\pi}} Z R_o^2 a_{20}^+ \quad (A2-1)$$

Again using the eigenvectors of equation A1-3  $Q$  is evaluated by

$$Q = \langle Q_{op} \rangle_{I=M}$$

The first term in  $Q_{op}$  is an irreducible tensor operator of rank two, so using equation A1-5,

$$\begin{aligned} \langle j', N'R', IM | Y_{20} | j, NR, IM \rangle_{M=I} &= C(I2I; MOM)(-1)^{R-j-I} \delta_{RR'} [(2j'+1) \\ &\times (2j+1)]^{1/2} W(jIj'I; R2) \langle j' || Y_2 || j \rangle \quad (A2-2) \end{aligned}$$

The Clebsch-Gordon coefficient is readily evaluated for  $M=I$  as

$$C(I2I; IOI) = \sqrt{\frac{I(2I-1)}{(I+1)(2I+3)}} \quad (A2-3)$$

and the reduced matrix element of  $Y_2$  was evaluated from equation 4-22. The second term in  $Q_{op}$  represents the collective motion contribution. Using

$$a_{20}^+ = \left(\frac{\hbar\omega}{2C}\right)^{1/2} (b_{20}^+ + b_{20}) \quad (A2-4)$$

the term is evaluated from equation A1-5. The final result for  $Q$  is:

$$\begin{aligned} \langle Q \rangle &= \langle r^2 \rangle \sqrt{\frac{I(2I-1)(2I+1)}{(I+1)(2I+3)}} \sum_{\substack{jNR \\ j'N'R'}} a(j, NR, I) a(j', N'R', I) \\ &\times \left\{ \sqrt{\frac{16\pi}{5}} (1 - Z^2/A) (-1)^{I+j-R} \delta_{NN'} \delta_{RR'} [(2j'+1)]^{1/2} \right. \\ &\times \langle j' || Y_2 || j \rangle W(jj'I; 2R) + \frac{3}{\sqrt{5\pi}} Z \left(\frac{\hbar\omega}{2C}\right)^{1/2} (-1)^{I-j} \delta_{jj'} \delta_{\ell\ell'} \\ &\times [(-1)^{R'} \sqrt{(2R'+1)} \langle N'R' || b^+ || NR \rangle \\ &\left. + (-1)^R \sqrt{(2R+1)} \langle N'R' || b || NR \rangle \right\} W(RR'I; 2j) \quad (A2-5) \end{aligned}$$

### Reduced Transition Probabilities B(E2) and B(M1)

Using the eigenvectors of equation A1-3, the reduced transition probabilities for photon emission are given by:

$$B(\sigma\lambda) = \frac{1}{2I+1} \sum_{MM'\mu} |\langle I'M' | M_\sigma(\lambda, \mu) | IM \rangle|^2 \quad (A3-1)$$

$I \rightarrow I'$

where  $\sigma$  is E or M for electric or magnetic radiation and  $\lambda = 0, 1, 2, \dots$  is the multipole order.

### Electric Quadrupole Radiation

The multipole operator is

$$M_e(2, \mu) = (1 - Z/A^2) r^2 Y_{2\mu}(\theta, \phi) + \frac{3}{4\pi} Ze R_o^2 a_2^+ \quad (A3-2)$$

where

$$a_{2\mu}^+ = \left(\frac{\hbar\omega}{2C}\right)^{1/2} [b_\mu^+ + (-1)^\mu \overline{b}_\mu] \quad (A3-3)$$

So in equation A3-1,

$$B(E2) = \frac{1}{2I+1} \sum_{MM'\mu} \left| \sum_{\substack{jNR \\ j'N'R'}} a(j, NR, I) a(j', N'R', I') \right. \\ \left. \langle I'M' | \gamma_1 Y_{2\mu} + \gamma_2 [b_\mu^+ + (-1)^\mu \overline{b}_\mu] | IM \rangle \right|^2 \quad (A3-4)$$

where

$$\gamma_1 = (1 - Z/A^2) \langle r^2 \rangle \quad \gamma_2 = \frac{3}{4\pi} \left( \frac{\hbar\omega}{2C} \right)^{1/2} Z e R_o^2 \quad (\text{A3-5})$$

From equation A1-5

$$\begin{aligned} \langle j', N'R', I'M' | Y_{2\mu} | j, NR, IM \rangle &= \delta_{NN'} \delta_{RR'} (-1)^{R-j'-I'} C(I2I'; M_\mu M') \\ &\times [ (2j'+1)(2j+1) ]^{1/2} W(jIj'I'; R2) \\ &\times \langle j' || Y_2 || j \rangle \end{aligned} \quad (\text{A3-6})$$

and similarly,

$$\begin{aligned} \langle j', N'R', I'M' | b_{2\mu} | j, NR, IM \rangle &= C(I2I'; M_\mu M') (-1)^{j-R-I'} \delta_{jj'} \\ &\times [ (2R'+1)(2R+1) ]^{1/2} \\ &\times W(RIR'I'; j2) \langle N'R' || b_2 || NR \rangle \end{aligned} \quad (\text{A3-7})$$

When these matrix elements are substituted into equation A3-1 and the squaring operation performed, the cross terms are zero because of the  $\delta_{NN'} \langle N'R' || b || NR \rangle$  term which occurs. The sum over  $M$  and  $\mu$  for the square of the Clebsch-Gordon coefficient gives 1, and the sum over  $M'$  gives a factor  $2I' + 1$ . Combining all terms gives the final expression:

$$\begin{aligned}
B(E2) = & \frac{2I'+1}{2I+1} \left| \sum_{\substack{jNR \\ j'N'R'}} a(j', N'R', I') a(j, NR, I) \right\{ \gamma_1 (-1)^{I'+j-R} [(2j'+1) \\
& \times (2j+1)]^{1/2} W(jj'I'I'; 2R) \langle j' || Y_2 || j \rangle \delta_{NN'} \delta_{RR'} \\
& + \gamma_2 (-1)^{I'-j} [(-1)^R [(2R+1)(2R'+1)]^{1/2} \langle N'R' || b || NR \rangle \\
& + (-1)^{R'} [(2R+1)(2R'+1)]^{1/2} \langle N'R' || b^+ || NR \rangle] \\
& \times W(RR'I'I'; 2j) \delta_{jj'} \delta_{\ell\ell'} \left. \right\}^2 \quad (A3-8)
\end{aligned}$$

#### Magnetic Dipole Radiation

$$M_m(l, \mu) = \frac{e\hbar}{2Mc} \sqrt{\frac{3}{4\pi}} (g_\ell \ell_\mu + g_s s_\mu + g_R R_\mu) \quad (A3-9)$$

From equation A3-1,

$$\begin{aligned}
B(M1) = & \frac{1}{2I+1} \sum_{MM'\mu} a(j, NR, I) a(j', N'R', I') \\
& \langle j', N'I', M' | \beta (g_\ell \ell_\mu + g_s s_\mu + g_R R_\mu) | j, NR, IM \rangle^2 \quad (A3-10)
\end{aligned}$$

where  $\beta = \frac{e\hbar}{2Mc} \sqrt{\frac{3}{4\pi}}$  and  $|j, NR, I\rangle$  are defined as in equation A1-3.

Consider the term with  $g_\ell \ell_\mu$  (the calculations are similar for the term with  $g_s s_\mu$ ):

$$I = \langle j' N' R' I' M' | \ell_\mu | j, NR, IM \rangle = \sum_{mm'} C(jRI; m M - m) C(j' R' I'; m' M' - m') \\ \times \langle j' | \ell_\mu | j \rangle \langle N' R' | NR \rangle \quad (A3-11)$$

but  $\langle N' R' | NR \rangle = \delta_{NN'} \delta_{RR'}$  and from equation A1-5,

$$\langle j' | \ell_\mu | j \rangle = C(j1j'; m_\mu m') (-1)^{3/2 - \ell' - j'} \delta_{ss'} [(2\ell' + 1)(2j + 1)]^{1/2} \\ \times W(\ell j \ell' j'; \frac{1}{2} 1) \langle \ell' || \ell || \ell \rangle \quad (A3-12)$$

where  $\langle \ell' || \ell || \ell \rangle = \sqrt{\ell(\ell+1)} \delta_{\ell\ell'}$ . So,

$$I = (-1)^{3/2 - \ell' - j'} \delta_{\ell\ell'} \delta_{NN'} \delta_{RR'} W(\ell j \ell' j'; \frac{1}{2} 1) [(2\ell' + 1)(2j + 1)(\ell + 1)\ell]^{1/2} \\ \times \sum_{mm'} C(jRI; m M - m) C(j' R' I'; m' M' - m') C(j1j'; m_\mu m') \quad (A3-13)$$

The sum over the Clebsch-Gordon coefficients is made using equation A1-9, where  $a = I$ ,  $B = j$ ,  $c = I'$ ,  $d = j'$ ,  $e = R$ , and  $f = 1$ , and finally,

$$\langle I' M' | \ell_\mu | IM \rangle = \sum_{jj'NR} a(j, NR, I) a(j', NR, I') (-1)^{3/2 - \ell' - j'} \delta_{\ell\ell'} \delta_{NN'} \delta_{RR'} \\ \times (-1)^{R+2j'-I'+j-1} [(2\ell+1)(2j+1)(\ell+1)\ell]^{1/2} \\ \times W(\ell j \ell' j'; \frac{1}{2} 1) (2j'+1)^{1/2} (2I+1) C(I1I'; M_\mu) \quad (A3-14)$$

The last expression is inserted into A3-1, making use of the relation:

$$\sum_{MM'\mu} |C(II'I;M\mu)|^2 = \sum_{M'} 1 = 2I' + 1 \quad (\text{A3-15})$$

The final expression for B(M1) becomes:

$$\begin{aligned} B(M1) = & \frac{3}{4\pi} \mu_N^2 (2I'+1) \left| \sum_{jj'NR} a(j, NR, I) a(j', NR, I') \right\{ (-1)^{R+I'+\ell-1/2} \\ & \times [(2j+1)(2j'+1)]^{1/2} [g_\ell (-1)^{j+j'} [\ell(2\ell+1)(\ell+1)]^{1/2} W(j'j\ell\ell; 1\frac{1}{2}) \\ & + g_s \sqrt{3/2} W(j'j\frac{1}{2}\frac{1}{2}; 1\ell)] W(j'jI'I; 1R) \delta_{\ell\ell'} + g_R (-1)^{I+j+R} \\ & \times [R(R+1)(2R+1)]^{1/2} W(RRII'; 1j) \delta_{\ell\ell'} \delta_{jj'} \} \Big|^2 \quad (\text{A3-16}) \end{aligned}$$



## APPENDIX B1

COMPUTER PROGRAM MATRIXL  
CALCULATION OF MATRIX ELEMENTS

```

      PROGRAM MATRIXL
      DIMENSION Y1 (500), Y2 (500), Y3 (500), W (500, 3), N (3), D (500),
1      T (500, 6), SO (6), SE (6), AREA(6)
C  CALCULATION OF WAVE FUNCTIONS -- H = MESH SIZE
      H= 0.1
      N1= 0
      VO= 70.0
      E= 7.8
      CALL BSWF (Y1, 2, 1.0, E, VO, 0.67, 5.40, H, N1)
      DO 15 I=1, N1
15  W (I, 1)= Y1 (I)
      N (1)=N1
      N2= 0
      VO= 70.0
      E= 6.8
      CALL BSWF (Y2, 1, 3.0, E, VO, 0.67, 5.40, H, N2)
      DO 16 I=1, N2
16  W (I, 2)=Y2 (I)
      N (2)=N2
      N3= 0
      VO= 70.0
      E= 5.6
      CALL BSWF (Y3, 2, 1.0, E, VO, 0.67, 5.40, H, N3)
      DO 17 I=1, N3
17  W (I, 3)= Y3 (I)
      N (3)= N3
      IF (N (1) - N (2)) 23, 24, 24
23  IF (N (2) - N (3))33, 34, 34
33  NMAX = N (3)
      NMIN = N (1)
      GO TO 40
34  NMAX = N (2)
      NMIN = N (1)
      GO TO 40
24  IF (N (1) - N (3)) 36, 35, 35
35  NMAX = N (1)
      GO TO 41
36  NMAX = N (3)
      NMIN = N (2)
      GO TO 40
41  IF (N (2) - N (3)) 37, 38, 38
37  NMIN = N (2)
      GO TO 40
38  NMIN = N (3)
40  CONTINUE

```

## C CALCULATION OF INTEGRANDS

```

      DO 12 I = 1, 3
      M = N (I)
      DO 12 J = 1, M
12    T(J, I) = W(J, I)*W(J, I)*D(J)
      DO 13 I = 4, 5
      DO 13 J = 1, NMAX
13    T(J, I) = W(J, I-3)*W(J, I-2)*D(J)
      DO 14 I = 1, NMAX
14    T(I, 6) = W(I, 1)*W(I, 3)*D(I)
      DO 51 I = 1, 6
      AREA (I) = 0.
      SE (I) = 0.
51    SO (I) = 0.
      DO 61 J = 1, 3
      DO 60 I = 3, NMIN, 2
60    SO (J) = SO(J)+T(I, J)
      DO 61 I = 2, NMIN, 2
61    SE(J) = SE(J) + T(I, J)
      DO 63 J = 4, 6
      DO 62 I = 3, NMIN, 2
62    SO (J) = SO (J)+T (I, J)
      DO 63 K=2, NMIN, 2
63    SE (J) = SE (J)+T (I, J)

```

## C RADIAL INTEGRALS BY SIMPSONS RULE

```

      DO 70 I=1, 3
      AREA (I) = AREA (I)+0.0333* (T (1, I)+4.0*SE(I)+2.0*SO (I)+T (NMAX, I))
      PRINT 100, AREA
100  FORMAT (6H AREA =, E16. 8, //)
      CALL EXIT
      END

```

## APPENDIX B2

COMPUTER PROGRAM BSWF  
BOUND STATE WAVE FUNCTIONS FOR THE SAXON-WOODS POTENTIAL

```

SUBROUTINE BSWF (Y, NODE, AL, E, VO, BO, RO, H, N2)
DIMENSION Y(500), A(500), P(300), Z(300)
E = -.04782*E
SWITCH = 0.
YMAX = 1.
NPRINT=N2
KTEST= 0
41  I= 1
    FVO= 0.
    F2= 1000000.
17  R=H*FLOATF (I)
    CALL POT (R, RO, BO, AL, VO, U, VI)
    F=U-E
    IF (F) 50, 51, 51
51  IF (F-F2)50, 18, 18
50  F2=F
    X= H*H*F
    A (I)= 1. -X/12.
    B= 2. +X/ A (I)
    IF (I-1)14, 15, 14
15  Y (1)= A (1)* H/YMAX
    Y (2)= B* Y (1)
    GO TO 16
C  INTEGRATE OUT
14  Y (I + 1)= B*Y (I) - Y (I-1)
16  FVD = VI*Y (I)* Y (I)/A (I)* A (I)) + FVD
    I= I+1
    IF (I-500)36, 35, 35
35  PRINT 204
204  FORMAT (46H NUMBER OF MESH PTS. IN OUTWARD INTEGRATION IS,
1    15H MORE THAN 500.)
    RETURN
36  CONTINUE
    GO TO 17
C  INTEGRATE IN
18  M= I-1
    BM=B
    N = 1
24  MN= M+N
    R = H*FLOATF(MN)
    CALL POT (R, RO, BO, AL, VO, U, VI)
    Y (MN)= VI
    X= (U-E)*H*H/12.
    A (MN)= 1. -X
    B= 2. +10. *X

```

```

      IF (N-1)22, 23, 22
23  P (1)= -A (M+1)/B
      Z (1)= -Y (M)
26  N= N+1
      IF (N-300)24, 28, 28
28  PRINT 200
200  FORMAT (45H NUMBER OF MESH PTS. IN INWARD INTEGRATION IS,
1    15H MORE THAN 300.)
      RETURN
22  P (N)= -1. /(B/A (MN) + P (N-1))
      Z (N)= -P(N-1) * Z (N-1)
      W= .002*H*SQRTF (-E)
      IF (ABSF (Z (N)) -W) 25, 26, 26
25  N2 = N + M
      N3 = N2 + 1
      N4 = N-1
      R = H*FLOATF (N3)
      FN2 = U-F
      CALL POT (R, RO, BO, AL, VO, U, VI)
      FN3 = U-E
      C = EXPF((R-H)*SQRTF (FN2)-R*SQRTF (FN3))
      A (N3) = 1. -H*H*FN3/12.
      X= Y (N2)
      Y (N2) = Z (N)/(A(N2)/P(N) + C*A(N3))
      FVD= X*Y (N2)*Y(N2) + FVD
      DO 29 I = 1, N4
      K= N2-I
      KM= K-M
      X=Y(K)
      Y(K) = (P(KM)/A(K))* (Z(KM) - A(K+1)*Y (K+1))
29  FVD= X*Y(K)*Y(K) + FVD
      FVD= H*H*FVD/Y(M)
      FV= BM*Y(M)-Y(M-1)-A(M+1)*Y (M+1)
      D= -FV/FVD
      KTEST = KTEST + 1
      IF (KTEST - 10)55, 54, 54
55  IF (SWITCH)52, 56, 52
56  IF (ABSF(D)-.08-VO)57, 43, 43
52  IF (ABSF(D)-.00001 -VO)53, 43, 43
57  SWITCH= 1.
      YMAX= 0.
      DO 59 I=1, M, 5
      IF (YMAX-ABSF (Y(I)))58, 59, 59
58  YMAX= ABSF (Y (I))
      IMAX= I
59  CONTINUE
      YMAX= YMAX/A (IMAX)
43  VO= VO + D
      GO TO 41
54  PRINT 301
301  FORMAT (49H NUMBER OF POTENTIAL ITERATIONS IS MORE THAN 10.)

```

```

53  NODEX= 0
    DO 30 I=1, M
      IF (ABSF(Y (I + 1)-Y (I))-ABSF (Y (I + 1) + Y (I)))30, 31, 32
31  IF (Y (I))30, 32, 30
32  NODEX= NODEX + 1
30  Y (I)= Y (I)/A (I)
      IF (NODEX-NODE)37, 38, 37
37  PRINT 306, NODEX
306  FORMAT (28H WRONG NO. OF NODES,      NODE=, I4)
38  ANORM= 0.
      N= N2/2
      DO 20 I=1, N2
20  ANORM= 4. *Y(2*K-1) *Y(2*K-1) +2. *Y(2*K)*Y(2*K) + ANORM
      ANORM= 1. /SQRTF ((H/3.)* ANORM)
      DO 21 I=1, N2
21  Y (I)= Y (I)*ANORM
      IF(NPRINT)60, 61, 60
61  PRINT 201, NODE, AL, VO
201  FORMAT (12H-BOUND STATE, 5X, 5HNODE=, I3, 5X, 2HL=, F6.1, 5X, 3HVO=, F10.4)
      PRINT 202
202  FORMAT (6H      I, 8X, 4HY (I), 9X, 6HY (I + 1), 7X, 6HY (I + 2), 7X, 6HY (I + 3),
1      7X, 6HY (I + 4), 7X, 6HY (I + 5), 7X, 6HY (I + 6), 7X, 6HY(I + 7)/)
      PRINT 203, (I, Y (I), Y(I + 1), Y (I + 2), Y (I + 3), Y (I + 4), Y(I + 5),
1      Y (I + 6), Y (I + 7), I=1, N2, 8)
203  FORMAT (1H , I5, 3X, 8E13.5)
60  RETURN
    END

```

```

      SUBROUTINE POT (XR,XRO,XBO,XAL,XU,XVI)
      IF (XR) 1, 2, 1
2  PRINT 10
10  FORMAT (5X, 28HDIVIDE BY R = 0 IN POT.  R = .001)
      XR= .001
1  XVI= -.04782/(1. + EXPF((XR-XRO)/XBO))
      XVI= (XAL* (XAL + 1.))/(XR*XR)
      XU= XVO*XVI + XVI
      RETURN
    END

```